RUPRECHT-KARLS-UNIVERSITÄT HEIDELBERG

Antonio Virgilio Failla

Advanced Methods in Spatially Modulated Illumination (SMI) Microscopy

Dissertation

HD-KIP-02-20

KIRCHHOFF-INSTITUT FÜR PHYSIK

Dissertation
submitted to the
Combined Faculties for the Natural Sciences and for Mathematics
of the Ruperto-Carola University of Heidelberg, Germany
for the degree of
Doctor of Natural Sciences

Presented by

Dottore Physica: Antonio Virgilio Failla
born in: Roma Italy
Oral examination: 3th of July 2002

(Title)

Advanced Methods
in
Spatially Modulated Illumination (SMI)
Microscopy

Referees: Prof. Dr. Dr. Christoph Cremer
Prof. Dr. Ioachim Spatz

In this dissertation a new Virtual microscopy approach is presented in order to investigate the potentiality of Spatially Modulated Illumination microscopy in topology investigation and nonosizing. Experimental measurements will follow to all the theoretical previsions. Virtual microscopy evaluations and experiment measurements indicate that with Spatially Modulated Illumination microscopy axial distance measurements in the one nanometer range are feasible and, for the first time in far field light microscopy subwavelength size measurements down to 30 nm can be performed.

Introduction

The purpose of this work is to show how Spatially Modulated Illumination (SMI) microscopy in combination with other microscopy techniques as Spectral Precision Distance Microscopy (SPDM) can play a role of protagonist in the a vast and important branch of the scientific research as biology. The investigation of the intra nuclei micro cosmos is basic to understand how macro processes as for example the evolution of a tumor are going on. This connection between micro and macro cosmo it is just well known is physics; today it is hard to split cosmology and particle physics. Furthermore several evaluation models used in cosmology are also used in microscopy. Starting from light microscopy the need of the man to "look" inside every time smaller area lead to the developing of other microscopy techniques as electron microscopy (EM). Up to now the level of EM is not overcome by any other light microscope and in this dissertation nothing that can reach EM optical and size resolution will be presented. Usually for introduce a new light microscope technique the reason more claimed is that, a biological alive specimen before going on the EM is killed, wasted, cutted and if it is not enough covered with poisonous substances. Imagine that this is not true and the specimen can be send completely alive to the EM microscope and then survive during all the measurements. The question is: What kind of information is avaliable after the acquisition is finished? In modern physics it is established the scientists and the instrumentation used are part of the experiment; then the scientist and the instrumentation should produce only a little perturbation on the phenomena to be studied. A biological specimen represent a little perturbation respect the EM technique. Anyway it is hard to quantify how the configurations presented by an EM microscope are modified by the same EM microscope. The need to have light microscopy advance technique is the need to build up instruments able to not perturb the phenomena of interest expecially when, as in biology cell nuclei phenomena, even a little perturbation can play an important role.

The aim of this work is to discover the limits and the possible application of SMI microscopy expecially in biology investigations. In order to reach this goal it is necessary to build up a virtual microscope in which to reproduce experiments in ideal conditions. The VIM (Virtual Microscopy) (in Latin vim is the accusative of Vis (strength) indicates a powerful research tool that allow the researcher to relate the physical quantities that lead a phenomena to the intensity profiles acquired by the detection system. The advantage is that VIM starting a measurements just knows the result of it and then wants to investigate the answer of the detection system.

In the first Chapter of this dissertation VIM will be introduced together with basic concepts as point-like objects (PSF), Axial Intensity Distribution (AID). Furthermore different topology experiments will be simulated. Topology for the Heidelberg SMI microscope means essentially to measure distances and object sizes along the axial direction because our SMI microscope is one of the SMI microscopes that presents a modulated standing wave field only along one direction, the axial direction. All the simulation shown in Chapter 1 were performed adding Poisson noise to the signal.

In Chapter 2 all the power of VIM is shown: It is well know since the first SMI microscope was built up that the object size perturb the AID. More the object size is comparable with the fringes FWHM and it became even bigger, more the AIDs shape become different respect to the PSFs shape. Never before, which relation exists between the SMI AID and the axial projection of the object size was investigated. VIM as shown in Chapter 2 was able to find this relation. The first step was to create ideal calibration curves, using noise less signal. This calibration curves were realized studying the relation between the AID produced by VIM of well known sized objects and the size $\mathcal{S}$ of them. Changing the size of the object in input the AID was detected in output. More over it was studied how this calibration changes varying other system parameters as the excitation wavelength. Furthermore the analytical expressions for this calibrations were calculated. These analytical expressions depend only on the typical parameters of the system e.g. excitation wavelength, objectives lenses numerical aperture.

In Chapter 3 VIM experiments try to simulate real experimental conditions to understand which size measurements are really feasible in determined experimental conditions. For this reason simulations were performed changing the total number of detected photons in the ideal acquisition chanel and adding to the signal Poisson noise. Furthermore, in order to discover the practical limits of the size measurements the concept of size resolution will be introduced. The definition of size resolution is arbitrary and it will be used only as a parameter for test the quality of the analyzed data.

Distance resolutions with an error less than one nanometer, size evaluation down to 30 nm using an excitation wavelength of 488 nm are some of the prevision of the VIM experiments. All this work without any real experimental measurement is not consistent. Chapter 4 presents the results of axial size measurements performed using different sized fluorescent objects (beads). This results indicate that using the actual SMI excitation wavelengths (647 nm, 488 nm), size measurements far below 100 nm are feasible. In details size measurements down to 40 nm with an excitation wavelength of 647 nm are feasible and size measurements down to 25-30 nm are feasible using 488 nm excitation wavelength. Measurement of the object size in the range of 50-100 nm are feasible with both the previous mentioned wavelength with high accuracy. In such a rance so far no other far field light microscope is able to realize size measurements.

Chapter 5 presents the experimental results of axial and 3D distance measurements. An accuracy between one and two nanometer in axial direction and between 10 and 25 nm for 3D distance evaluations can be obtained normally in a SMI microscope.

Now a really concentrated reader will ask where is the biology? In the first lines of this introduction was strongly claimed the importance of the SMI microscopy for biological application. In Chapter 6 ("dulcis in fundo") a biology experiment is presented. The goal of this experiments is to make an estimation of the size of transcription factories. This estimation so far was possible only using EM. It was possible to perform this experiments only with the collaboration of the MRC (Medical Research Council London) group leaded by Dr. Ana Pombo. The results from the physical point of view indicate that it is possible to estimate the size of the transcription factories using SMI microscopy; how this estimation is close to the real value of the size of transcription factories depends on the quality of the microscopical set up (that for the author can be much improved); about the real importance of this estimation for the biology I can not answer and I think that biologists should answer to this question.

In Chapter 7 a short summary of all the results will be presented and a gallery of images representing new possible applications of SMI and SMI-VIM microscopy are shown.

Chapter 1

SMI Virtual Microscopy Topological Analysis

1.1 Introduction

In the this Chapter SMI Virtual Microscopy (SMI-VIM) will be introduced.[1,2,3,4,5,6] The goal of SMI-Virtual Microscopy is to reproduce a real SMI system and to study its capabilities under ideal schematic and simplified conditions. Furthermore when basic virtual experiments are simulated it became necessary to develop data analysis tools in order to interpreter correctly the results of these simulations; to increase the possibility to understand and read correctly the data acquired by a microscope means to increase the range of the real experiments[7,8,9] in which this microscope can give helpful information to basic research. Data analysis studies allow expecially to know how to investigate the topology of complexis micro systems. Virtual Microscopy is presented in this work to be one of the more valid instruments, if supported after by real experiments, to build up and develop data analysis tools. In fact the possibility to simulate ideal experiments is the simplest way to discover the relations between the physical quantities to be measured and the output microscope signals (Intensities distributions). In a real experiment the results of measurements help to give to the user information about the specimen. VIM is going backward: After all the basic system costants, as objective lenses, numerical aperture emission excitation wavelength, index of refraction, are determined, the variation of the output is studied varying a well known input. In other words the physical quantities as object size and position are supposed to be well known and are varied in a controlled way in order to study how the output, normally the intensity distributions acquired by a camera, is changing. In this way it is possible to discover close mathematical relations between the parameter of the intensity distributions of the system and the physical quantities to be studied, or at least to build up calibration curves. In the following the virtual microscopy model and some virtual microscopy approaches will be presented.

1.2 Fundamentals of SMI Virtual Microscopy (SMI-VIM)

1.2.1 Some basic notion about a SMI-Microscope.

Here it will be not described in details the general design of the microscopical SMI[7,9,10,11,12] setup. Briefly in its central part it consists of a rectangular interferometer starched by 50:50 beam splitter. Each of the two collimated vertically polarized laser beams for the fluorescence excitation has a diameter of about 15 mm and is focused in a back focal plane of two opposite equal objective lenses (for more details see Figure 1.1 and Figure 4.1). This configuration leads to a standing wavefield between the objectives with plane waves and a $\cos^2$ modulation of the laser intensity along the axial direction z (the axial direction is orthogonal to the standing wave field: theoretically should be parallel to line line made by the two objective lenses). The objects which are situated in the space between the objective lenses are mounted between a conventional object slide and a cover slip. To carry out the measurements they can be moved along the axial direction (providing optical sectioning). The minimal step size of the object stage is 10 nm. For the detection of the emitted fluorescence light, on one side between the focusing lense and objective, one mirror is replaced by a dichroic beamsplitter. Since the objectives were designed according to infinite optics, the collimated detection light beam is focused onto the CCD chip of a cooled color CCD camera by a respective tube lens. For excitation in principle all the possible excitation wavelength (λ_{ex}) can be used adjusting and varying opportunely all the optical components of the microscope. In the Heidelberg laboratory an Ar^+ laser ($\lambda_{ex} = 488$ nm) and a Kr^+ laser ($\lambda_{ex} = 647$ nm) are used.

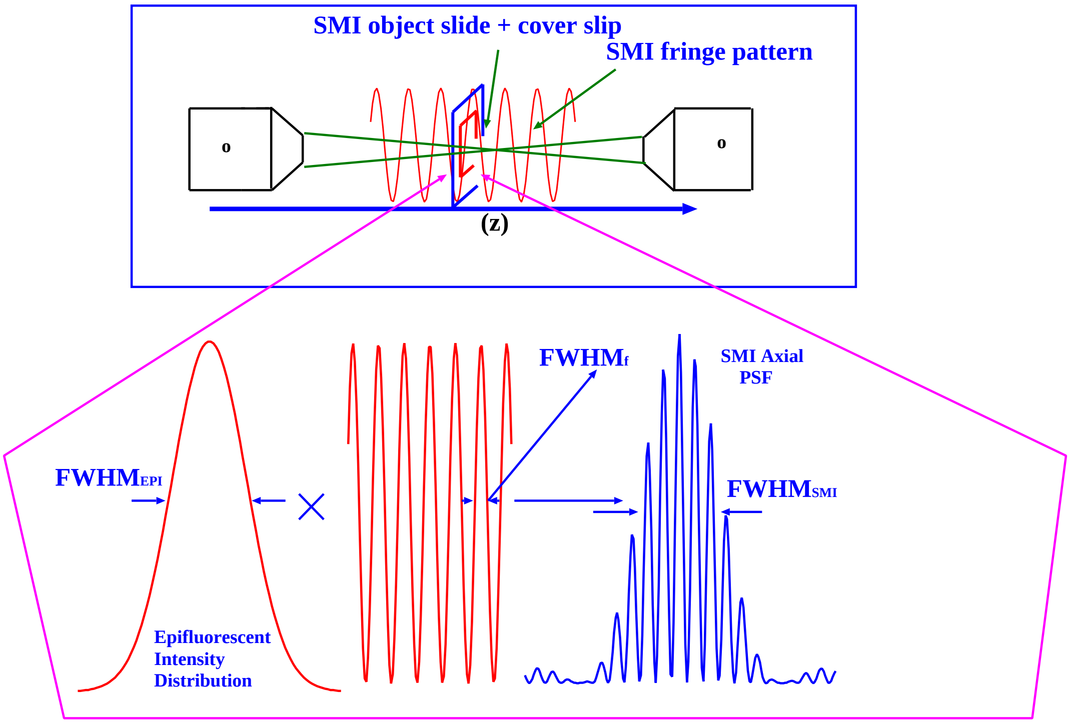

Figure 1.1: SMI microscope basic schematic example: Two collimated vertically polarized laser beams are focused in the back focal plane of two objective lenses (0). This leads to a standing wave field and a $\cos^2$ modulation of the laser intensity between the objective lenses. Bottom a schematic example of the detection Point Spread Function (PSF).

1.2.2 Principle of SMI Microscopy

As told in the previous Section SMI microscopy is characterized by a fringe interference pattern produced by two laser beams focused in to the back focal plane using two opposite objective lenses (for more details see Figure 1.1 and Figure 4.1 and references[7,9,10,11,12]). A point like object here is defined as objects which dimensions are small respect to the physical constants characteristics of the system e.g. the Full-Width-at-Half-Maximum of the excitations fringes ($FWHM_f$) (for more details see Figure 4.1); A point like objects is characterized by an Intensity distribution called Point Spread Function (PSF) (detected by the detection part of the microscope): The PSF is as well a characteristic physical constant of the microscope system, depending only by the microscope physical parameters as for example the numerical aperture (NA) of the objective lenses or the excitation wavelengths.

The PSF of this system can be written in the following way[10,11,12]:

$$PSF_{SMI} = PSF_{EPI}\Big(\cos\frac{2\pi n(z-z_0)}{\lambda_{ex}}\Big)^2; \tag{1.1}$$

where z is the axial coordinate, z_0 is a phase constant, n is the index of refraction of the mounting medium, and PSF_{EPI} is the epifluorescent PSF of a conventional light microscope. In the present work the attention will be concentrated on the Axial Intensity Distribution (AID) of the SMI microscope because this is the peculiar part of the considered system. The lateral intensity distribution (the lateral plane is orthogonal to the optical axis) is a conventional epifluorescent intensity distribution and its properties were detailed studied in a huge amount of previous works. The SMI axial PSF (PSF_z) can be easily evaluated and is given by:[10]

$$PSF_z \simeq A\left[\mathrm{sinc}\left(\frac{\mathrm{z}-\mathrm{z}_1}{\mathrm{B}}\right)\cos \mathrm{K}(\mathrm{z}-\mathrm{z}_0)\right]^2, \tag{1.2}$$

where A is a positive constant, z_1 is the position of the maximum of the PSF_z, B is a constant proportional to the FWHM (FWHM_{EPI}) of the epifluorescence PSF, and $K = \dfrac{2\pi n(z-z_0)}{\lambda_{ex}}$. It should be emphasized that the parameter z_0 contains information about the fringe oscillating pattern; thus it can be arbitrarily assumed to be equal to one of the relative maxima positions of the SMI (PSF_z).

1.2.3 Distance Determination in SMI Microscopy

In scientific imaging the precise evaluation of distances between objects (Topology) is one of the most important information in several fields of research ranging from astronomy to molecular biology. In biology an important topic is to study and understand the organisation of the interphase cell nucleus and its functional role, e.g, in gene regulation or in the formation of chromosome aberrations.[13,14,15,16] To quantify such studies, precise measurements of positions and distances are important. Previously it has been shown that the precision of distance measurements can be highly improved[17] using PSF engineering.[18,19,20] Here will be described in detail a series of computer simulation of axial distance measurements obtained by SMI microscopy.[21,22] Therefore it is necessary to define distance determination algorithms that allow to reach high precisions (standard deviations in a order of few nanometers) in distance measurements: let call $\mathbf{P_1}$, $\mathbf{P_2}$ two point-like objects; z_{1-1}, z_{1-2}, z_{01} and z_{02} are the values of the parameters z_1 and z_0 relative to the point spread function of the two objects. Therefore it is possible to define the axial distance (D_{21}) between $\mathbf{P_1}$ and $\mathbf{P_2}$ in the following way:

$$D_{21} = z_{1-2} - z_{1-1}, \tag{1.3}$$

$$D_{21} = z_{02} - z_{01}; \tag{1.4}$$

Both the definitions are, theoretically, valid; moreover, the two procedures are the same if it is supposed to be $z_1 = z_0$. But, from the practical point of view, while evaluating z_0 in the equation 1.4, an oscillation parameter is determined and all the axial data information is used. Instead, measuring z_1 (see equation 1.3), only the data in a small region around the absolute PSF$_z$ maximum (FWHM $\simeq$ 80 nm for $\lambda_{ex} = 488$ nm) have to be considered. Using the distance definition in equation 1.3, a lower precision in distance determination was observed (data not shown). In the following, only equation 1.4 will be used in the virtual evaluation of the two point-like distance determination.

1.3 SMI VIM Simulations

The SMI-VIM simulations, presented here, were made to study the precision limits in distance measurements of the SMI microscope, varying the total number of photons detected per object (N_{tot}). Especially low photon count conditions were analyzed. In other words, here the interest is focused on the evaluation, by VIM, of the limits of SMI in the distance evaluation. Two independent point-like objects can be mathematically represented by two Dirac delta functions (the computer representation of a Dirac delta function is a voxel-like pulse with a maximum value equal to 255 in grey scale) situated respectively in the position $\mathbf{R}_1(x_1, y_1, z_1)$, $\mathbf{R}_2(x_2, y_2, z_2)$ (a schematic example is shown in Figure 1.2).

$$\mathbf{P_{1(2)}} = \delta(x - x_{1(2)}, y - y_{1(2)}, z - z_{1(2)}). \tag{1.5}$$

The objects visualized by two independent channels of the virtual SMI microscope are the results of the convolution product by a Dirac delta function and the SMI PSF. Thus, as follows after simple calculations, the two independent point like objects are represented by the SMI

PSF centered in the points $\mathbf{R}_1(x_1, y_1, z_1)$, and $\mathbf{R}_2(x_2, y_2, z_2)$, respectively. The axial distance D_{21} between the two objects detected in the two independent channels was determined using a fit function in order to obtain z_{02}, z_{01}. The test fit function is given by the SMI PSF$_z$ (see equation 1.2), where A, B, K z_0, z_1 are the unknown parameters of the fit. In these simulations a least square fit algorithm is used. In each simulation the average total number N_{tot} of detected photons per object is fixed. The evaluated values determined are the mean and the standard deviation. Equation 1.4 was used after adding to each of the objects appropriate Poisson noise corresponding to the number N_{tot} of photons registered per object. To each "true" axial distance this procedure was repeated forty times. In addition simulations were performed where N_{tot} was varied. A different kind of simulations can be realized taking into account the digitization problem.[3] In this case the distance between the two points is not constant but changes every time in the following way:

$$D_{21i} = z_{02} + d_{2i} - (z_{01} + d_{1i}) \qquad i = 1:40; 0 \leq d_{1i} < 1; 0 \leq d_{2i} < 1; \qquad (1.6)$$

where $d_{1(2)i}$ are produced by a random number generator. The evaluated distance (D_d) and its error (ΔD_d) are calculated in the following way:

$$D_d = mean(D_{21i}) \qquad \Delta D_d = \sqrt{\frac{\Sigma_{i=1}^{40}(D_{di} - D_{21i})^2}{40}}; \qquad (1.7)$$

where D_{di} is the result of the fit evaluation of the true distance D_{21i}.

1.4 A first series of simulations

For the present simulations the voxel size was chosen to be, similar to that in a real SMI microscope, i.e. 100(nm) x 100(nm) x 20(nm). The "true" distance assumed was $D = 600$ nm; the two independents point-like objects, detected by two different channels, were assumed to have the same absorption/emission wavelength $\lambda_{ex} = 488$ nm; in this case the PSF FWHM was equal to 600 nm and the FWHM of the oscillating fringes was equal to 80 nm. In the Table 1.1 the mean detected distance values and their standard deviations are shown for several values of N_{tot}.

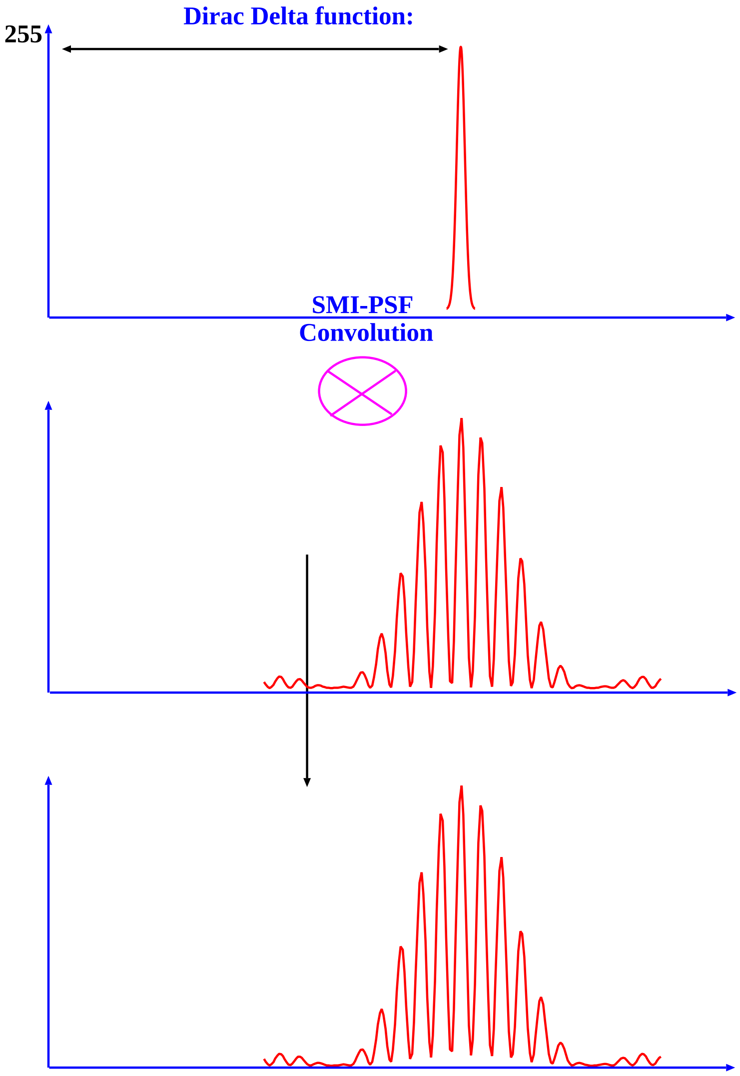

Figure 1.2: Schematic example of SMI-VIM: A point-like object (Dirac delta function visualized here by a narrow Gaussian) is convoluted with the SMI PSF.

As is shown in the Table 1.1, SMI microscopy allows to reach very high precision distance measurements even when a low number of photons is detected. In fact, a total number of detected photons for each object equal to $N_{tot} = 2500$ is sufficient for reach a precision of 1.3 nm. Figure 1.3 shows how the precision distance evaluation (standard deviation) changes with the total number of photons N_{tot} detected in each microscope channel. The standard deviation in distance determination is approximately proportional to $\frac{1}{\sqrt{N_{tot}}}$ (see figure 1.4). One may note, however, that the SMI-VIM simulation allows to give precise estimates of the standard deviations (SD) for each photon count N_{tot} in dependence of the special PSF and image analysis used. As expected, the SD strongly increases at lower photons counts (see Table 1.1).

Table 1.1: Virtual axial SMI-distance determination mean ± standard deviation.
"true" distance: 600 nm (see text for details)

N_{tot}	SMI Distance(nm)
125	599.7 ± 6.8
250	601.1 ± 4.3
500	600.4 ± 3.1
750	599.5 ± 2.8
1250	600.1 ± 2.5
2500	599.7 ± 1.3
5000	599.67 ± 0.93
10000	599.84 ± 0.74
17500	600.12 ± 0.54
25000	599.81 ± 0.46
32500	599.89 ± 0.39
65000	599.72 ± 0.37

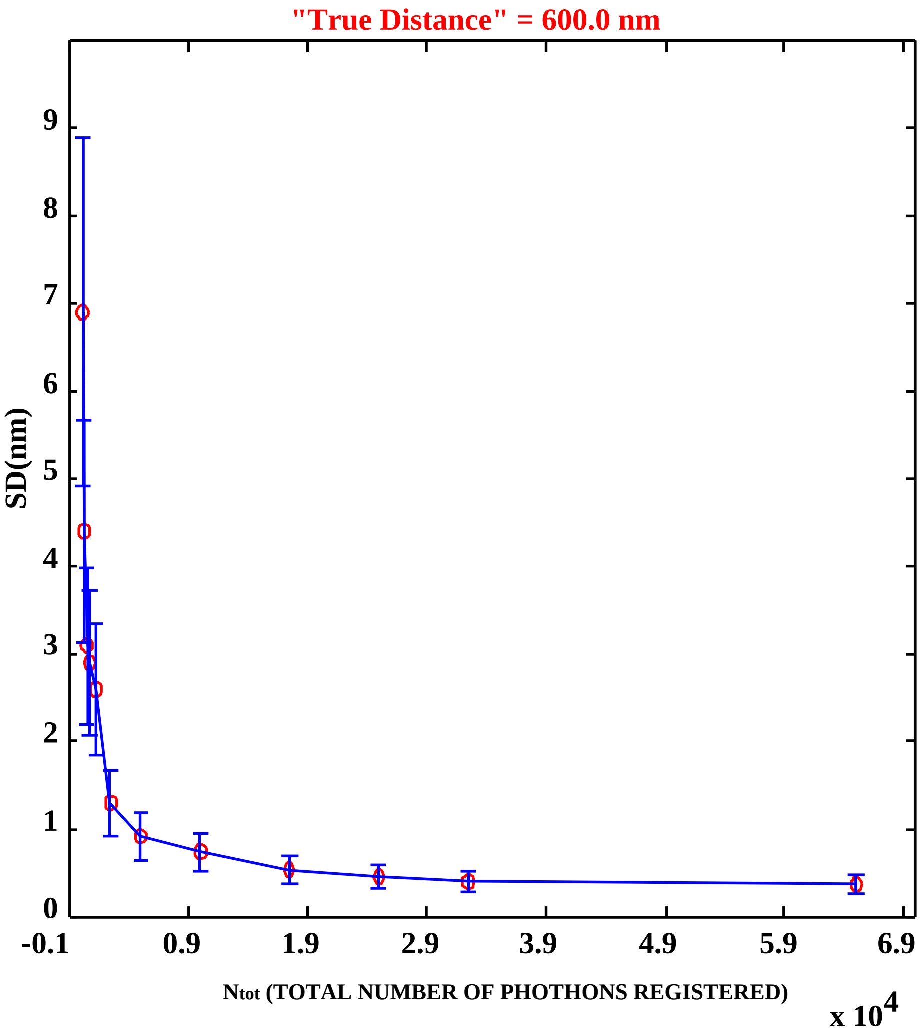

Figure 1.3: Precision of Virtual Axial SMI distance determination.
Ordinate: Standard Deviation (nm) of the SMI distance determined ("true distance": 600.0 nm).
Abscissa: Total number of photons registered per object (see Table1.1 for values).

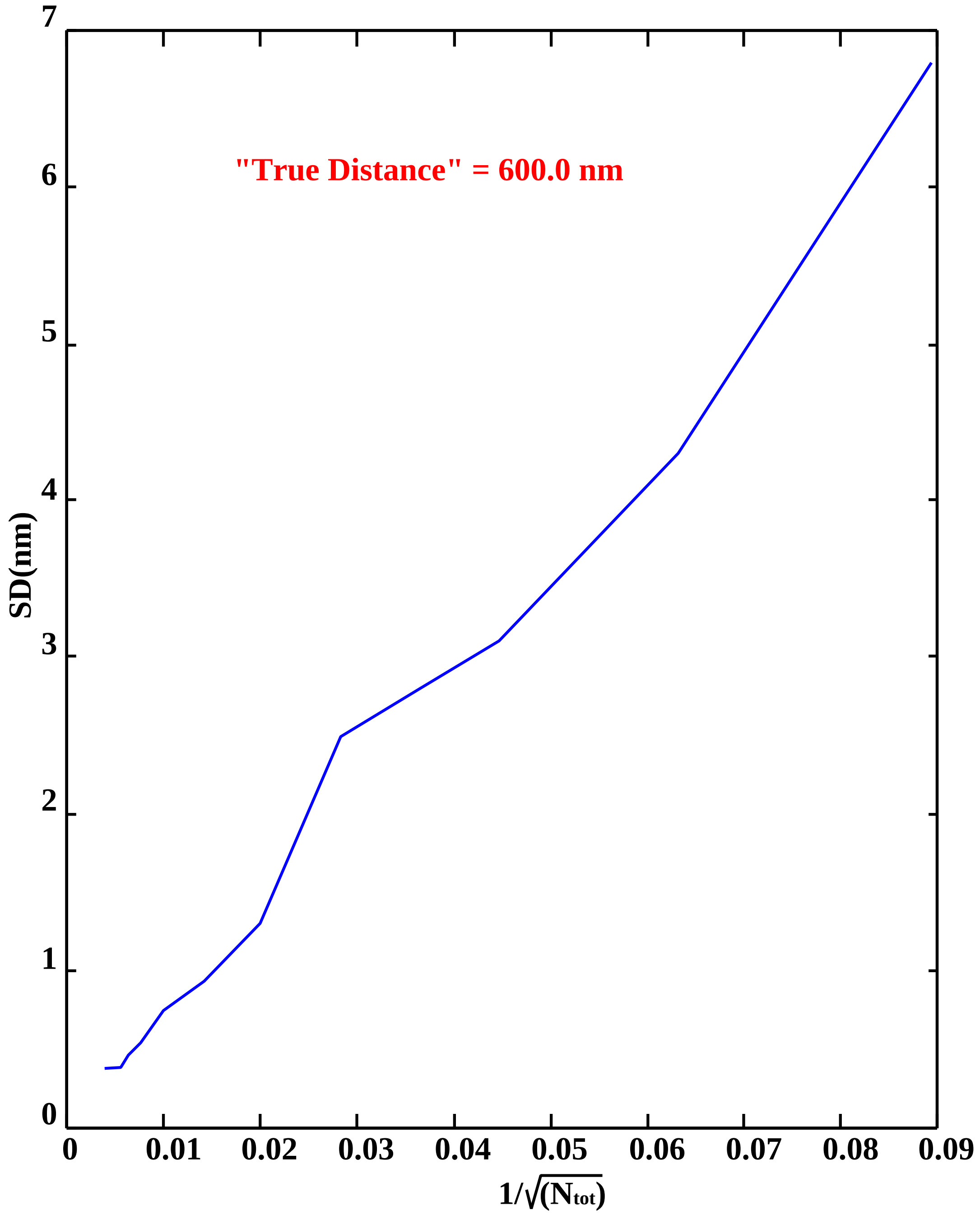

Figure 1.4: Precision of Virtual Axial SMI distance determination.
Ordinate: Standard Deviation (nm) of the SMI distance determined ("true distance": 600.0 nm).
Abscissa: $\frac{1}{\sqrt{N_{tot}}}$, N_{tot} is the number of detected photons per object.

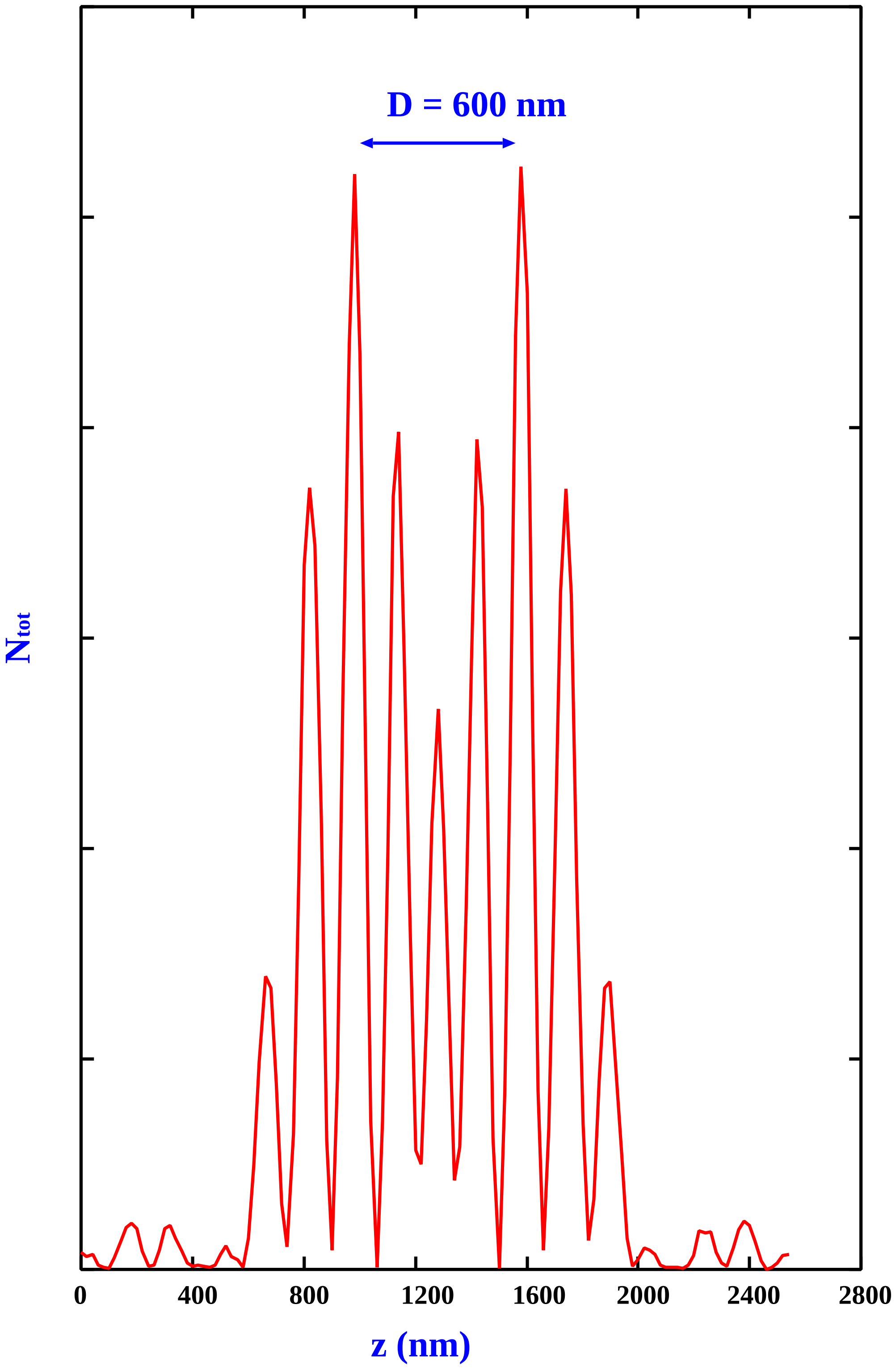

Figure 1.5: Visualization by fluorescence life time of two point like object which distance D in the axial z direction is D = 600 nm.

The results show that even when a low number of photons is detected, the error (standard deviation) in axial distance determination of an SMI microscope is expected to be in the nanometer range. The reason for such a good result can be found considering the shape of the SMI axial point spread function. In fact the error in axial distance determination is not proportional to the FWHM of the envelope of the PSF (FWHM_{SMI}) but to the FWHM of the individual fringes ($\mathrm{FWHM}_f \simeq 80$ nm). Moreover, it is possible to determine axial distances measuring the phase of the fringe oscillations. Here, the precision of axial distance measurements was considered using an absolute distance of 600 nm (i.e. close to the optical resolution limit given by the Rayleigh criteria). Still smaller distances can be determined with a similar precision, if objects with different spectral signatures are used.[17,23,24,25,26] Virtual SPDM SMI simulations indicate that absolute distance measurements down the nanometer range with a standard deviation of one nm are feasible (see next Section).[3]

1.5 Limit in distance resolution evaluated by VIM-SPDM simulations.

Using the SPDM method, distances considerably below 100 nm and with standard deviations in the range of 10 nm and better can be detained using other microscopical methods, such as conventional microscopy[24] or confocal laser scanning microscopy.[17] However, VIM simulations indicate that unmodulated PSFs do not allow nanometer distance measurements at low photons counts and with nanometer precision. This however should be possible using PSF engineered microscope. The limitations of confocal SPDM in the low nanometer/low photon count range may be attributed to two sources: Firstly, as long as different excitation/emission wavelengths have to be used for the registration of objects with different spectral signatures, this contributes significantly to the error of distance determination in the low photon count regime; secondly, with the relatively large FWHM (typically 250-700 nm) of the confocal laser scanning microscopy PSF it is very difficult to localize the respective barycentre centers if their distance decreases to the range of a few nanometers only. Both limitations can be largely overcome by the elimination of chromatic shift errors in combination with PSF-engineering approaches. For example, a 4Pi confocal microscope and simultaneous excitation of the spectral signatures by a mode-locked Ti-Sapphire laser was used to measure the distance of a fluorescent bead to a fluorescent surface; a distance in the order of 60 nm was measured with a precision of 1.2 nm.[27] Here, the results of virtual SPDM computer simulations using SMI PSFs are reported.[10,11,21,22] Since SMI-microscopy so far has only been realized to engineer the axial PSF, the subsequent simulations are restricted to the axial direction. Furthermore, in the following simulations the same excitation as well as the same emission wavelengths are assumed for both spectral signatures. This condition can be experimentally realized as mentioned above by fluorescence life time microscopy.[28,29,30]

The simulations were performed in the following way:[1]

I.) To simulate an object pair, two intensity "Delta" functions of the same height (255 in gray values) with a given axial distance were created in different "channels";

II.) The object intensity distributions were each convoluted with the "ideal" PSF of the SMI-PSF, assuming a wavelength of 488 nm and a numerical aperture of NA = 1.4; both objects were convoluted with the same PSF;

III.) To both data sets (for object 1, and 2), photon noise was added independently, assuming a given number of registered photons N_{tot} per object;

IV.) To detect the position of the objects in the virtual "diffraction images", a least square algorithm was applied to both "images" independently to estimate the positions z_{01} and z_{02} relative to a given coordinate system ("oscillation phase centers") of the two "geometrical image points".

V.) As a result, the "detected distance" between the two objects of a pair was obtained as D(d) (see equation 1.7). A negative value means that an inversion of the object positions in axial direction was detected. Note that using equation 1.7 the error due to the digitization was introduced.

VI.) For each assumed "true axial distance", forty independent simulations as described were performed.

An example is shown in Figure 1.6. In this case, a "true" distance of 5.0 nm was assumed. The resulting two virtual axial SMI-fluorescence intensity distributions (one for each spectral signature) after adding photon noise ($N_{tot} = 1300$) are shown together with the calculated adaptation curves. The distance between the corresponding peaks was 5.2 nm, with a standard deviation SD = 1.0 nm. The result of a virtual SMI-SPDM computer simulation for different "true" distances and low photon numbers is shown in Figure 1.7. A total number of detected photons of $N_{tot} = 1300$ per object was assumed. On the abscissa, the "true" axial distance D_{true} between the two virtual objects is given; on the ordinate, the detected axial distance d_{det} after the virtual microscopy process is plotted. Under the more favorable conditions assumed here (same SMI-PSF for both the signatures), the detected mean distance corresponded well to the "true" distance down to the one nanometer range. For comparison, in Table 1.2 in addition to the SMI case the results are given also for the confocal and the conventional microscopy case; for these cases, the simulations were performed in the same way as for the SMI-case, using ideal conventional and confocal PSFs instead of the SMI-PSF. The results of these simulations indicate that the elimination of different excitation and emission wave lengths improves considerably the detection of correct distances in the low nanometer range even in the confocal and conventional imaging case. One has to consider, however, that the standard deviations of the detected distances are several to many times higher than for the SMI.

Table 1.2: Virtual axial SMI-distance determination mean ± standard deviation."true" distance: 0-40 nm.

"True" Distance (nm)	Conventional Distance (nm)	Confocal Distance (nm)	SMI Distance (nm)
0	1 ± 13	0.5 ± 3.7	0.0 ± 1.1
5	8 ± 12	4.1 ± 3.9	5.2 ± 1.0
15	12 ± 10	16.7 ± 4.4	15.0 ± 1.6
20	23 ± 13	22.3 ± 5.3	19.7 ± 1.3
35	47 ± 11	33.7 ± 3.8	35.2 ± 1.1
40	32 ± 12	39.2 ± 4.3	40.2 ± 1.7

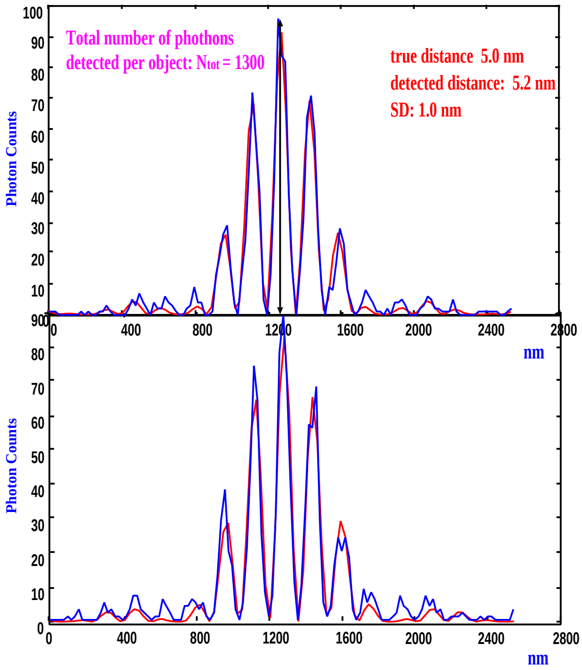

Figure 1.6: Visualization using two independent channels of two point like object which "true" distance D in the axial z direction is D = 5.0 nm .

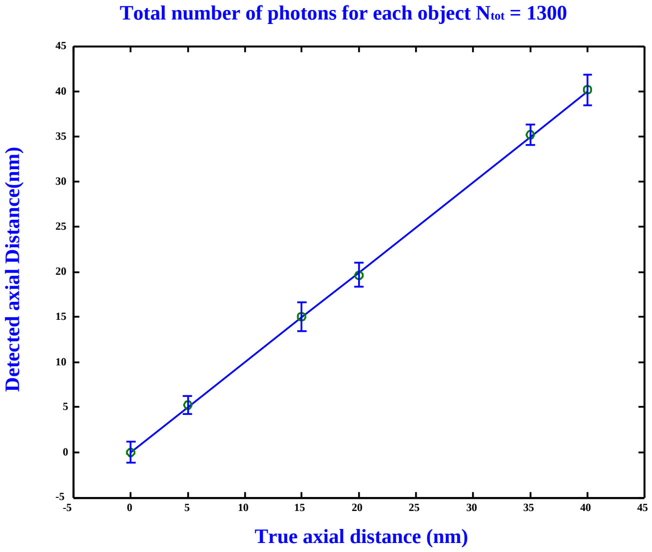

Figure 1.7: Abscissa: "True" distance (nm).Ordinate: Detected distance (nm).

1.5.1 Detailed analysis of topology high resolution determination comparing different microscopical systems

The previously shown simulation were repeated not taking in to account the digitization problem (see equation 1.7). The main procedure of the simulation is the same as described before. No digitization indetermination (”digitation noise”) was added in the present case because this kind of noise is effective only when traditional intensity ”centre of mass” algorithms are applied in order to evaluate the barycentre of an object. Here a least square fit, not subjected to thresholding problems, will be applied on the simulated data in order to measure the distance between two independent point like objects. Expecially equation 1.4 is used when the SMI microscopic system is simulated and equation 1.3 when the evaluation are repeated in the case that a conventional light microscopy PSF and Confocal Laser Scanning microscopy PSF are considered. Furthermore a new case is considered in this new serie of simulations. As will be pointed out in details in Chapter 2, Chapter 3 and Chapter 4, an object which dimension are comparable with the SMI FWHM$_f$ (for $\lambda_{ex} = 488$ nm FWHM$_f \simeq 80$ nm) is charactherized by an AID that differ from PSF. The modulation of the AID will decrease increasing the object axial size. Therefore more the object became big, less it is possible to use the information given by the intensity fringes oscillations. In this Section a new case will be added to the simulations: SMI topology simulation will be performed even in the case that an object with 100 nm axial extension is considered (SMI$_2$). The SMI AID of a 100 nm diameter object is simulated by VIM performing the convolution product between a 3D Gaussian intensity distribution (FWHM = 100 nm) and the 3D SMI PSF. The purpose is clearly to evaluate the SMI limits in topological resolution in a realistic non ideal conditions. The procedure of the simulations is the same as before; different photon count conditions will be simulated. The results shown in Table 1.3 indicate that even under low photon count conditions $N_{tot} = 2500$ high precision topological measurements are feasible with SMI microscopy even in the case in which an extended object is considered. The VIM SPDM simulations show that starting from $N_{tot} = 5000$ it is possible in principle to discrimate distances in the order of 5 nm whatever is the size of the object. A distance of 5 nm correspond to 1/4 of the axial voxel size and to $\simeq 1/100$ of the considered excitation wavelength. The modulation of the excitation light along the axial direction produces a dynamic resolution effect that will be shown better in the final Chapter of this work. Here it will be remarked only that the object placed in a particular position along the optical axis causes a shift in the phase of the standing wavefields; Different axial positions correspond to different local shifts of the modulated standing wavefields. Instead of in conventional and in confocal microscopes even under extremely good conditions e.g axial voxel size equal to 20 nm, it is anyway not possible to discriminate sub voxel distances in any photon count condition. In Figure 1.8 is shown how the estimate of the error e.g. SD vary in different photon count conditions and considering different value of D_{true} (D_{true} = 15 nm, D_{true} = 20 nm), for all the microscopic system considered. Note that in the case of a subvoxel distance D_{true} = 15 nm an asymptotic value of SD is evaluated for the conventional and confocal detection system (respectively SD $\simeq$ 9 nm and SD $\simeq$ 6 nm). In Figure 1.9 the values of the detected distance D are plotted as function of the "true" distance D_{true} for all the simulated microscopic systems; in all the four cases shown the total number of detected photons per object was fixed to be N_{tot} = 2500.

Table 1.3: VIM SPDM simulations:

SMI$_1$ regards VIM SPDM simulation when the SMI microscopical system is simulated and the objects detected are considered to be "point like" (with an axial extension of 10-20 nm).
SMI$_2$ regards VIM SPDM simulation when the SMI microscopical system is simulated and the objects detected is considered to have an axial extension of 100 nm.
Conv. regards VIM SPDM simulation when a conventional microscopic system is simulated.
Conf. regards VIM SPDM simulation when a confocal microscopic system is simulated.

N_{tot}	SMI$_1$	SMI$_1$	SMI$_2$	SMI$_2$	Conv.	Conv.	Conf.	Conf.
	D$_{true}$	D$_{true}$	D$_{true}$	D$_{true}$	D$_{true}$	D$_{true}$	D$_{true}$	D$_{true}$
	0 nm	5 nm	0 nm	5 nm	0 nm	5 nm	0 nm	5 nm
125	0.2 ± 4.3	5.6 ± 4.5	0 ± 14	5 ± 13	9 ± 33	16 ± 36	1 ± 27	6 ± 28
250	0.0 ± 3.3	3.7 ± 3.6	0.1 ± 8.5	3.7 ± 7.1	3 ± 23	6 ± 21	12 ± 18	2 ± 16
500	0.5 ± 2.4	5.7 ± 2.6	0.4 ± 4.7	5.7 ± 5.4	3 ± 15	4 ± 18	3 ± 13	1 ± 14
750	0.1 ± 1.8	5.3 ± 1.5	0.6 ± 4.2	5.3 ± 4.7	0 ± 12	6 ± 14	1 ± 10	2.0 ± 9.1
1250	0.1 ± 1.1	5.1 ± 1.0	1.0 ± 2.9	5.1 ± 2.9	1 ± 10	7 ± 13	0.6 ± 8.1	4.3 ± 7.6
2500	0.04 ± 0.98	5.05 ± 0.98	0.4 ± 2.3	5.0 ± 2.2	0.3 ± 6.6	5.1 ± 11	1.0 ± 4.2	5.0 ± 6.3
5000	0.04 ± 0.69	5.04 ± 0.72	0.2 ± 1.4	5.0 ± 1.4	0.4 ± 4.5	5.1 ± 10	1.0 ± 2.8	5.4 ± 6.4
10000	0.10 ± 0.49	5.23 ± 0.52	0.1 ± 1.3	5.24 ± 0.94	0.7 ± 3.7	6.1 ± 9.9	0.2 ± 2.4	6.4 ± 6.2
17500	0.09 ± 0.36	4.67 ± 0.34	0.00 ± 0.76	4.67 ± 0.89	0.4 ± 2.5	6.2 ± 9.2	0.6 ± 1.7	4.0 ± 6.3
25000	0.06 ± 0.27	4.86 ± 0.22	0.18 ± 0.65	4.86 ± 0.73	0.1 ± 1.8	4.7 ± 8.4	0.1 ± 1.1	6.2 ± 7.1
32500	0.04 ± 0.18	4.94 ± 0.19	0.21 ± 0.63	4.94 ± 0.60	0.1 ± 1.5	4.9 ± 8.9	0.7 ± 0.9	6.1 ± 6.9
65000	0.01 ± 0.16	4.89 ± 0.16	0.04 ± 0.39	4.89 ± 0.42	0.1 ± 1.4	5.4 ± 9.0	0.2 ± 0.8	5.4 ± 6.8
	D$_{true}$	D$_{true}$	D$_{true}$	D$_{true}$	D$_{true}$	D$_{true}$	D$_{true}$	D$_{true}$
	15 nm	20 nm	15 nm	20 nm	15 nm	20 nm	15 nm	20 nm
125	15.2 ± 3.9	20.2 ± 3.8	15 ± 9.6	18.7 ± 9.8	24 ± 34	25 ± 33	7 ± 24	22 ± 28
250	16.8 ± 3.2	19.7 ± 3.1	13.8 ± 5.6	21.7 ± 6.7	15 ± 29	17 ± 26	14 ± 16	19 ± 15
500	15.4 ± 2.6	20.1 ± 2.6	15.6 ± 5.5	21.0 ± 5.6	11 ± 18	17 ± 19	11 ± 13	23 ± 11
750	14.1 ± 1.8	20.5 ± 1.9	16.0 ± 3.8	21.0 ± 5.0	18 ± 15	18 ± 12	17.4 ± 9.0	19.0 ± 9.8
1250	15.3 ± 1.2	20.0 ± 1.4	15.3 ± 3.4	19.4 ± 4.1	15 ± 14	16 ± 10	16.0 ± 7.3	22.3 ± 8.0
2500	16.01 ± 0.95	20.0 ± 1.0	15.2 ± 2.6	20.9 ± 2.1	18.7 ± 11	21.1 ± 6.8	14.9 ± 6.7	19.4 ± 5.4
5000	15.54 ± 0.71	19.91 ± 0.69	15.1 ± 1.5	20.0 ± 1.7	13.4 ± 9.1	19.3 ± 4.1	16.6 ± 6.1	20.6 ± 3.1
10000	14.93 ± 0.53	20.06 ± 0.43	14.78 ± 0.97	20.4 ± 1.6	15.2 ± 8.6	20.1 ± 3.7	15.9 ± 6.4	20.2 ± 2.8
17500	14.73 ± 0.35	19.98 ± 0.36	15.31 ± 0.75	19.88 ± 0.78	16.1 ± 8.7	19.6 ± 2.9	16.7 ± 6.2	20.0 ± 1.9
25000	15.02 ± 0.28	20.08 ± 0.31	15.05 ± 0.61	20.11 ± 0.61	15.1 ± 8.5	19.1 ± 2.2	17.1 ± 6.1	20.1 ± 1.1
32500	15.10 ± 0.19	19.94 ± 0.25	14.88 ± 0.50	20.12 ± 0.51	16.1 ± 8.8	20.0 ± 1.7	15.9 ± 6.8	19.6 ± 0.9
65000	15.03 ± 0.15	20.04 ± 0.19	15.10 ± 0.37	20.08 ± 0.41	15.4 ± 8.8	20.1 ± 1.5	16.6 ± 6.2	19.4 ± 0.7
	D$_{true}$	D$_{true}$	D$_{true}$	D$_{true}$	D$_{true}$	D$_{true}$	D$_{true}$	D$_{true}$
	35 nm	40 nm	35 nm	40 nm	35 nm	40 nm	35 nm	40 nm
125	35.4 ± 4.4	40.0 ± 3.3	36.9 ± 8.8	44.3 ± 9.6	48 ± 37	39 ± 32	29 ± 26	29 ± 23
250	34.3 ± 3.7	39.7 ± 2.6	37.0 ± 6.8	39.7 ± 7.8	32 ± 24	44 ± 21	38 ± 17	36 ± 14
500	34.2 ± 2.5	40.0 ± 1.8	34.7 ± 5.0	39.7 ± 4.5	38 ± 22	40 ± 14	32 ± 14	39 ± 11
750	33.7 ± 1.9	40.0 ± 1.6	34.2 ± 4.5	40.1 ± 4.2	34 ± 15	42 ± 13	35.4 ± 9.3	39.1 ± 9.2
1250	34.6 ± 1.1	39.9 ± 1.4	35.2 ± 3.3	40.3 ± 2.9	36 ± 14	41 ± 10	30.8 ± 7.8	41.6 ± 6.9
2500	35.23 ± 0.95	39.76 ± 0.96	35.0 ± 2.2	39.8 ± 2.3	36 ± 13	39.9 ± 6.1	35.2 ± 6.2	41.0 ± 5.1
5000	35.67 ± 0.68	39.63 ± 0.52	34.8 ± 1.5	40.3 ± 1.3	34.7 ± 9.4	38.8 ± 4.0	36.2 ± 6.5	40.5 ± 3.2
10000	34.85 ± 0.44	39.87 ± 0.39	35.3 ± 1.1	40.02 ± 0.96	35 ± 11	39.9 ± 3.0	34.6 ± 6.6	39.9 ± 2.3
17500	34.97 ± 0.38	39.90 ± 0.35	35.26 ± 0.76	40.01 ± 0.77	34.9 ± 8.8	39.6 ± 2.4	35.4 ± 6.1	39.6 ± 1.9
25000	35.24 ± 0.25	40.01 ± 0.30	35.11 ± 0.71	39.97 ± 0.66	35.2 ± 8.8	40.1 ± 2.2	34.3 ± 6.0	40.1 ± 1.5
32500	35.13 ± 0.21	39.99 ± 0.28	34.94 ± 0.58	39.79 ± 0.61	35.8 ± 8.6	40.4 ± 1.7	35.2 ± 6.7	40.4 ± 0.9
65000	34.94 ± 0.16	40.02 ± 0.15	35.11 ± 0.46	39.97 ± 0.41	35.3 ± 9.4	39.6 ± 1.4	36.1 ± 6.3	39.6± 0.7

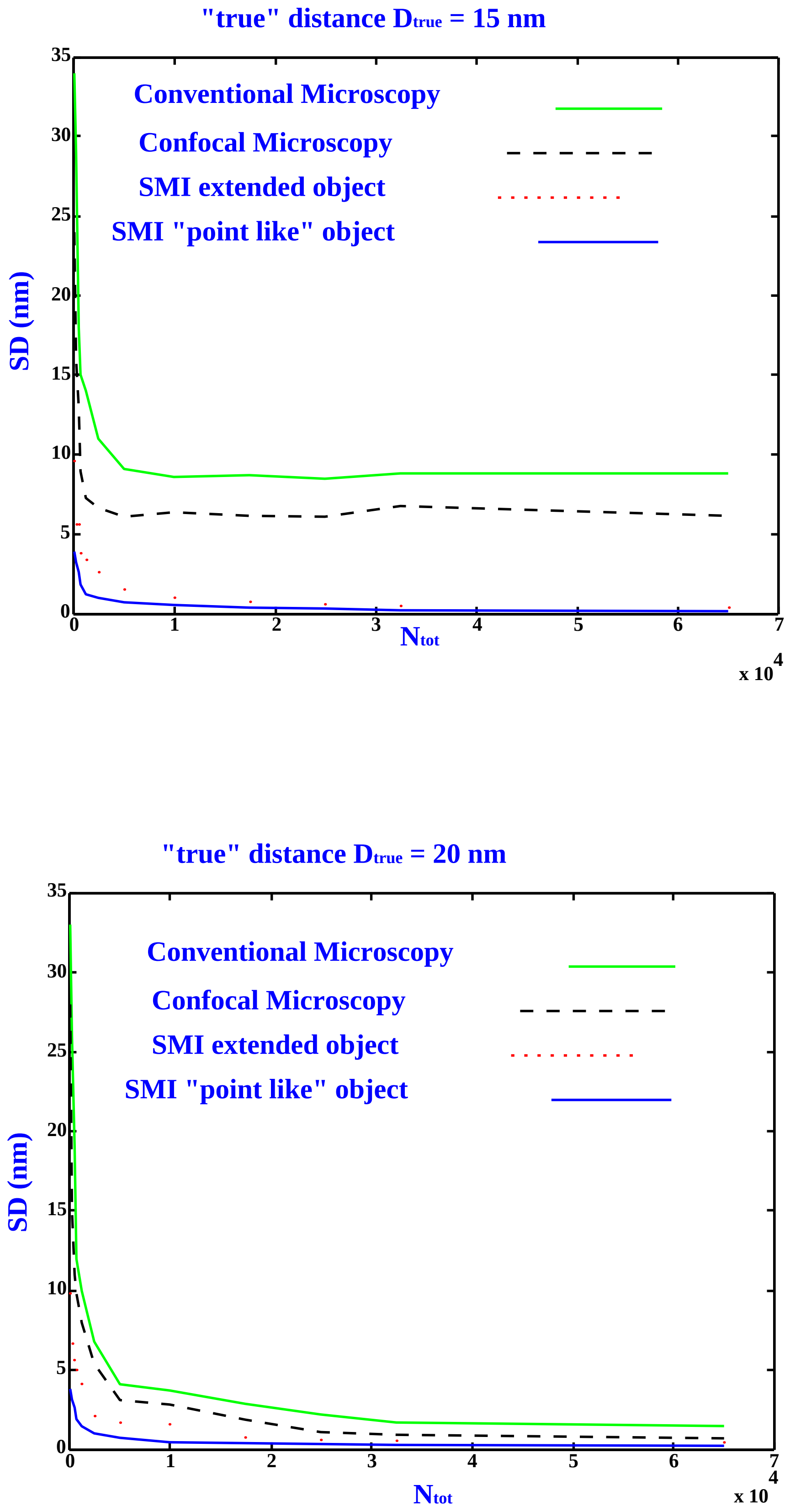

Figure 1.8: abscissa: Total number of detected photons per object N_{tot}.
Ordinate: Estimate of the error in distance measurements SD (nm).

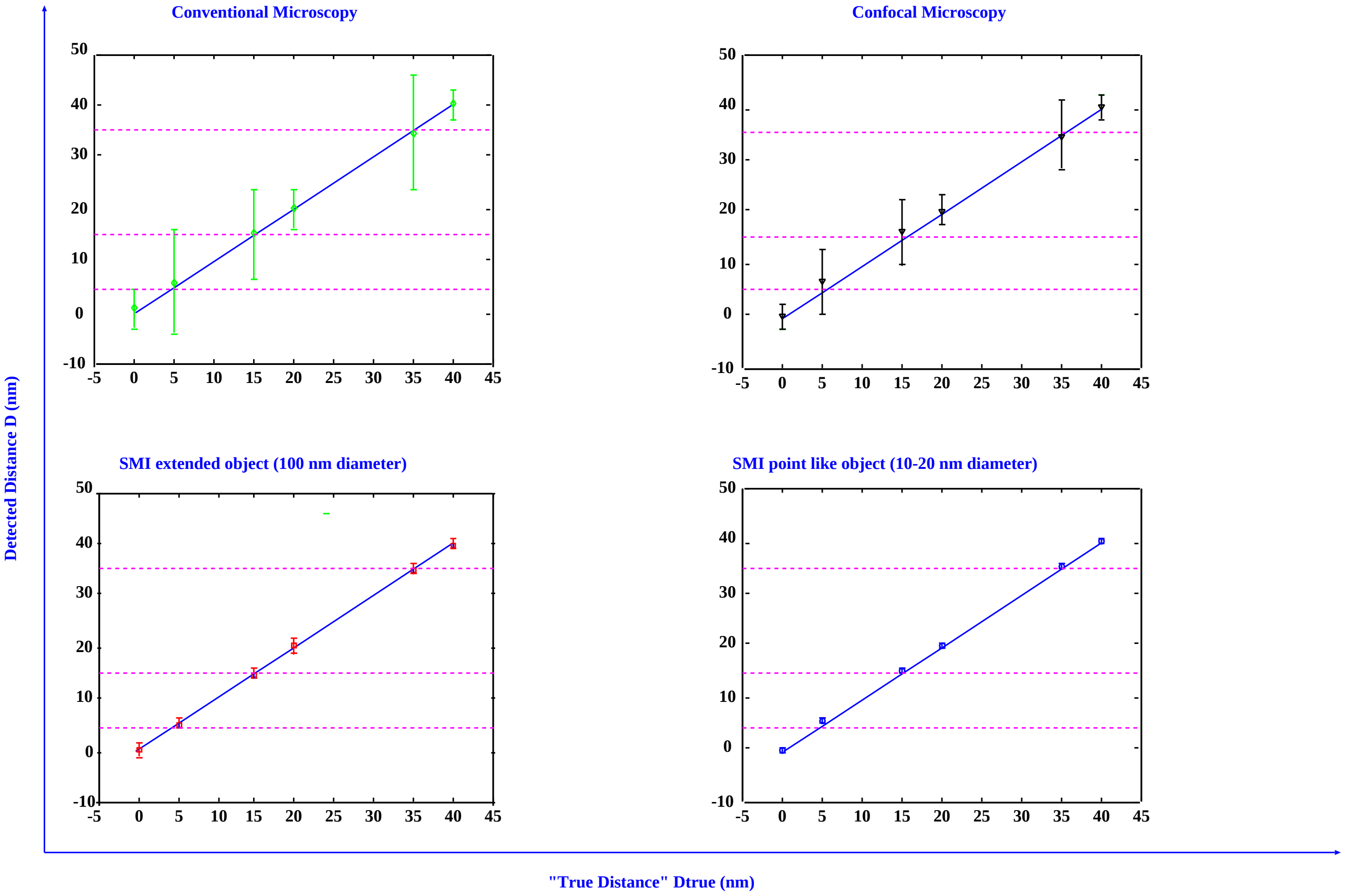

Figure 1.9: Abscissa: "True" distance (nm).Ordinate: Detected distance (nm).

Chapter 2

Object size determinations tools and algorithms performed by SMI Virtual Microscopy

2.1 Introduction

The elucidation of the three dimensional nanostructure of complexes of biological macromolecules ("biomolecular machines") is a major goal of modern biology. For example, specific chromatin regions (composed of DNA and proteins) may form elaborated structures the knowledge of which will be highly important for an improved understanding of the functional topology of the genome[12,14,15,16,38,64] Other examples are the organization and the structure of "transcription factories"[58,59,60,61,62,63] where DNA sequences are transcribed into RNA sequences; the organization of "replication factories"[60] where DNA sequences are doubled; or the organization of nuclear pores and other complexes which regulate the molecular traffic between the nucleus and the cytoplasm of a cell or between a cell and its environment. Although in recent years, the X-ray and electron microscopic (EM) analysis of "biomolecular machines" has made impressive progress, the knowledge of the "in vivo" conformation cannot be replaced by such analyses; especially in the case of weak interactions between the elements forming a biomolecular machine, alterations by fixation are difficult to interprete without a knowledge of the "in vivo" conformation. Furthermore, X-ray and EM analysis do not allow to study the dynamics of individual biomolecular machines in the cellular environment. Both requirements can be solved by "low energy" approaches. While atomic force microscopy and near field optical scanning microscopy (NSOM) allow to study "biomolecular machines" at high resolution if positioned at a surface, an analysis of such structures in the interior of cells would be possible by far field light microscopy only. However, due to the small size of many biomolecular machines (in many cases in the order of a few hundred nm and smaller), until recently Far Field Light Microscopy (FFLM) appeared to be excluded from such studies.

In spite of the general limitations of FFLM.[17,20,25,26] for ultrastructure analysis, valuable structure information can be obtained also by FFLM if special conditions are fulfilled. For example, in many cases the elements (e.g. protein subunits) of biomolecular machines are already well known; thus, the problem of structure analysis can be reduced to the analysis of the reciprocal geometrical relationships between these elements. Spectral Precision Distance Microscopy (SPDM),[23,41,42] in combination with SMI[1,2,3,4,5,6,7,8,9,10,11,12] microscopy and several Point Spread Function (PSF) engineering methods (4Pi , Stimulated Emission Depletion (STED))[18,19,21,22,24,27,28,29,30,31,32,35,37,43,44,45,46,51,57,65,66,67,68] allow to obtain high accuracy nano localization and sub wavelength mutual distance resolution of small targets labelled with different spectral signatures. An equally important topic is the determination of the size of individual nano structures using FFLM. For example, the size of a specific chromatin region in a cell is regarded to have a decisive influence on its genetic activity; thus, such size measurements may provide key information towards a better understanding of the regulation of gene activity. Another example is the identification of functional biomolecular machines by analyzing the colocalization of its elements: It is obvious that a necessary requirement for the proper functioning of a biomolecular machine is that its elements are sufficiently close together; i.e. the diameter of the minimum volume enveloping these elements has to meet certain limits.

In this chapter a far field microscopy approach will be described to obtain informations about the size of individual specifically fluorescent labelled objects with a diameter ranging from about 10 nm to 200 nm using Spatially Modulated Illumination microscopy.

As pointed out several times in the previous Chapter, one of the most important properties of a SMI light microscope is that the excitation light forms an interference fringe pattern along the optical (z) axis.[7,8,9,10,11,12] To achieve this, a collimated and vertically polarised beam of coherent light is focused into the back plane of two opposite objective lenses after it was split in a Mike Zender interferometer. This configurations generates, between the two objective lenses, a standing wave field configuration characterised by $\sin^2$ fringe intensity patters along the optical axis (z). The advantage of this system is that the emission light intensity distribution is modulated by oscillation fringes. Since this modulation is highly sensitive to the size of the object excited to fluorescence this will make it possible to obtain, with the help of image analysis, informations about the size of the fluorescent labelled object along z even if this size is considerably smaller than the excitation wavelength.

2.2 Schematic SMI-VIM object size evaluation model

The basic concept to determine the axial diameter (size) of small fluorescent objects considerably below the optical resolution (d_{op}) of advanced microscope systems (about 500 nm in axial direction) is to calibrate the disturbance of the modulation of the SMI fluorescence intensity diffraction image. To do this, an extended fluorescent object can be represented as the superposition of several "point-like" fluorescent objects, each one emitting light independently with respect to the other. The resulting fluorescence intensity distribution is the sum of the SMI-PSF of each "point-like" object. The SMI-PSF is defined, as in the previous Chapters, as the axial (z) intensity distribution obtained using a truly "point-like" fluorescent object. Here, an extended object represents a fluorescent specimen whose axial extension (size $\mathcal{S}$) starts to be comparable with the Full-Width-at-Half-Maximum ($FWHM_f$) of the individual fringes ($\mathcal{S} > 20$ nm) of the SMI fluorescence intensity diffraction image. Thus an extended object can be replaced by several fluorescent "point-like" objects (an ensemble), each e.g. having a size $\mathcal{S} \leq 10$ nm. The size of the "point-like" fluorescent object can e.g. be characterised by the Full-Width-at-Half-Maximum ($FWHM_o$) of its fluorescent intensity distribution in the object space. Note that for simplicity of argument, here all consideration were restricted to extensions along the optical axis. Following this scheme, it is possible to represent the SMI diffraction axial fluorescence intensity distribution (AID) of this ensemble as the incoherent superposition

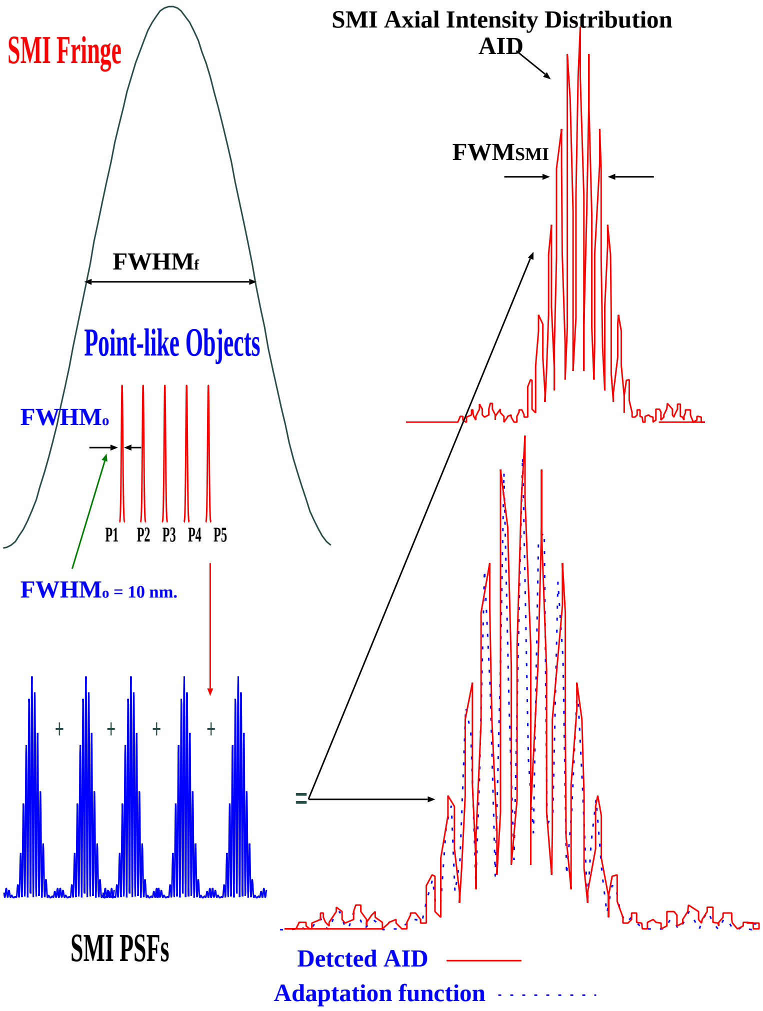

Figure 2.1: An extended fluorescent object is represented as the incoherent superposition of "point-like" fluorescent objects. The axial intensity distribution of an extended object is the sum of the axial intensity distributions (PSF) of each "point-like" object. For a better visualization the fringes and the point like PSFs are not represented in the same scale. The axial intensity distribution on the right side is shown together with the adaptation function used for evaluate size parameters.

of axial PSFs (for more details see Figure 2.1, 2.2). After the sampling size ($\mathcal{S}_f$) is fixed (in this work $\mathcal{S}_f = 10$ nm), the axial intensity distribution depends on the number of (e.g. equally spaced) "point-like" objects and thus on the size $\mathcal{S}$ of the extended object (see Figure 2.2). Increasing the number of "point-like" objects and thus the size of the ensemble, the modulation depth of the axial intensity distribution decreases, although the size range that can be evaluated for each excitation wavelength (λ_{ex}), is limited. In fact, it is not possible to recognize any differences in the axial intensity distribution for $\mathcal{S} \leq 20$ nm ("point-like" condition) and for $\mathcal{S} > 190$ nm (using $\lambda_{ex} = 488$ nm; see the following section). In this case where the specimen approximately corresponds to two times the fringes $\mathbf{FWHM_f}$, the axial intensity distribution does not present any modulation. In the following sections it will be shown how it is possible

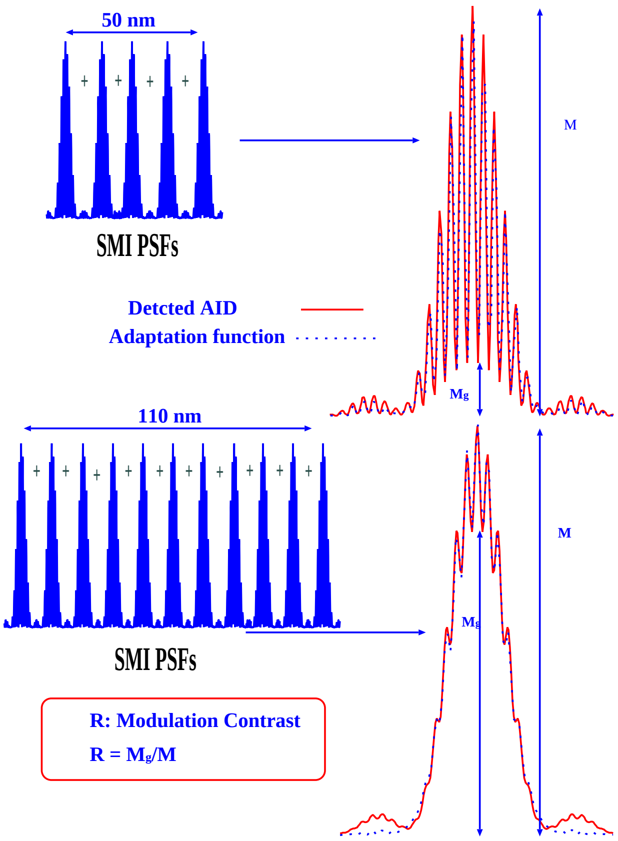

Figure 2.2: Visualization of an example of how the AID depends on the size $\mathcal{S}$ of an extended object computed using an excitation wavelength equal to 488 nm. The extended object was realised either as an ensemble of several "point-like" objects (5 and 11 in the example) with a total extension of 50 nm and 110 nm, respectively, giving rise to 5 and 11 SMI-PSFs being 10 nm apart from each other. To obtain the AID of the extended object, the individual SMI-PSFs are summed up. The resulting AIDs are shown on the right (normalized to magnification factor of one). Note that the modulation contrast $R = M_g/M$ strongly depends on the object size. The same AID was obtained by convolution of an object represented by a Gaussian intensity distribution with an axial $FWHM_{True}$. The $FWHM_{True}$ is equal to the maximum distance between the equivalent object constituted by several point like objects. In the following, it is assumed that the "true size" value of an object is equal to $FWHM_{True}$. For example, the object with an indicated size of 50 nm was represented by a Gaussian with the $FWHM_{True} = 50$ nm. Note that for reason of visualization, the SMI-PSFs are not shown in scale.

to use image analysis to determine the object size along the optical axis and how it depends on the photon count conditions. In the case of spherical objects, this size is equal to the diameter.

2.3 The Nano Size Measurement Algorithm

For the nano size measurement algorithm three dimensional (3D) digital axial intensity distributions (AIDs) produced by SMI-VIM were used. The voxel size of each image was 100 nm X 100 nm X 20 nm. Here, the projection on the z axis of the 3D axial diffraction image intensity distribution AID was calculated. The AID of extended objects symmetrically positioned with respect to the axial SMI-PSF were analyzed Furthermore, it was assumed that 3D distances (D) between an extended object and its nearest neighbor was $D >> FWHM_{SMI}$, where $FWHM_{SMI}$ denotes the Full-Width-at-Half-Maximum of the envelope of the SMI-PSF (corresponding to the FWHM ($FWHM_{SMI}$)) of the detection PSFs. This $FWHM_{SMI}$ can be approximated by connecting the maxima of the individual fringes in the SMI-PSF. To obtain the desired relationship between object size and AID-modulation, it was analyzed by virtual SMI-microscopy how the AID changed on variation of the object size $\mathcal{S}$ (defined here as the maximum distance between the axial positions of two constituting "point-like" object pairs of the extended object). It was found that the depth of the AID-modulation decreased with increasing $\mathcal{S}$ (see Figure 2.2 for example). The principal approach to the quantitative evaluation of the size $\mathcal{S}$ consisted in the study of the ratio between the absolute intensity maxima M and the object "disturbance" maxima M_G under appropriate conditions relates directly to the extended object size $\mathcal{S}$. The "modulation contrast" $R = \frac{M_G}{M} = F(\mathcal{S})$ between the absolute intensity maxima (M) and the maxima of the object "disturbance" M_G was determined by SMI-VIM (see above), taking into account optical numerical aperture, exciting wavelength, index of refraction, emission wavelength as well as fluorescent photon count statistics. The ratio R was studied for the excitation wavelengths: λ_{ex}= 360, 488, 564 and 647 nm. For each excitation condition, the modulation contrast R was computed, varying $\mathcal{S}$. In this case, the AID was calculated as the axial projection of the 3D convolution product between a Gaussian-like object (Full-Width-at-Half-Maximum = $\mathcal{S}$) and the SMI-PSF. Here, extended objects asymmetrically positioned in the fringe patterns where not further considered. A test function $\mathcal{G}(z)$ was used, extracting informations from the axial intensity profile, in order to evaluate $F(\mathcal{S})$. The test function, based on a least square algorithm was:

$$\mathcal{G}(z) = M_1 Sinc^2\Big(\frac{z-z_0}{A}\Big)\Big(\cos\frac{z-z_0}{C}\Big)^2 + M_G Sinc^2\Big(\frac{z-z_0}{B}\Big)^1, \tag{2.1}$$

(for definition of M and M_G see Figure where A, C are positive constants depending on λ_{ex}, B is a positive constant factor, and z_0 is the position of the axial intensity distribution maxima and where:

$$\mathcal{M} = \mathcal{M}_{\mathcal{G}} + \mathcal{M}_1; \tag{2.2}$$

---

[1] Note that $sincu = \frac{\sin(u)}{u}$.

then

$$R = \frac{\mathcal{M}_{\mathcal{G}}}{\mathcal{M}} = \frac{\mathcal{M}_{\mathcal{G}}}{\mathcal{M}_1 + \mathcal{M}_{\mathcal{G}}} = \frac{1}{1 + \frac{\mathcal{M}_1}{\mathcal{M}_{\mathcal{G}}}}. \tag{2.3}$$

In Figure 2.3 , $R = F(\mathcal{S})$ as a function of the object size $\mathcal{S}$ (corresponding to the diameter)

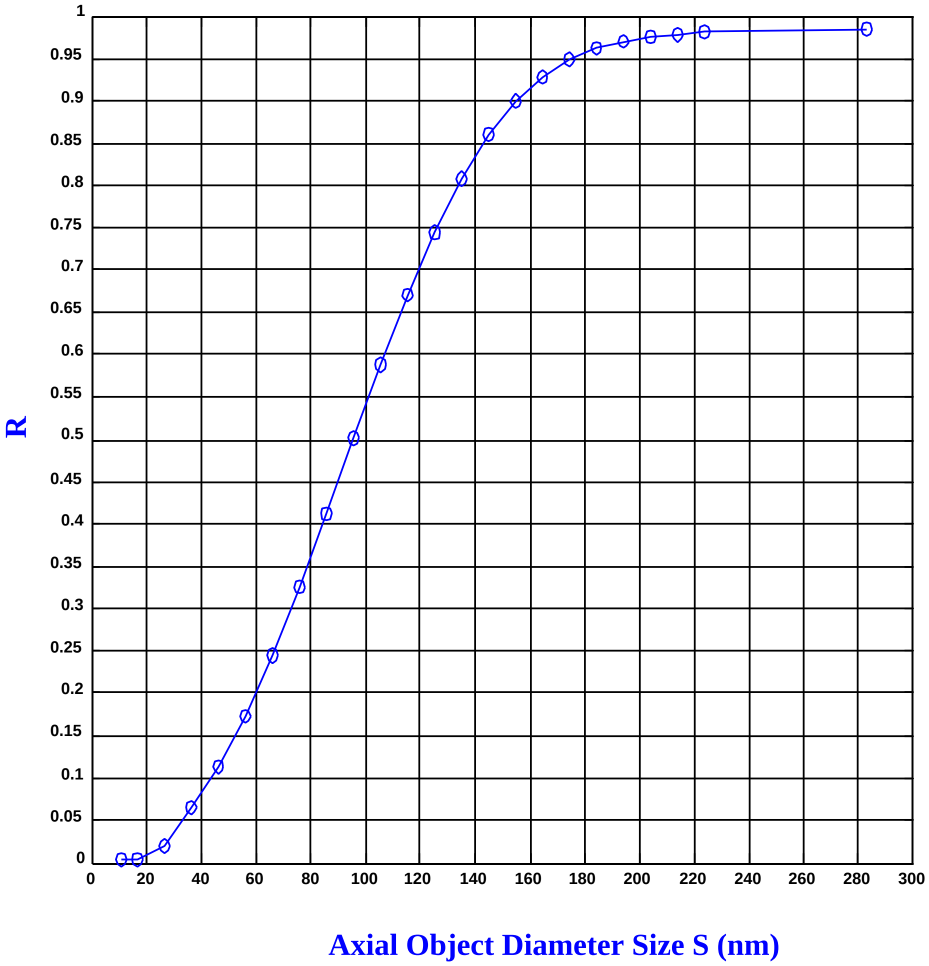

Figure 2.3: In the graph above was visualized the calibration function $R = F(\mathcal{S})$; here the excitation wavelength (λ_{ex}), $\lambda_{ex} = 488$ nm was considered. For sizes smaller then 20 nm, the modulation contrast R is close to zero; this means that the AID, in such a condition, well approximates the theoretical PSF. Increasing the size $\mathcal{S}$ the modulation contrast also increases and the degree in modulation in AID decreases. For ($\mathcal{S} \simeq 160$ nm) the modulation contrast R starts to be close to one and it is not possible to detect any clear information from the AID because it does not presents any modulation in its shape; in this case small changes in the modulation contrast correspond to large changes of size.

is shown for $\lambda_{ex} = 488$ nm. For simplicity, also the emission wavelength (λ_{em}) of the excited fluorescence was set to λ_{ex}. In principle, such a condition can be experimentally determined by e.g. using fluorescence life time microscopy.[28,29,30] In Figure 2.4 , the above mentioned relation $R = F(\mathcal{S})$ is represented for all the wavelengths used here in the SMI-VIM calculations (for more details see Figure 2.3 and Figure 2.4). In order to facilitate the evaluation of huge amount of data and to produce calibration curves for all the possible excitation wavelengths

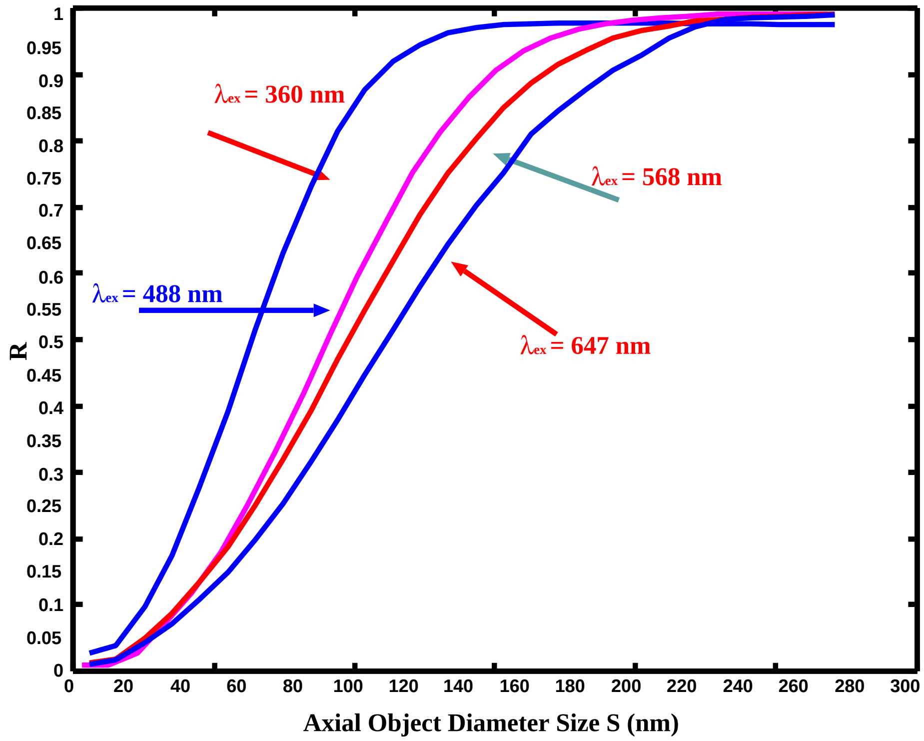

Figure 2.4: In this Figure are shown several calibration function obtained by virtual microscopy using $\lambda_{ex} = 360$ nm, $\lambda_{ex} = 488$ nm, $\lambda_{ex} = 568$ nm, $\lambda_{ex} = 647$ nm. The Figure shows that, varying λ_{ex}, the calibration function $R = F(\mathcal{S})$ changes. Changing λ_{ex}, it is possible to analyze different size ranges under optimal conditions. The smaller the excitation wavelength the smaller the size $\mathcal{S}$ that can be determined. For more details see next chapter

other object size evaluation algorithms will be presented in the following subsections.

2.3.1 Linear Aprossimation algorithm

In a certain size range, being different for different excitation wavelengths, $R = F(\mathcal{S})$ increases strongly with the axial size of the object. In case a spherical object is assumed, $\mathcal{S}$ corresponds to the diameter $\mathcal{D}$ of the object in all directions ($\mathcal{S} = \mathcal{D}$). In a limited range it is possible, evaluating $\mathcal{S}$, to determine the axial object size $\mathcal{S}$ either graphically or with the help of a linear approximation function. This range, as it is expected, depends on the fringe pattern Full-Width-at-Half-Maximum ($FWHM_f$) and varies by changing the excitation wavelength λ_{ex}. A part of the curve $R = F(\mathcal{S})$ can be well approximated by a linear function:

$$R = \left(\frac{\alpha}{\lambda_{ex}}\right)\mathcal{S} + \beta, \qquad (2.4)$$

where α and β are two positive constants,

$$\mathcal{S} = (R - \beta)\left(\frac{\lambda_{ex}}{\alpha}\right). \tag{2.5}$$

The fit parameters α, β were evaluated using all the above cited excitation wavelengths. The resulting mean values and their standard deviations were determined to be:

$$\alpha = 4.18 \pm 0.05, \qquad \beta = -0.27 \pm 0.02. \tag{2.6}$$

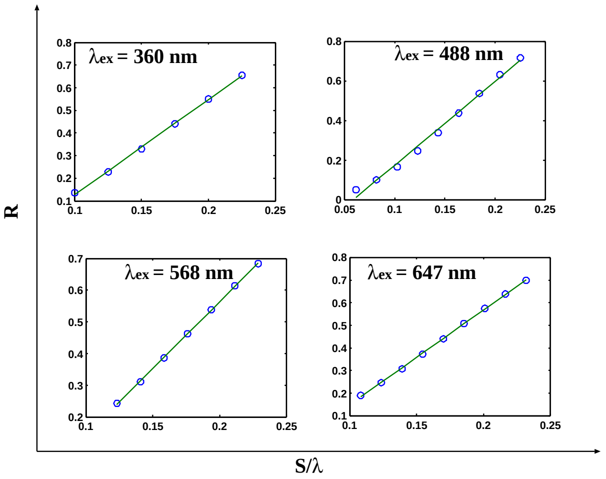

Figure 2.5: A linear relation between the modulation contrast $\mathcal{R}$ and the object size $\mathcal{S}$ can be, under appropriate conditions, determined. The linear coefficients α, β were calculated using all the calibration functions shown in Figure 2.4.

2.3.2 An analytical expression of the modulation contrast R

A further progress in developing SMI-VIM tools for calculating the object size was to determine the analytical expression of the calibration function $R = F(\mathcal{S})$ using the four SMI-VIM calibration function shown in the previous section. Three of the four SMI-VIM calibration functions e.g. $\lambda_{ex} = 360$ nm, $\lambda_{ex} = 568$ nm and $\lambda_{ex} = 647$ nm were used in order to determine the analytical expression of the curves represented in Figure as function of the excitation wavelength (λ_{ex}) and of the object size ($\mathcal{S}$). The analytical expression R =R($\mathcal{S}$,λ_{ex}) of the modulation contrast (R) was determined to be:

$$R = R(\mathcal{S}, \lambda_{ex}) = \frac{1}{1 + +B(\lambda_{ex})^2 \exp -[A(\lambda_{ex})\mathcal{S}]^{C(\lambda_{ex})}}; \tag{2.7}$$

where:

$$A(\lambda_{ex}) = \frac{11.19}{\lambda_{ex}^{0.74} - 65.27}, \tag{2.8}$$

$$B(\lambda_{ex}) = \frac{45.68}{(\lambda_{ex} - 356.69)^{0.23}}, \tag{2.9}$$

and

$$C(\lambda_{ex}) = \frac{1}{1.42 + (11.61)(\exp -0.0081\lambda_{ex})}. \tag{2.10}$$

As a prove of the validity of the algorithm implemented, a comparison between the fourth calibration function measured by virtual microscopy ($\lambda_{ex} = 488$ nm), and $R = R(\mathcal{S}, \lambda_{ex})$ was made. The two calibration functions, in different ways evaluated, were in good agreement as shown by the Figure 2.6. In this way a fast and high precision algorithm to determine the relation between the object size $\mathcal{S}$ and the modulation contrast R was developed, allowing the user to determine such a relation for all the experimentally realised and detected effective wavelengths. A plot of several calibration functions obtained using the previous relation is shown in Figure 2.7.

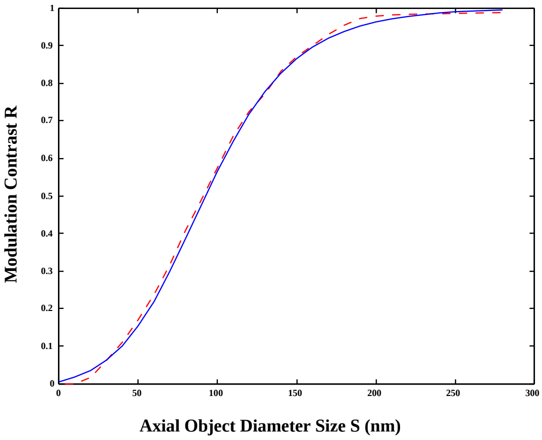

Figure 2.6: In this Figure it is visualized the comparison between the calibration function computed (dotted line) as described in section 2.3, and the analytical expression (continuous line) both considering $\lambda_{ex} = 488$ nm. The good agreement between the VIMs computed modulation contrast R and the its analytical expression can be considered the prove that in the equation 2.7 is shown a valid analytical expression of the modulation contrast R for other values of the excitation wavelength.

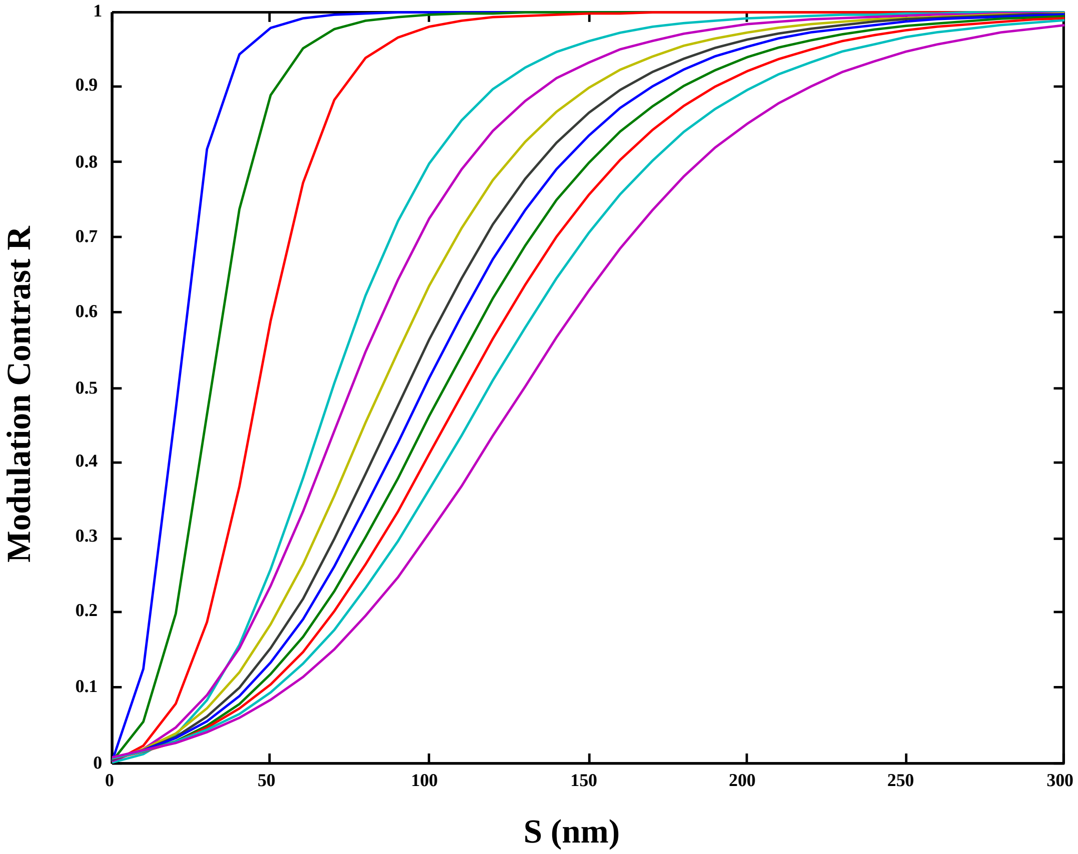

Figure 2.7: In this Example several graphical representations of the calibration function realised are shown using the analytical expression of the modulation contrast R (for more details see section 2.3.2 and equations 2.7, 2.8, 2.9 and 2.10. In the Figure are represented, (starting from left to right) the analytical expression of the modulation contrast R for the following wavelengths: λ_{ex} = 330, 340, 350, 360, 400, 440, 488, 528, 568, 608, 647, 700 nm. The analytical expression for the calibration function can be evaluated in real time regarding the special light excitation conditions in which the system is configured.

Chapter 3

SMI-VIM Size evaluation experiments.

3.1 Introduction

A major obstacle to high resolution light microscopical analysis of small fluorescence objects in biological applications is the low number of detected fluorescence photons; therefore it is necessary to perform extensive SMI-VIM simulations of the effect of photon count noise. It is also interesting to study the effect of photon noise on the algorithms presented in the Chapter 2 in order to point out the practical limit of their use. Expecially, one of the more important goal of this Chapter is to establish a criteria to determine the range of sizes that can be measured using physical relevant excitation wavelengths under normal experimental configurations. Presently will be studied several different configuration using four different excitation wavelengths, λ_{ex1} = 360 nm; λ_{ex2} = 488 nm; λ_{ex3} = 568 nm; λ_{ex4} = 647 nm. This choice is not random; λ_{ex2} = 488 nm and λ_{ex4} = 647 nm actually are the two excitation wavelengths used by the SMI microscope here in Heidelberg; λ_{ex3} = 568 nm is one of the excitation wavelengths used by a normal confocal microscope[33,34,36,39,40,41,47,48,49,50,52,53];λ_{ex1} = 360 nm is frequently used in medicine and it is not a problem to find fluorochromes excitable by this frequency.

Furthermore in this Chapter it will be studied the size algorithm resolution limits; here size resolution limit means, the smaller increment or decrement of size that can be detected by and SMI-microscope with the support of the algorithms introduced in Chapter 2 in a real experiment. In other words it will be point out for each size range e.g. (10-50) nm how big at least should be the difference in in size Δ between two different objects e.g. $\Delta = 5$ nm, $\Delta = 10$ nm, $\Delta = 20$ nm, to be sure that all the measurements regarding one objects are distinguishable from the measurements related to the other object.

Different photon counts conditions will be simulated ranging from a total number of photon detected for object (N_{tot}), N_{tot} = 150, to N_{tot} = 76,800 (for more details see the following sections). The reason of such a choice can be explained thinking how big is a fluorochrome molecule and how many photons it can emits; Normally a fluorochrome molecule has a size in the nanometer range and can emits up to 10,000 photons. Under ideal condition it is possible to assume that a spherical object with a radius of 30 nm can be cover by 6 fluorochrome molecules; Consequently N_{tot} = 60,000 is expected to be detected by a camera after such a object is excited. As it is well known several effects as light dispersion, optical aberrations and last but not least the bleaching of the fluorochrome reduce drastically N_{tot}. Therefore the last section of this Chapter regards a detailed study of SMI-VIM simulations considering that N_{tot} = 9,600 for all the previous mentioned excitation wavelengths, because N_{tot} = 9.600 can be considered as a realist value of the total number of photons detected when small objects e.g. characterized by a size in the 30-40 nm range, are excited.

3.2 Effects of the photon noise on the SMI-VIM tools

The virtual SMI microscope used in this work consist of four independent channels one for each of previous cited excitation wavelength. In each channel, 3D diffraction image intensity distributions were produced for extended objects of a given size $\mathcal{S}$ (the procedure is described in Section 2.2). These 3D intensity profiles are rescaled: The total number of detected photons is considered to be equal to the total integral performed on a given 3D profile. After, a special algorithm is applied for adding photon noise; each voxel value is considered to be the mean value of a Poisson distribution; then a random number genarator substitute the original voxel value with stochastic value extracted by the previous mentioned distribution. Finally from these 3D intensity distribution the projection on the axial z direction (AID) is computed. As a first example in Figure3.1 is shown the effect of the Poisson noise changing N_{tot}. The higher N_{tot} the more noise less and approximating the ideal condition is the AID. Even more interesting is to study how photon noise can effect the calculation of the calibration curves presented in

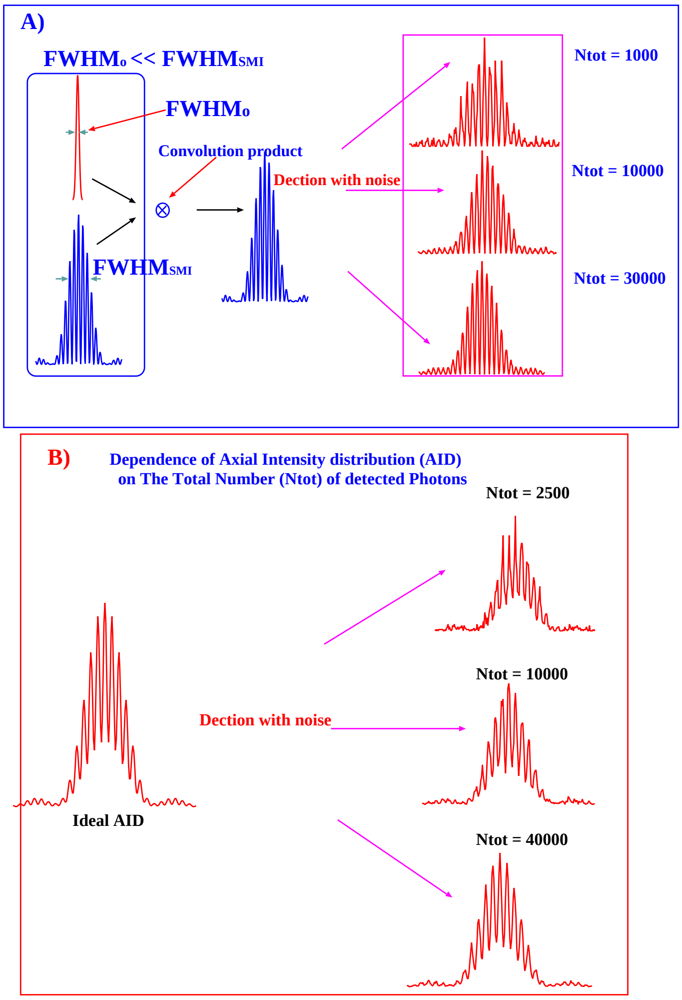

Figure 3.1: A.) SMI-VIM microscopy: on the left side it is shown how VIM is used to compute the SMI-PSF. On the right side is an example regarding the effect of photon noise in SMI-PSF analysis. Three different photon count condition are shown assuming that the photon noise respects a Poisson statistics. As it is shown, the higher the total number of photon (N_{tot}) detected by the acquisition system, the closer to the ideal detection condition shape is the PSF. B.) the same example as in A.) it is shown for the case of the AID of an extended object. One may note that in both cases, the excitation wavelength used was 488 nm and that all the images for reason of clarity are not in scale.

Section 2.3 (see Figures 2.3 and 2.4). This example was made considering only the excitation wavelength $\lambda_{ex} = 488$ nm and few values of N_{tot} (for more details see Figure 3.2). Even in high photon count conditions the presence of photon noise does not allows the possibility of build up an "ideal" calibration function. This is one of the more important reason that justify the use of VIM in order to create evaluation algorithm for SMI microscopy.

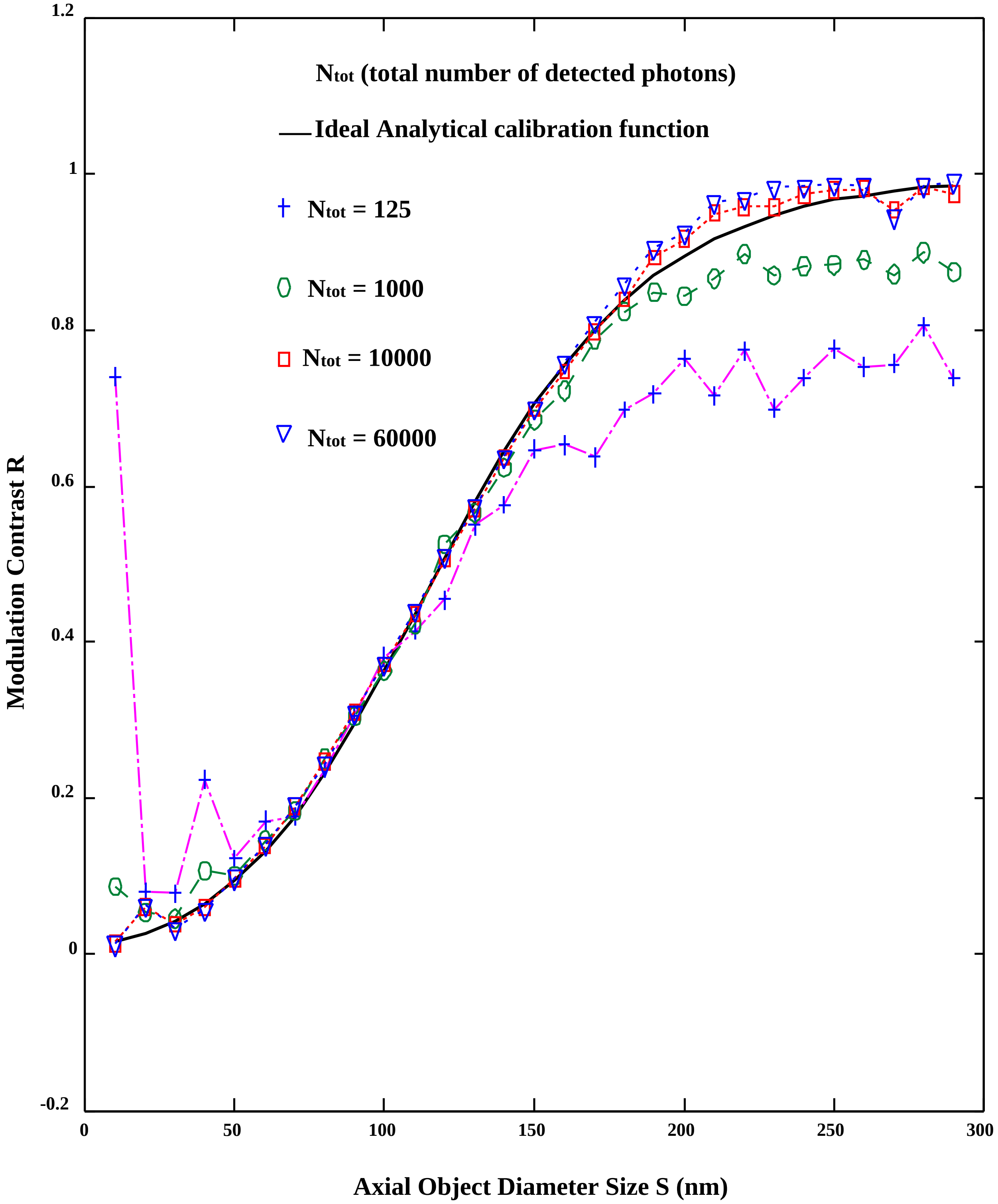

Figure 3.2: Abscissa: Axial Object diameter size $\mathcal{S}$ (nm).
Ordinate: modulation contrast R.
In the Figure, the continuous line refers to the case of noise less "ideal" computation of the analytical calibration function performed by VIM (see equations 2.7-2.10); the dotted lines represent the cases of different photon counts conditions in which Poisson noise was added before starting the evaluations.

3.3 Noise simulations

In this section the results of simulation performed considering the effect of photon noise and using different photon counting conditions are presented. This virtual experiments are focalized to show the experimental limits of size evaluation especially regarding size measurements on objects which diameter is ranging between 10-60 nm, because presently no light microscope are able to evaluate the size of such objects. For this reason the photon count condition $N_{tot} =$ 77,600 will be considered, in the following subsections, as an ideal experimental condition; it is important to remember that a spherical object with a diameter of 30 nm can be covered by 5 or 6 fluorochromes and that each fluorochrome can emits up to 10,000 photons if no other secondary effects as bleaching or dispersion are involved in the emission process. Furthermore the concept of size resolution will be introduced; after a statistical relevant number of independent size evaluations are performed two different object (their size is previously known), are "size resolved", when the histogram of the size evaluation of the first objects is not overlapping the histogram of size evaluation of the other object. The reader have to be careful: this concept is introduced only for the cases in which few size evaluation of the same specimen can be performed. For example if it is possible to realize only one size measurement for two different specimens and the results are 30 nm, 40 nm respectively, this criteria indicates only if it is possible to affirm that the two specimen are related to two different sized objects "case of size resolution" or it is impossible to determine if the specimens are related to two different sized objects or are two different exemplars of the same object ("no size resolution"). Therefore if for some excitation wavelength in some photon count conditions the condition of size resolution (e.g between 30 nm and 40 nm) is not reached this not means that after a statistical relevant series of measurements will be not feasible to discriminate different sized objects in that range.

3.3.1 Noise simulations ($\lambda_{ex} = 360$ nm)

The theoretical calibration curves shown in Chapter 2 (see Figures 2.3, 2.3 and 2.7) suggest that in the size ranges placed in their edges not successful size evaluations can be performed; in that regions small changes of the contrast factor R corresponds to big variation in the object size $\mathcal{S}$. A first virtual experiment (the results are shown in Figure 3.3) regard size evaluations in ideal photon count conditions (N_{tot} = 77,600) ranging from $\mathcal{S}$ = 10 nm to $\mathcal{S}$ = 290 nm. The excitation wavelength used was λ_{ex} = 360 nm and as in all the following simulations typical SMI microscope parameters e.g numerical aperture (NA) (Na = 1.4) etc. were fixed. For each object 40 independent size evaluation were performed; the mean of this measurements was considered as the VIM evaluation of the size and their standard deviation as an estimation of the error. The results shown in Figure 3.3 indicate that with λ_{ex} = 360 nm it is possible to measure the axial projection of the size of objects which dimension is ranging between 10 nm to 120 nm. Another

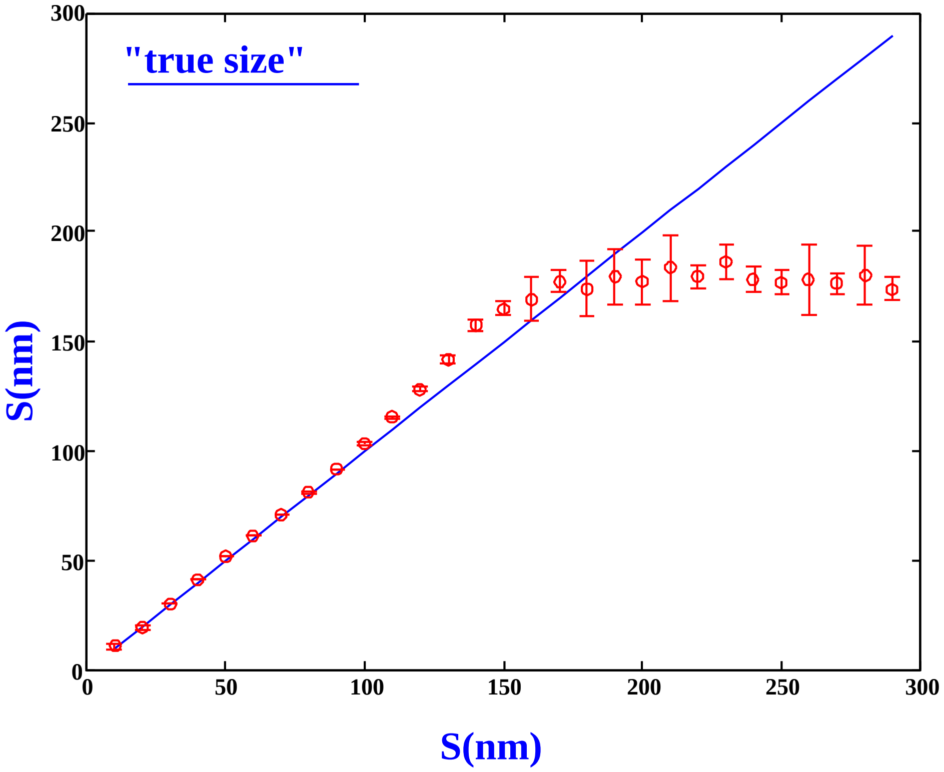

Figure 3.3: Abscissa: "True" Axial Object diameter size $\mathcal{S}$ (nm).
Ordinate: Axial Object diameter size $\mathcal{S}$ (nm). The FWHM of the Gaussian intensity distribution convoluted with the axial PSF in order to produce the AID of an extended object is considered to be the object "true size".

virtual experiment was performed to study the limits in which the previous size measurements can be performed. In other words the goal of the second VIM experiments was to point out the worser photon count conditions that allow to discriminate two objects characterized by different sizes. The criteria to distinguish such objects was established as follow: the mean value M_e of multiple (40) independent evaluations was considered as the estimated value of the size of the given object and the standard deviation SD of that evaluations as an estimation of the error; if M_{e1}, SD_1 and M_{e2}, SD_2 are respectively the evaluation of the size and the error of the object one and the object two, the two object can be "size resolved" when:

$$|M_{e1} - M_{e2}| \geq 3(SD_1 + SD_2) \tag{3.1}$$

if this criteria is fulfilled the distribution of the independent evaluations of the object one is complitely separate by the distribution of the evaluation of the object two. Several different photon count condition were considered (N_{tot} = 150; 300; 600; 1,200; 2,400; 4,800; 9,600; 19,200; 38,400; 76,800); in each photon count conditions the evaluation of objects characterized by different sizes $\mathcal{S}$ ($\mathcal{S}$ = 10 nm; 20 nm; 30 nm; 40 nm;) were performed. Since $N_{tot} \simeq$ 20,000 (for more details see Figure 3.4) it is possible to distinguish all the objects and since $N_{tot} \simeq$ 5,000 it is possible to distinguish all the objects with the exception of the one of 10 nm respect the one of 20 nm. This mean that and realable size resolution of 10 nm starting from object with a size of 20 nm and a realable size resolution of 20 nm starting with object with a size of 10 nm is expected. From the theoretical calibration function (see Figures 2.3, 2.3 and 2.7)

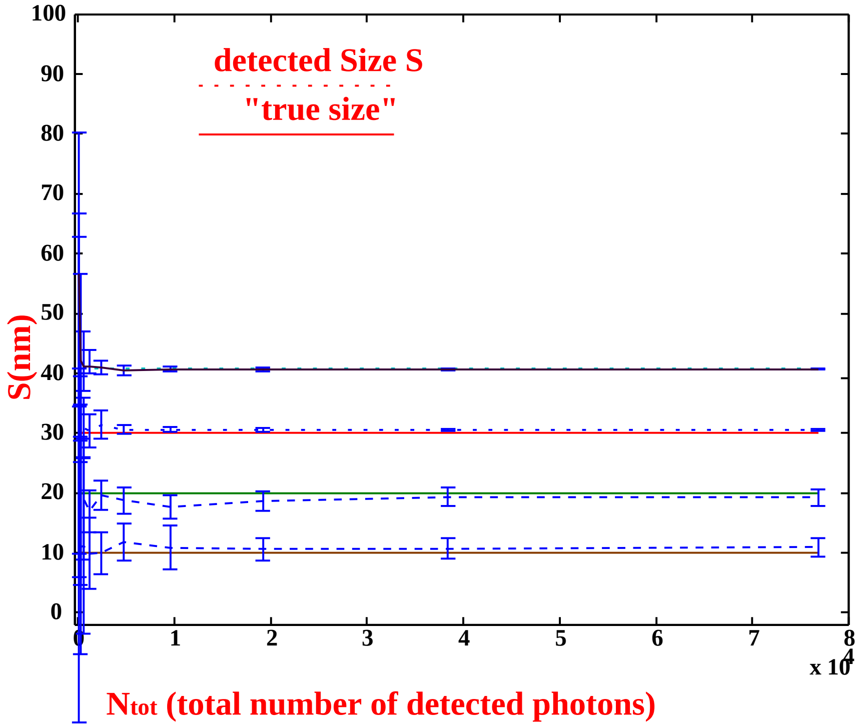

Figure 3.4: Results of simulations regarding "the size resolution".
For a best understanding of the Figure the bars represent the SD of each size evaluation; consequently it is possible looking at the present Figure to apply the criteria described in equation 3.1 (for more details see main text).

it is possible to argue that the accuracy of size evaluation can be higher considering objects which sizes are placed in the middle of that curves; for the present excitation wavelength a good accuracy in size evaluation can be reached measuring objects with "true" size between 30 nm and 80nm. A third virtual experiment was realised in order to confirm this intuitive prevision: for four different photon count conditions (N_{tot} = 150; 1,200; 19.200; 76,800), the variation of the accuracy (proportional to the inverse of SD) considering objects differently sized was studied. The results shown in Figure 3.5 are in agreement with the previous prevision, in fact the region in which the size accuracy is higher (the evaluated SD is smaller) is placed almost in between 30 nm and 80 nm.

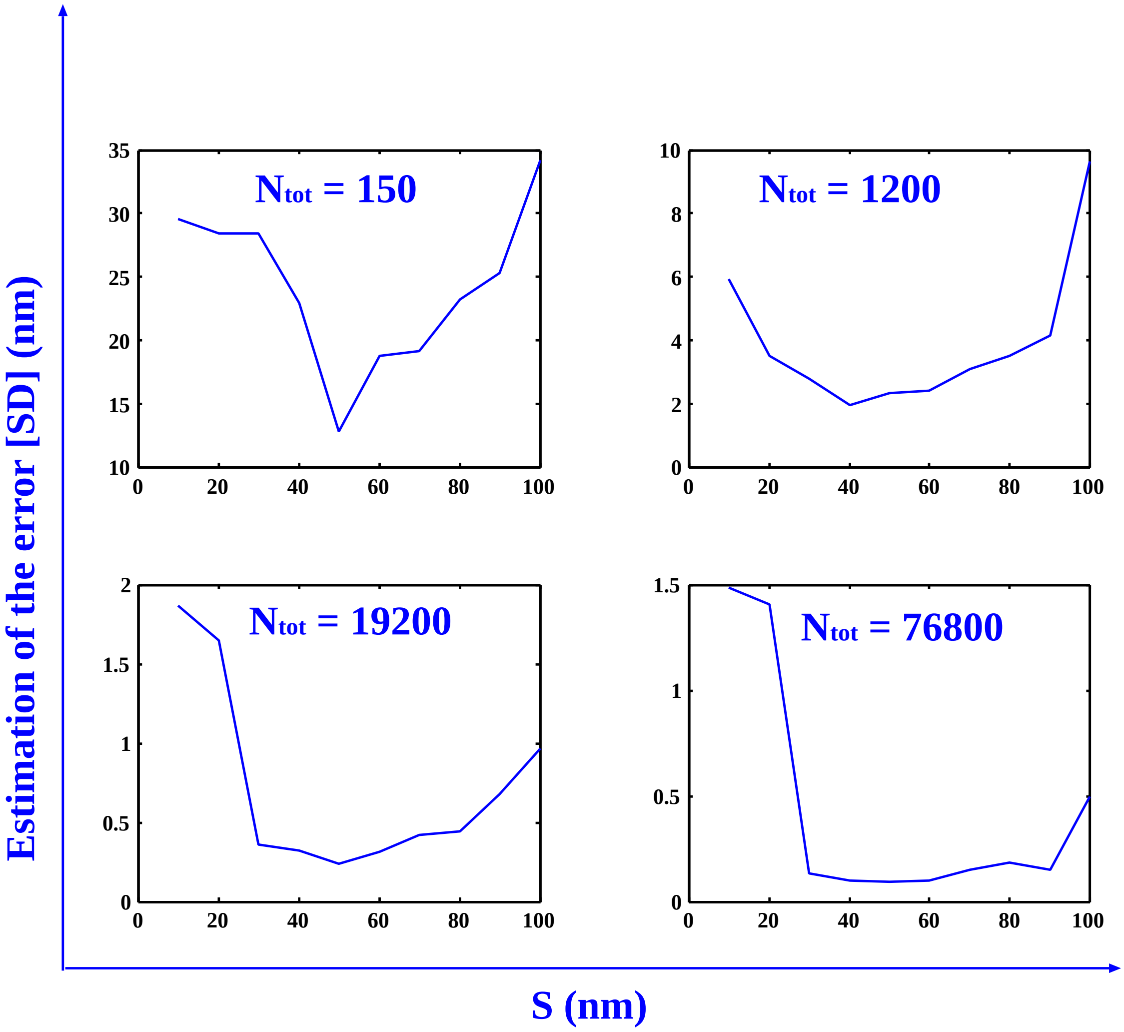

Figure 3.5: Abscissa: Axial Object diameter size $\mathcal{S}$ (nm).
Ordinate: Estimation of the size evaluation error SD.

3.3.2 Noise Simulations ($\lambda_{ex} = 488$ nm)

The same simulations as in the previous section were performed. Here an excitation wavelength $\lambda_{ex} = 488$ nm is considered. Figure 3.6 shows that size measurements from 20 nm up to 130 nm are reliable. Figure 3.7 shows that no "size resolution" conditions can be reached for objects which size range between 10 nm and 30 nm; a "size resolution" of 10 nm is reached since N_{tot} = 19,200 starting from the value $\mathcal{S}$ = 30 nm. The best size evaluation accuracy was reached when $\mathcal{S}$ varied between 50 nm and 100 nm (for more details see Figure 3.8).

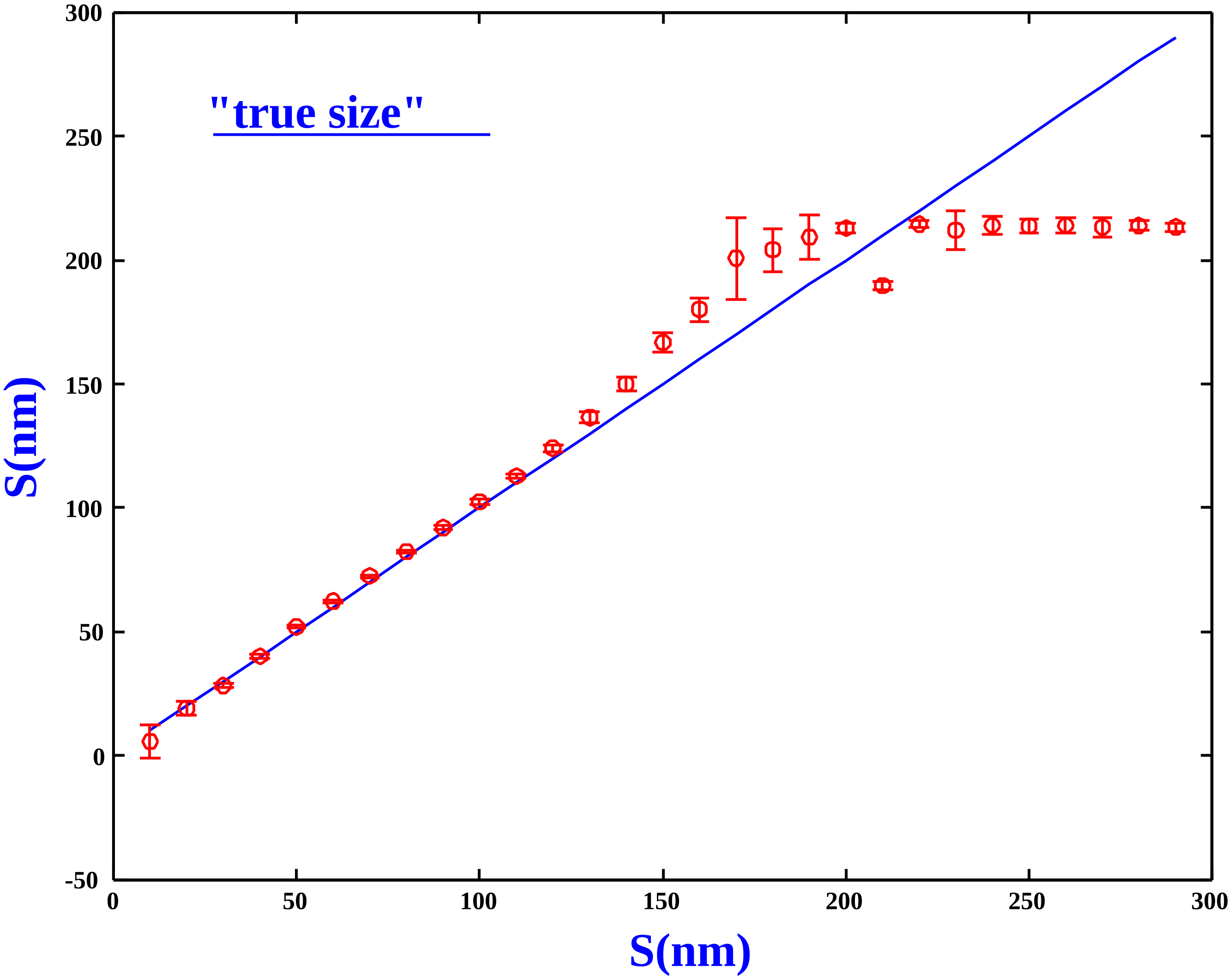

Figure 3.6: Abscissa: "True" Axial Object diameter size $\mathcal{S}$ (nm).
Ordinate: Axial Object diameter size $\mathcal{S}$ (nm). The FWHM of the Gaussian intensity distribution convoluted with the axial PSF in order to produce the AID of an extended object is considered to be the object "true size".

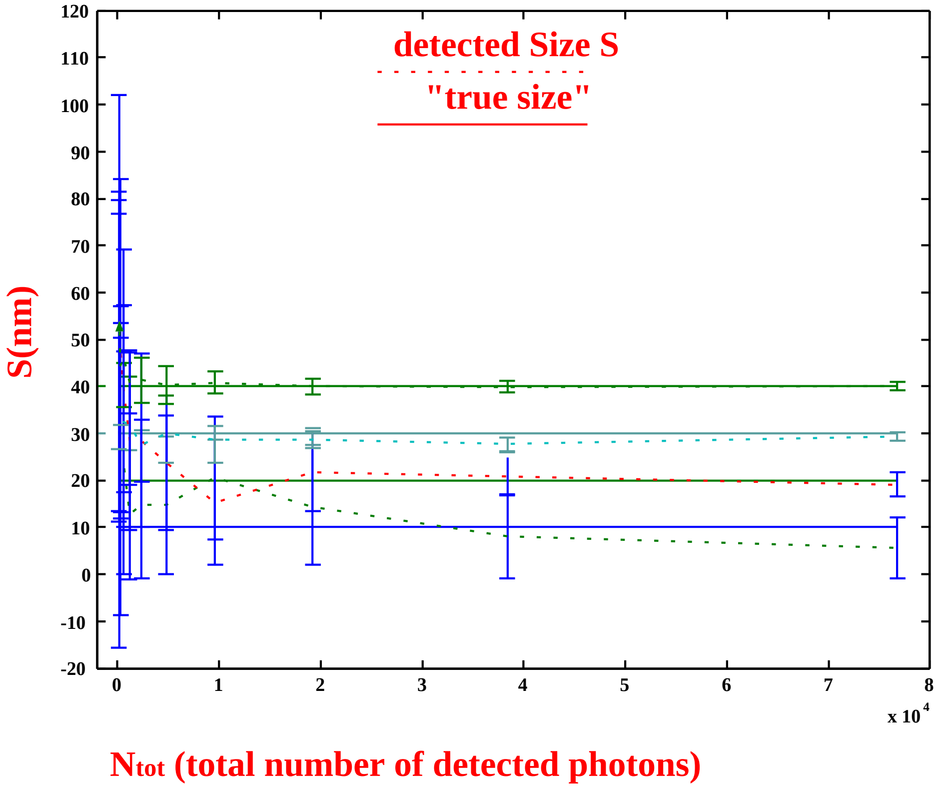

Figure 3.7: Results of simulations regarding "the size resolution".
For a best understanding of the Figure the bars represent the SD of each size evaluation; consequently it is possible looking at the present Figure to apply the criteria described in equation 3.1 (for more details see main text).

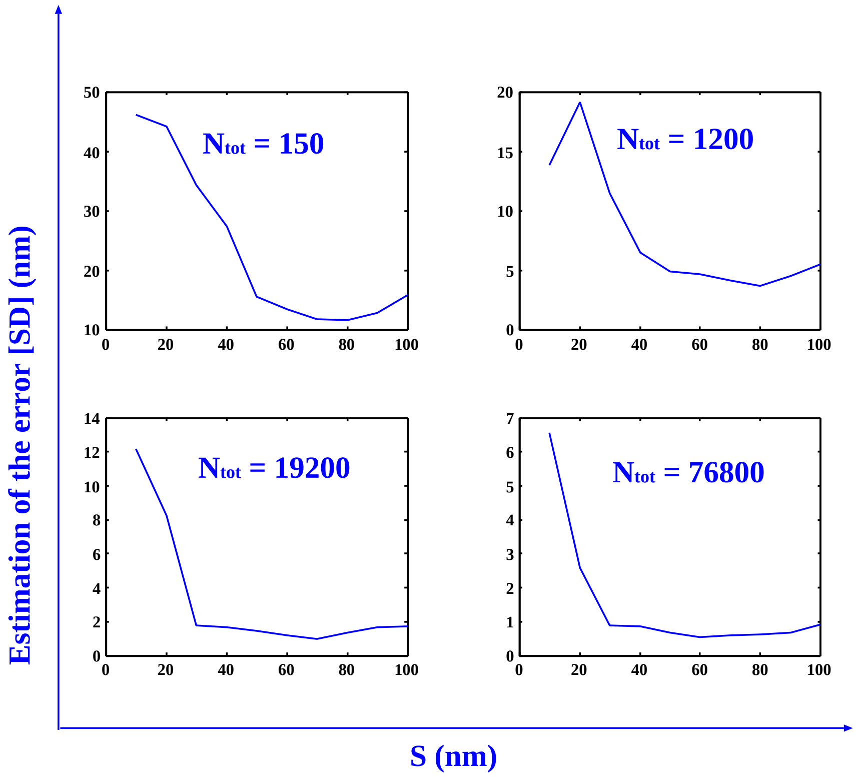

Figure 3.8: Abscissa: Axial Object diameter size $\mathcal{S}$ (nm).
Ordinate: Estimation of the size evaluation error SD.

3.3.3 Noise Simulations (λ_{ex} = 568 nm)

The same simulations as in the section 3.3.1 were performed. Here an excitation wavelength λ_{ex} = 568 nm is considered. Figure 3.9 shows that size measurements from 40 nm up to 150 nm are reliable. Figure 3.10 shows that no "size resolution" conditions can be reached for objects which size range between 10 nm and 40 nm; a "size resolution" of 20 nm is reached since N_{tot} = 19,200 starting from the value $\mathcal{S}$ = 40 nm. A size resolution of 10 nm can be reached stating from $\mathcal{S}$ = 50 nm, N_{tot} = 36,400. The best size evaluation accuracy was reached when $\mathcal{S}$ varied between 60 nm and 110 nm (for more details see Figure 3.11).

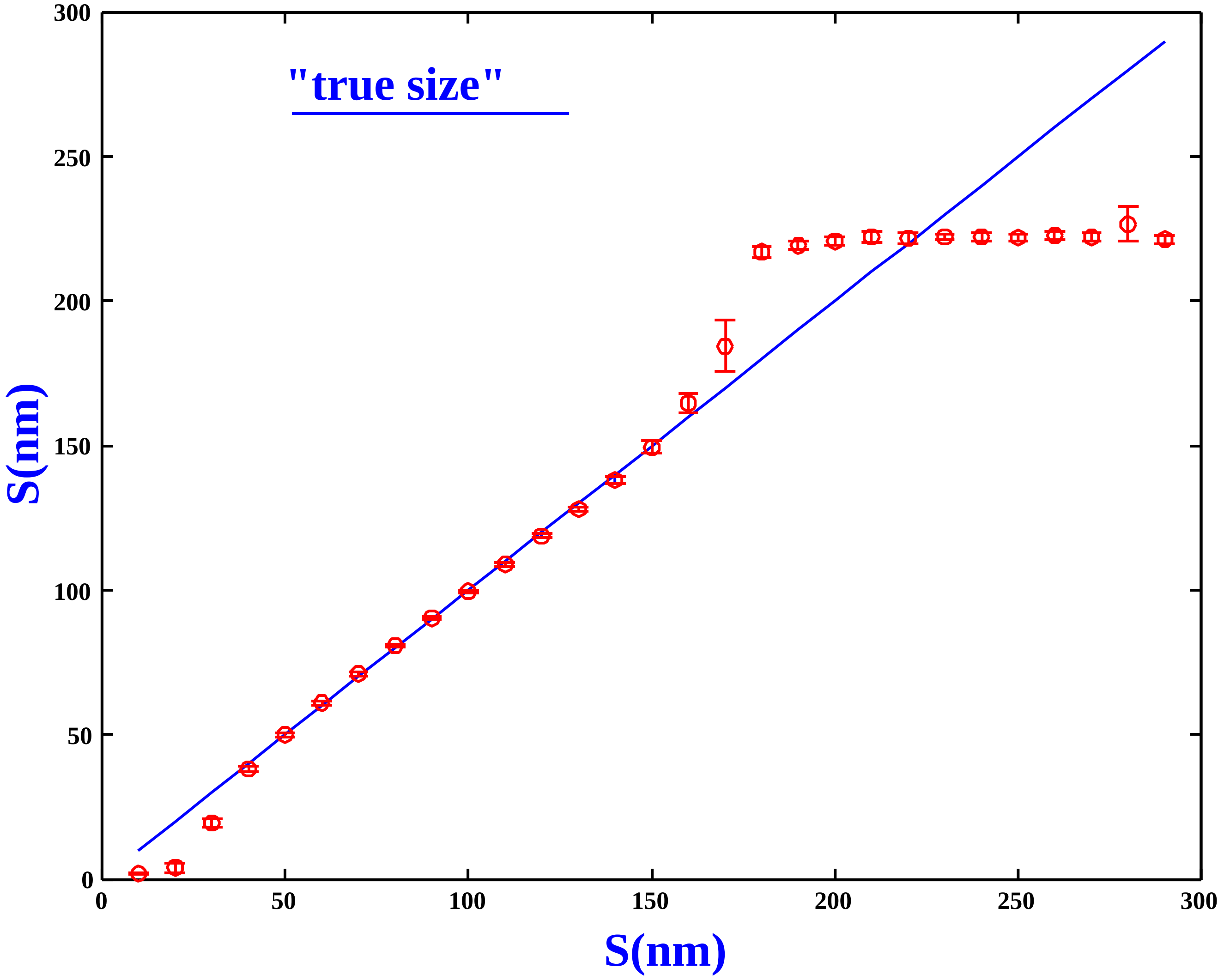

Figure 3.9: Abscissa: "True" Axial Object diameter size $\mathcal{S}$ (nm).
Ordinate: Axial Object diameter size $\mathcal{S}$ (nm). The FWHM of the Gaussian intensity distribution convoluted with the axial PSF in order to produce the AID of an extended object is considered to be the object "true size".

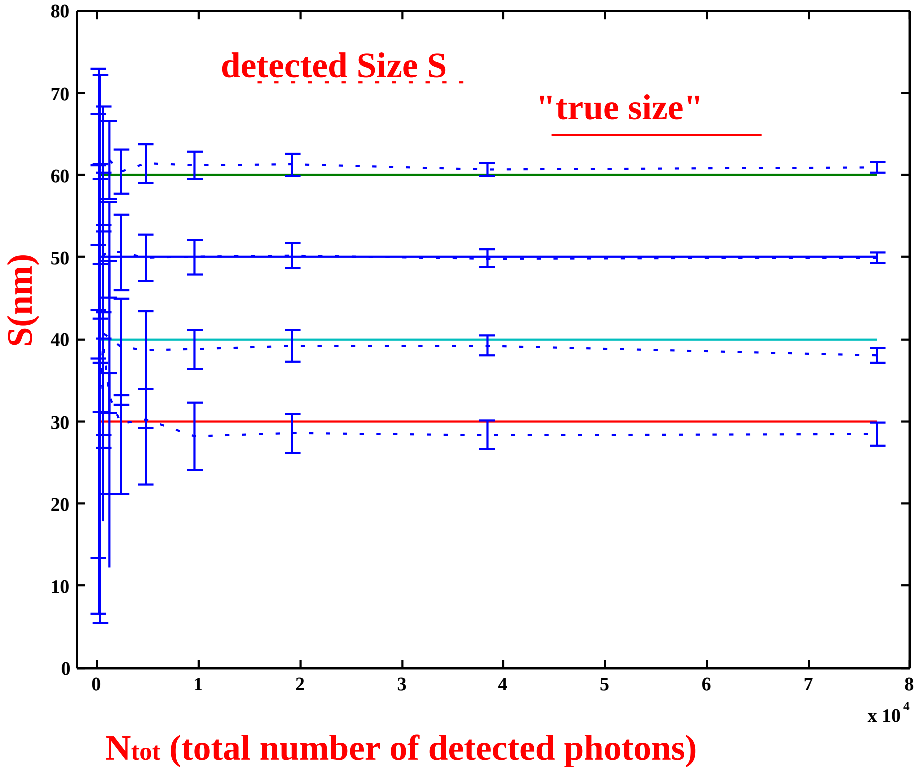

Figure 3.10: Results of simulations regarding ”the size resolution”.
For a best understanding of the Figure the bars represent the SD of each size evaluation; consequently it is possible looking at the present Figure to apply the criteria described in equation 3.1 (for more details see main text).

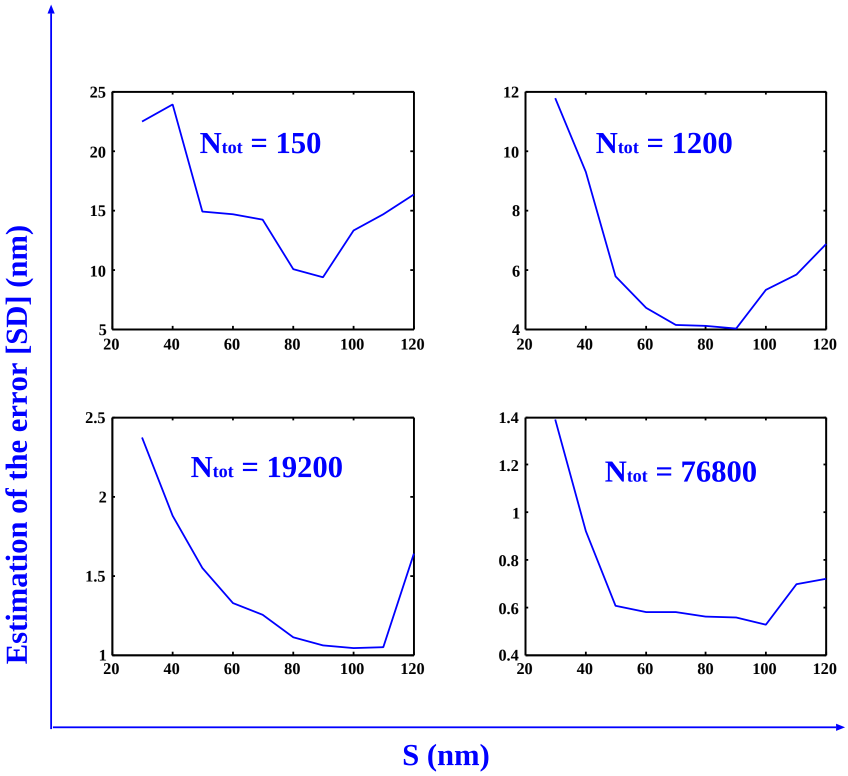

Figure 3.11: Abscissa: Axial Object diameter size $\mathcal{S}$ (nm).
Ordinate: Estimation of the size evaluation error SD.

3.3.4 Noise Simulations (λ_{ex} = 647 nm)

The same simulations as in the section 3.3.1 were performed. Here an excitation wavelength $\lambda_{ex} = 647$ nm is considered. Figure 3.12 shows that size measurements from 40 nm up to 180 nm are reliable. Figure 3.13 shows that no "size resolution" conditions can be reached up to 60 nm; The best size resolution accuracy was reached when $\mathcal{S}$ varied between 80 nm and 120 nm (for more details see Figure 3.14). Then it is possible to bet that a size resolution of 10 nm can be reached ranging from $\mathcal{S} = 80$ nm to $\mathcal{S} = 120$ nm (results not shown).

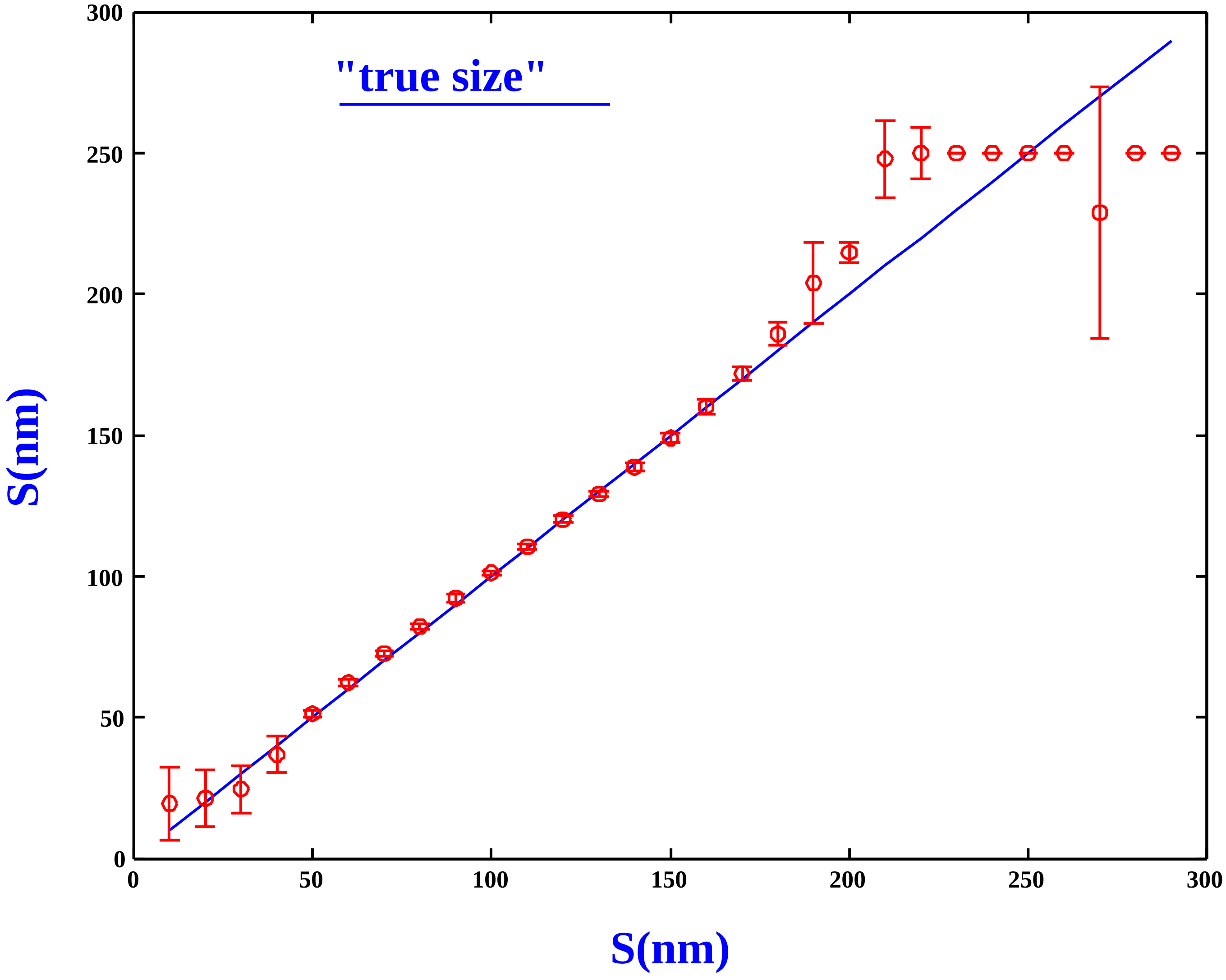

Figure 3.12: Abscissa: "True" Axial Object diameter size $\mathcal{S}$ (nm).
Ordinate: Axial Object diameter size $\mathcal{S}$ (nm). The FWHM of the Gaussian intensity distribution convoluted with the axial PSF in order to produce the AID of an extended object is considered to be the object "true size".

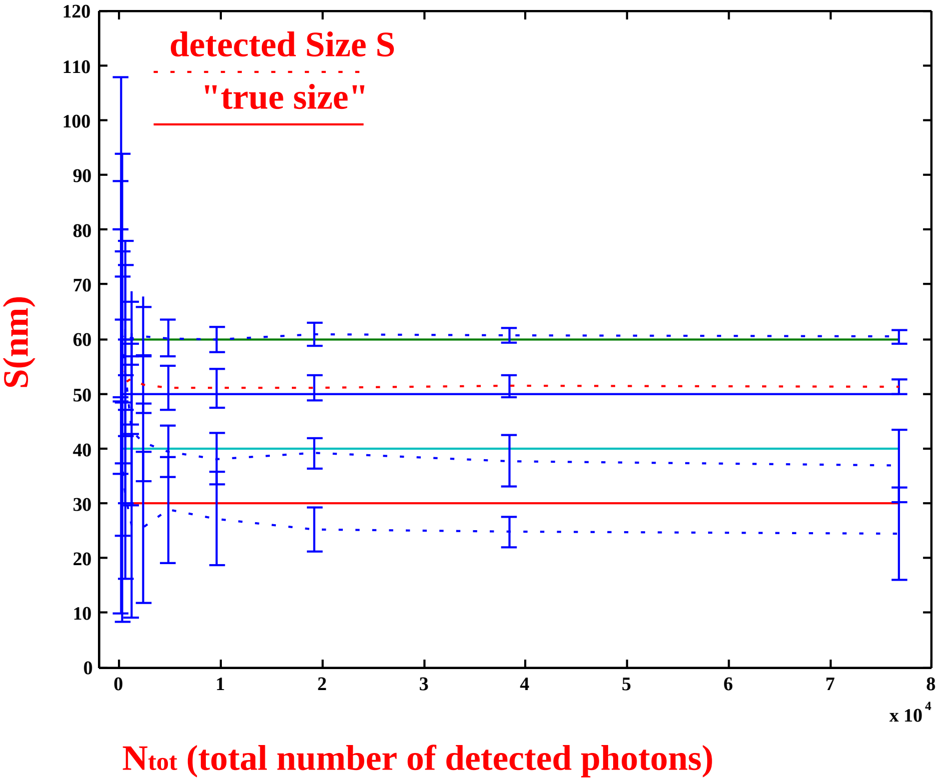

Figure 3.13: Results of simulations regarding ”the size resolution”.
For a best understanding of the Figure the bars represent the SD of each size evaluation; consequently it is possible looking at the present Figure to apply the criteria described in equation 3.1 (for more details see main text).

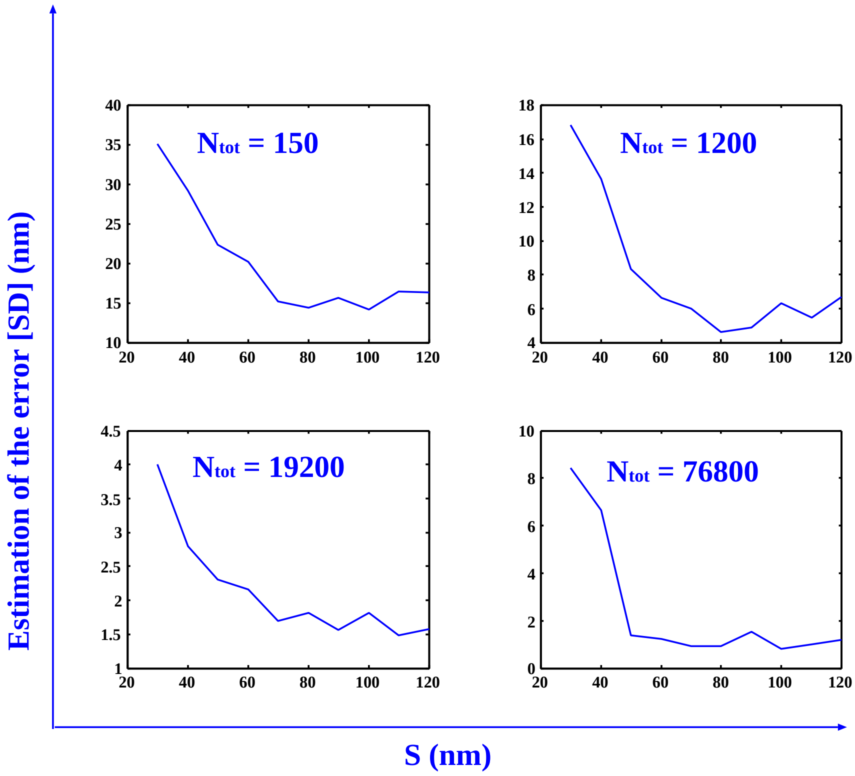

Figure 3.14: Abscissa: Axial Object diameter size $\mathcal{S}$ (nm).
Ordinate: Estimation of the size evaluation error SD.

3.4 Noise Simulations special case $N_{tot} = 9600$

The SMI-VIM simulations allowed to estimate the theoretical limits of size measurements in each channels. As an example, the total number of detected photons was fixed to be N_{tot} = 9,600. Before performing image analysis of the virtual data, appropriate Poisson noise was added to the 3D intensity distribution of the objects; for each specimen, 40 different acquisitions were made. In addition, two other conditions were studied: In the first λ_{ex} and λ_{em} (emission wavelength) were assumed to be the same; in the second, $\lambda_{em} \neq \lambda_{ex}$was assumed.

In Figure 3.15 the comparison is shown between an ideal calibration function $R = F(\mathcal{S})$ and the result obtained in the non ideal photon count condition (N_{tot} = 9,600) described above. The large vertical bars represent the region where the modulation is low due to instabilities in the calculation of the adaptation function. In Table 3.1, the results of the SMI-VIM simulations for $R = F(\mathcal{S})$ assuming $\lambda_{em} = \lambda_{ex}$ (360 nm; 488 nm; 568 nm; 647 nm) and N_{tot} = 9,600 photons, are listed. For each wavelength, the axial sizes were determined using the graphical visualization of the calibration function (see Figure 2.3, 2.4), columns B, or the linear approximation formula, columns C, starting from the detected values of the parameter R. As expected, the accuracy in evaluation depends on the "true" size $\mathcal{S}_t$ that is evaluated, and even more on the wavelength used. For each λ_{ex}, the accuracy of the size evaluation was better in the region where the graph was fairly well be approximated by a linear fit function. This region changes for different excitation wavelengths. Using smaller wavelengths and the non linear calibration mode, "true" object diameter as low as 20 nm were detected with an error (standard deviation) of a few nanometer. Using a linear approximation calibration mode, "true" object extension down to 40-50 nm were correctly detected by the SMI-evaluation procedure (compare Figure 3.16). Using longer wavelengths, "true" diameters up to about 180 nm were correctly determined.

Figure 3.17 shows the relationship obtained between "true" size $\mathcal{S}_t$ and detected size $\mathcal{S}$ as the result of the calculation procedure. The most simple correlation between "true" size and "evaluated" size is given by the continuous straight line, using the linear approximation mode. The vertical bars indicate the standard deviation obtained under the assumption of a Poisson noise corresponding to a total number N_{tot} = 9,600 of fluorescent photons detected for each object in each channel. For each wavelength, the range where the linear approximation can be used successfully is given by the region with small size error bars.

Table 3.2 shows the results for the second condition: $\lambda_{em} = \lambda_{ex} + 100$ nm. A comparison of the results of Table 3.2 with those of Table 3.1 shows that similar results are obtained for both cases a) $\lambda_{ex} = \lambda_{em}$; b) $\lambda_{em} = \lambda_{ex} + 100$ nm. This indicates that the size evaluation does not critically depend on the small enlargement of the $FWHM_{SMI}$ of the enveloping curve (corresponding to the detection PSF) of the SMI-PSF produced by reasonable small Stokes shifts of the fluorescent emission. Under both conditions, however, a strong dependence in size determination on the excitation wavelength λ_{ex} was noted. This last consideration suggests a imaginary picture to describe a SMI microscope: Such a microscope could be imagined as a linear ruler in which the SMI interference fringes are the marks. Varying λ_{ex}, the fringe widths $FWHM_f$ are modified and by that the width of the marks. Reducing the width of the marks, it become more easy to measure small object sizes.

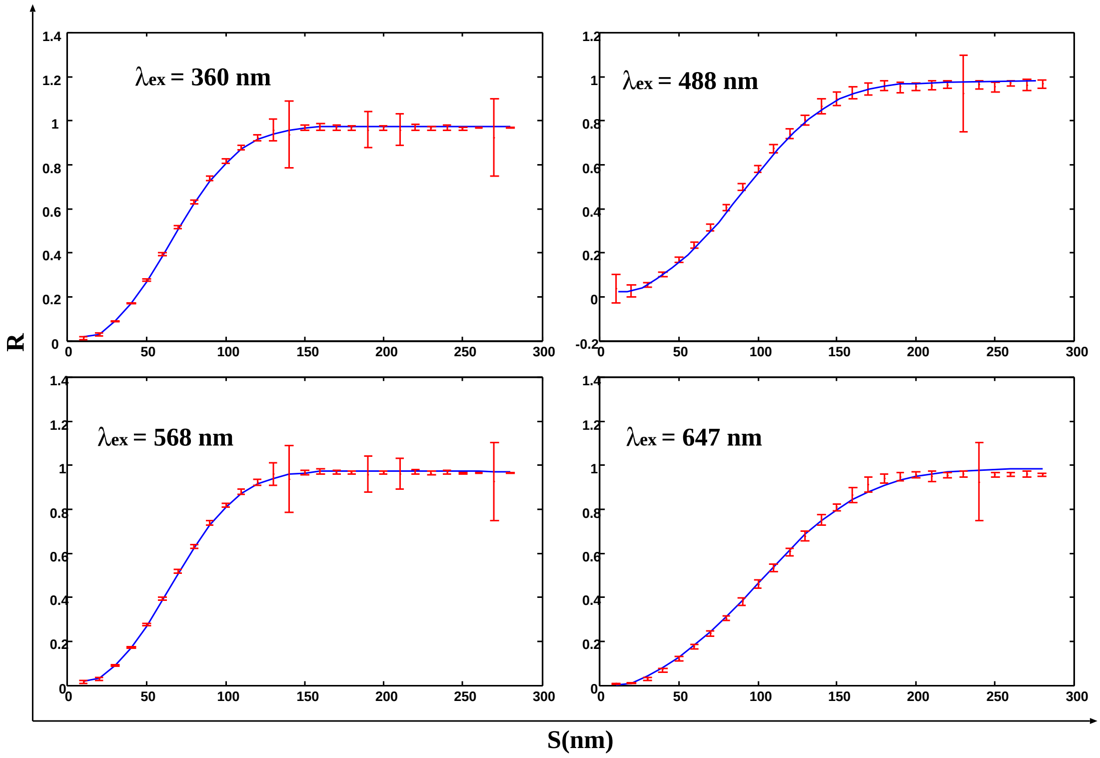

Figure 3.15: Case: $\lambda_{ex} = \lambda_{em}$.
The curves plotted with bars were evaluated assuming that the total number of photons (N_{tot}) registered was N_{tot} = 9,600 and that photon noise was added to the AIDs. Abscissa: Object diameter size $\mathcal{S}$ (nm). Ordinate: Modulation contrast R.
The continuous lines are the calibration functions under "ideal" noiseless conditions evaluated by VIM.

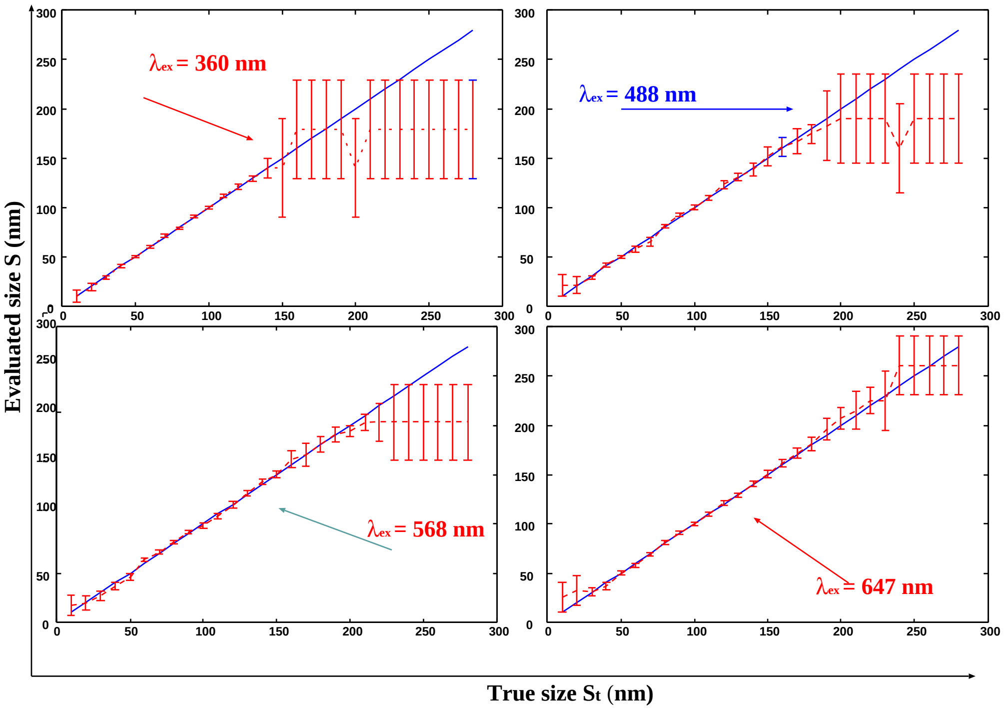

Figure 3.16: Simulation for the case case: $\lambda_{ex} = \lambda_{em}$.
Abscissa: "True size" $\mathcal{S}_t$(nm) $= FWHM_{True}$.
Ordinate: Detected size $\mathcal{S}$(nm).
The objects size values $\mathcal{S}$ are evaluated using the graphical VIM calibration representation of the modulation contrast R shown in Figure 5, 6. Continuous lines: "True size" S_t(nm) $= FWHM_{True}$, dotted lines and bars: detected sizes and their standard deviations, respectively.

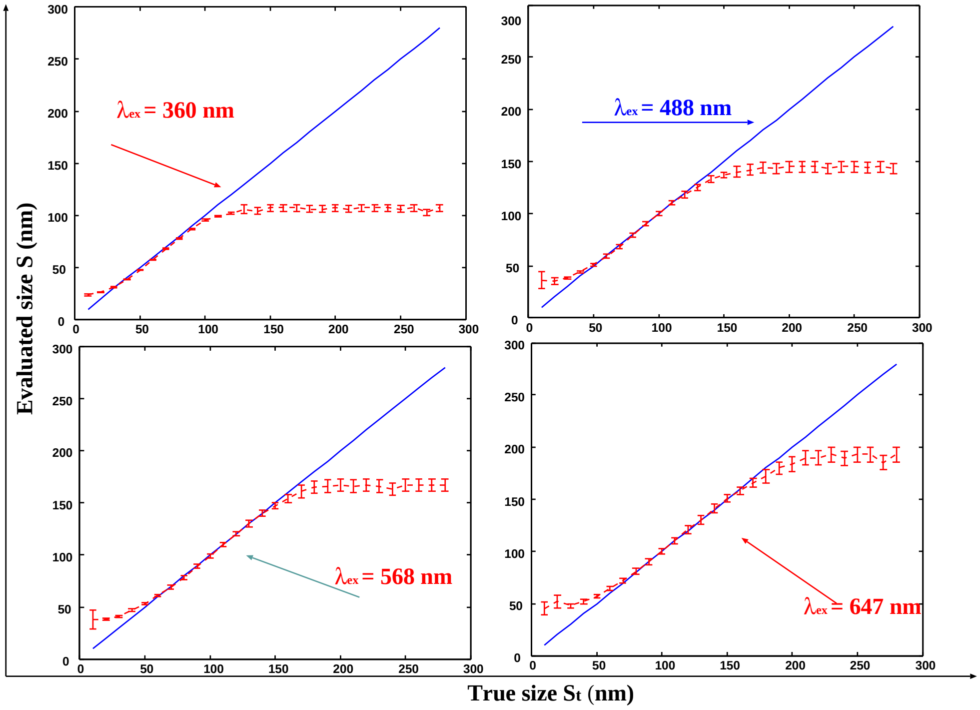

Figure 3.17: Case: $\lambda_{ex} = \lambda_{em}$.
Abscissa: "True size" $\mathcal{S}_t$(nm) $= FWHM_{True}$.
Ordinate: Detected size $\mathcal{S}$(nm)
. The objects size values (equal to the diameter in the case of spherical objects) are evaluated using the linear expression of the modulation contrast R. Continuous lines; "True size" $S_t = FWHM_{True}$; dotted lines and bars: detected sizes and their standard deviations, respectively.

Table 3.1: Case: $\lambda_{ex} = \lambda_{em}$.
Three different VIM approaches in order to determine the object size starting from the evaluation of the modulation contrast R are used. The evaluations are performed for the effective excitation wavelengths, indicated in the head row of the Table.
Column A: "True size" values ($\mathcal{S}_t$); i.e. the $FWHM_{True}$ of the objects fixed at the start of the VIM simulation process.
Columns B: Determination of the object size ($\mathcal{S}$) using the graphical visualization of the modulation contrast R; for more details see Figure 5, 6 and the main text.
Columns C: Determination of the object size ($\mathcal{S}_L$) after inversion of the linear approximation of the calibration function (for more details see the main text).

$\mathcal{S}_t$ (nm)	$\mathcal{S}$ (nm) λ_{ex} = 360 nm	$\mathcal{S}_L$ (nm) λ_{ex} = 360 nm	$\mathcal{S}$ (nm) λ_{ex} = 488 nm	$\mathcal{S}_L$ (nm) λ_{ex} = 488 nm	$\mathcal{S}$ (nm) λ_{ex} = 568 nm	$\mathcal{S}_L$ (nm) λ_{ex} = 568 nm	$\mathcal{S}$ (nm) λ_{ex} = 647 nm	$\mathcal{S}_L$(nm) λ_{ex} = 647 nm
10	9.8 ± 6.0	24 ± 1	21 ± 11	36 ± 8	17 ± 10	38 ± 9	25 ± 15	45 ± 6
20	19.2 ± 3.8	26.1 ± 0.5	21.0 ± 8.7	35 ± 3	19.2 ± 6.7	38 ± 1	32 ± 15	52 ± 6
30	28.8 ± 1.9	31.1 ± 0.5	28.8 ± 1.9	38 ± 1	26.8 ± 4.6	41 ± 1	30.7 ± 4.8	48 ± 2
40	40.3 ± 1.3	38.2 ± 0.2	41.3 ± 1.5	44 ± 1	36.5 ± 3.8	47 ± 1	36.5± 3.8	52 ± 2
50	50.0 ± 1.3	47.4 ± 0.4	50.0 ± 1.4	51 ± 1	46.1 ± 3.8	53 ± 1	50.0 ± 1.9	57 ± 2
60	59.8 ± 1.3	57.4 ± 0.5	57.7 ± 2.8	59 ± 2	63.4 ± 1.9	61 ± 1	57.7 ± 1.9	64 ± 2
70	71.1 ± 1.3	68.0 ± 0.6	65.4 ± 4.6	68 ± 2	71.1 ± 1.9	69 ± 2	69.2 ± 1.9	72 ± 2
80	78.8 ± 1.3	77.8 ± 0.7	80.8 ± 2.0	79 ± 2	81.3 ± 1.9	78 ± 2	80.8 ± 1.9	81 ± 3
90	90.3 ± 1.3	87.0 ± 0.7	92.3 ± 2.0	90 ± 2	91.2 ± 1.9	89 ± 2	90.3 ± 1.9	90 ± 3
100	100.0 ± 1.5	95.4 ± 0.8	100.0 ± 2.4	100 ± 2	98.1 ± 3.0	99 ± 2	100.0 ± 1.9	100 ± 3
110	111.5 ± 1.9	99.3 ± 0.9	109.6 ± 2.4	110 ± 2	107.7 ± 3.0	110 ± 2	109.6 ± 1.9	110 ± 3
120	121.0 ± 2.3	102 ± 1	123.1 ± 3.8	118 ± 3	119.2 ± 3.0	120 ± 2	121.1 ± 1.9	121 ± 4
130	128.8 ± 3.0	106 ± 4	130.8 ± 3.8	125 ± 3	130.7 ± 3.0	130 ± 3	128.8 ± 1.9	130 ± 4
140	140 ± 10	104 ± 3	138.4 ± 6.7	133 ± 3	142.2 ± 3.0	140 ± 3	140.3 ± 2.8	141 ± 4
150	140 ± 50	107 ± 3	151.9 ± 9.6	137 ± 3	150.0 ± 3.0	147 ± 3	150.3 ± 3.8	151 ± 4
160	179 ± 50	107 ± 3	161.5 ± 9.6	140 ± 5	165.3 ± 8.6	154 ± 4	161.5 ± 3.8	158 ± 4
170	179 ± 50	107 ± 3	167 ± 13	142 ± 5	170 ± 12	161 ± 6	171.7 ± 5.1	166 ± 4
180	179 ± 50	106 ± 3	175.0 ± 9.6	144 ± 5	180.6 ± 7.7	165 ± 6	180.8 ± 6.7	172 ± 6
190	179 ± 50	106 ± 3	183 ± 35	143 ± 5	190.7 ± 7.7	166 ± 6	196 ± 11	180 ± 6
200	140 ± 50	107 ± 3	190 ± 45	145 ± 5	194.2 ± 5.7	167 ± 6	207 ± 11	184 ± 7
210	179 ± 50	106 ± 3	190 ± 45	145 ± 5	202.8 ± 8.3	166 ± 6	215 ± 19	190 ± 7
220	179 ± 50	107 ± 3	190± 45	145 ± 5	203 ± 19	167 ± 6	225 ± 13	190 ± 7
230	179 ± 50	107 ± 3	190 ± 45	143 ± 5	203 ± 38	166 ± 6	225 ± 30	193 ± 7
240	179 ± 50	107 ± 3	160 ± 45	145 ± 5	203 ± 38	163 ± 6	261 ± 30	189 ± 7
250	179 ± 50	106 ± 3	190 ± 45	145 ± 5	203 ± 38	167 ± 6	261 ±30	193 ± 7
260	179 ± 50	107 ± 3	190 ± 45	144 ± 5	203 ± 38	167 ± 6	261 ± 30	193 ± 7
270	179 ± 50	103 ± 3	190 ± 45	145 ± 5	203 ± 38	167 ± 6	261 ± 30	185 ± 7
280	179 ± 50	107 ± 3	190 ± 45	143 ± 5	203 ± 38	167 ± 6	261 ± 30	193 ± 7
290	179 ± 50	106 ± 3	190 ± 45	146 ± 5	203 ± 38	161 ± 6	261 ± 30	193 ± 7
A	B	C	B	C	B	C	B	C

Table 3.2: Case: $\lambda_{em} = \lambda_{ex} + 100$ nm.
Two different VIM approaches in order to determine the object size starting from the evaluation of the modulation contrast R are used. The evaluations are performed for the effective excitation wavelengths, indicated in the head row of the Table. Column A: "True size" values ($\mathcal{S}_t$); i.e. the $FWHM_{True}$ of the objects fixed at the start of the VIM simulation process.
Columns B: Determination of the object size ($\mathcal{S}$) using the graphical visualization of the modulation contrast R; for more details see the main text.
Columns C: Determination of the object size ($\mathcal{S}_L$) after inversion of the linear approximation of the calibration function (for more details the main text).

$\mathcal{S}_t$ (nm)	$\mathcal{S}$ (nm) λ_{ex} = 360 nm	$\mathcal{S}_L$ (nm) λ_{ex} = 360 nm	$\mathcal{S}$ (nm) λ_{ex} = 488 nm	$\mathcal{S}_L$ (nm) λ_{ex} = 488 nm	$\mathcal{S}$ (nm) λ_{ex} = 568 nm	$\mathcal{S}_L$ (nm) λ_{ex} = 568 nm	$\mathcal{S}$ (nm) λ_{ex} = 647 nm	$\mathcal{S}_L$ (nm) λ_{ex} = 647 nm
10	9.6 ± 6.0	20 ± 1	19 ± 10	13 ± 8	17 ± 10	31 ± 9	25 ± 15	39 ± 6
20	12.3 ± 3.8	19.4 ± 0.3	19.2 ± 3.7	25 ± 3	17.3 ± 8.1	29 ± 1	32 ± 15	36 ± 6
30	30.7 ± 1.9	34.1 ± 0.3	28.8 ± 1.9	40 ± 1	30.8 ± 5.4	46 ± 1	28.8 ± 5.8	52 ± 2
40	44.2 ± 1.3	49.4 ± 0.3	41.3 ± 1.5	45 ± 1	38.5 ± 3.8	54 ± 1	36.5 ± 5.8	63 ± 2
50	51.9 ± 1.3	49.6 ± 0.4	50.0 ± 1.4	52 ± 1	48.5 ± 3.8	55 ± 1	48.5 ± 1.9	59 ± 2
60	61.5 ± 1.3	59.3 ± 0.5	57.7 ± 2.8	60 ± 2	63.4 ± 1.9	62 ± 1	57.7 ± 1.9	61 ± 2
70	69.2 ± 1.3	69.3 ± 0.6	67.4 ± 4.6	70 ± 2	71.1 ± 1.9	70 ± 2	69.2 ± 1.9	72 ± 2
80	80.7 ± 1.3	79.3 ± 0.6	80.7 ± 2.0	80 ± 2	81.3 ± 1.9	79 ± 2	80.8 ± 1.9	82 ± 3
90	90.3 ± 1.3	87.6 ± 0.9	92.3 ± 2.0	90 ± 2	91.2 ± 1.9	89 ± 2	90.3 ± 1.9	90 ± 3
100	100.0 ± 1.5	94.9 ± 0.7	100.0 ± 2.4	100 ± 2	98.1 ± 3.0	99 ± 2	100.0 ± 1.9	100 ± 3
110	113.5 ± 1.9	100.4 ± 0.9	109.6 ± 2.4	110 ± 2	107.7 ± 3.0	110 ± 2	111.5 ± 1.9	111 ± 3
120	121.0 ± 2.3	104 ± 1	121.1 ± 3.8	119 ± 3	117.3 ± 3.0	121 ± 2	119.2 ± 1.9	121 ± 4
130	128.8 ± 3.0	107 ± 4	130.8 ± 3.8	126 ± 3	128.8 ± 3.0	130 ± 3	128.8 ± 1.9	130 ± 4
140	140 ± 10	107 ± 3	138.4 ± 6.7	132 ± 3	140.3 ± 3.0	139 ± 3	138.5 ± 2.8	141 ± 4
150	140 ± 50	107 ± 3	150.0 ± 9.6	135 ± 3	151.9 ± 3.0	146 ± 3	148.1 ± 3.8	150 ± 4
160	179 ± 50	106 ± 3	154.4 ± 9.6	139 ± 5	165.3 ± 8.6	154 ± 4	161.5 ± 3.8	157 ± 4
170	179 ± 50	105 ± 3	167 ± 13	141 ± 5	170 ± 12	161 ± 6	171.7 ± 5.1	164 ± 4
180	179 ± 50	105 ± 3	171 ± 10	142 ± 5	180.6 ± 7.7	165 ± 6	180.8 ± 6.7	172 ± 6
190	179 ± 50	105 ± 3	183 ± 35	143 ± 5	190.7 ± 7.7	167 ± 6	194 ± 11	178 ± 6
200	140 ± 50	108 ± 3	190 ± 45	145 ± 5	194.2 ± 5.7	168 ± 6	211 ± 11	185 ± 7
210	179 ± 50	107 ± 3	190 ± 45	145 ± 5	202.8 ± 8.3	169 ± 6	215 ± 19	190 ± 7
220	179 ± 50	107 ± 3	190 ± 45	145 ± 5	203 ± 19	169 ± 6	225 ± 13	187 ± 7
230	179 ± 50	107 ± 3	190 ± 45	143 ± 5	203 ± 38	169 ± 6	225 ± 30	189 ± 7
240	179 ± 50	107 ± 3	160 ± 45	145 ± 5	203 ± 38	170 ± 6	261 ± 30	189 ± 7
250	179 ± 50	107 ± 3	190 ± 45	145 ± 5	203 ± 38	169 ± 6	261 ±30	192 ± 7
260	179 ± 50	107 ± 3	190 ± 45	144 ± 5	203 ± 38	167 ± 6	261 ± 30	193 ± 7
270	179 ± 50	109 ± 3	190 ± 45	147 ± 5	203 ± 38	170 ± 6	261 ± 30	195 ± 7
280	179 ± 50	107 ± 3	190 ± 45	143 ± 5	203 ± 38	169 ± 6	261 ± 30	193 ± 7
290	179 ± 50	108 ± 3	190 ± 45	146 ± 5	203 ± 38	169 ± 6	261 ± 30	193 ± 7
A	B	C	B	C	B	C	B	C

Chapter 4

Experimental object size evaluations

Spectral Precision Distance Microscopy (SPDM)[23,41,42] in combination with conventional microscopic techniques, or with Standing Wave Illumination/SMI[24,17,20,25] microscopy and several others PSF engineering methods[7,8,12,18,19] allows to obtain high accuracy nanolocalization and subwavelength mutual distance resolution of small targets labeled with different spectral signatures. Spectral signature (specs) is any fluorescent labeling scheme allowing by photophysical means to discriminate the photons emitted from an object labeled with the respective specs. Another not less important topic is the determination of the size of individual nanostructures using FFLM. Such "nanosizing", e.g. of individual fluorescent objects with a diameter between 50 and 100 nm, can be performed by FFLM in different ways: One may use PSF-engineered microscope devices with an appropriately small FWHM of the PSF (e.g. 100 nm) if necessary in combination with deconvolution techniques; another approach is to use SPDM of the object following multispectral labeling. In this case, the size of the object is given by the topology of its labeled sites. E.g., the diameter of an object may be determined by a sufficient number of multispectrally labeled sites on its surface.

Here, an alternative to SPDM nanosizing is presented using SMI microscopy. For size determination, it requires labeling with one spectral signature ("monospectral labeling") only; any of the known fluorescence labeling techniques may be used; one photon excitation is sufficient; conventional object slides may be used; finally, the percentage of fluorescence photons contributing to the information is as high as in epifluorescence microscopy, allowing the nanosizing also of weakly fluorescent objects. Based on previous theoretical considerations , in this report, experimental results of nanosize measurements using this new far field light microscopy approach are presented. In combination with SMI-VIM evaluation tools ,this new method allowed to obtain experimental information about the size of individual fluorescent labeled objects with a diameter (size) ranging from about 25 nm to 140 nm with high accuracy.

In this Chapter the results of size measurements performed on different kind of fluorescent particles (e.g. beads with different nominal size) will be presented.

The results prove that using SMI-microscopy in combination with SMI-VIM calibration, subwavelength object size measurements down to 40 nm (for $\lambda_{ex} = 647$ nm) and 25 nm (for $\lambda_{ex} = 488$ nm) are experimentally feasible with high accuracy.

4.1 Experimental details

4.1.1 Specimen

The specimens used were different kind of fluorescents beads. In detail, beads with a diameter of 40 nm and 100 nm excitable at 647 nm excitation weavelength ("red beads") and beads with a diameter of 40 nm and 100 nm excitable at 488 nm excitation wavelength ("green beads") were provided by Molecular Probes (Eugene, Oregon); "green beads" with a nominal diameter of 50 and 100 nm were provided by Biolab SN; "green beads" with a diameter of 26 nm, 44 nm, 57 nm, 71 nm, 85 nm 100 nm and 140 nm were provided by Duke Lab. The diameters mentioned were provided by the manufacturers.

4.1.2 The SMI-microscope setup

The SMI-microscope used has been described in detail in several publications[1,2,3,4,5,6,7,8,9,10,11,12] and its description will be not the main topic of this dissertation. Briefly, it can be represented as an interferometer setup where two collimated and counterpropagating laser beams with linear polarization are focused into the back focal plane of two opposite objective lenses (for more details see Figure 4.1). This configuration leads to an interference pattern, i.e. a "standing wavefield" with plane wavefronts characterised by a $\cos^2$-shape of the intensity along the axial direction. For excitation, both an Ar^{+}-laser ($\lambda_{ex} = 488$ nm, "green light") and a Kr^{+}-laser ($\lambda_{ex} = 647$ nm, "red light") were used. The emitted fluorescence light was detected by a CCD camera after the light had been separated from the coherent excitation light by a dichroic beamsplitter (for more details see Figure 4.1). For the measurements, the objects were moved along the axial direction using a piezoelectric stage; the step size was 20 nm. During this procedure, images were acquired at equidistant axial positions (optical sectioning).

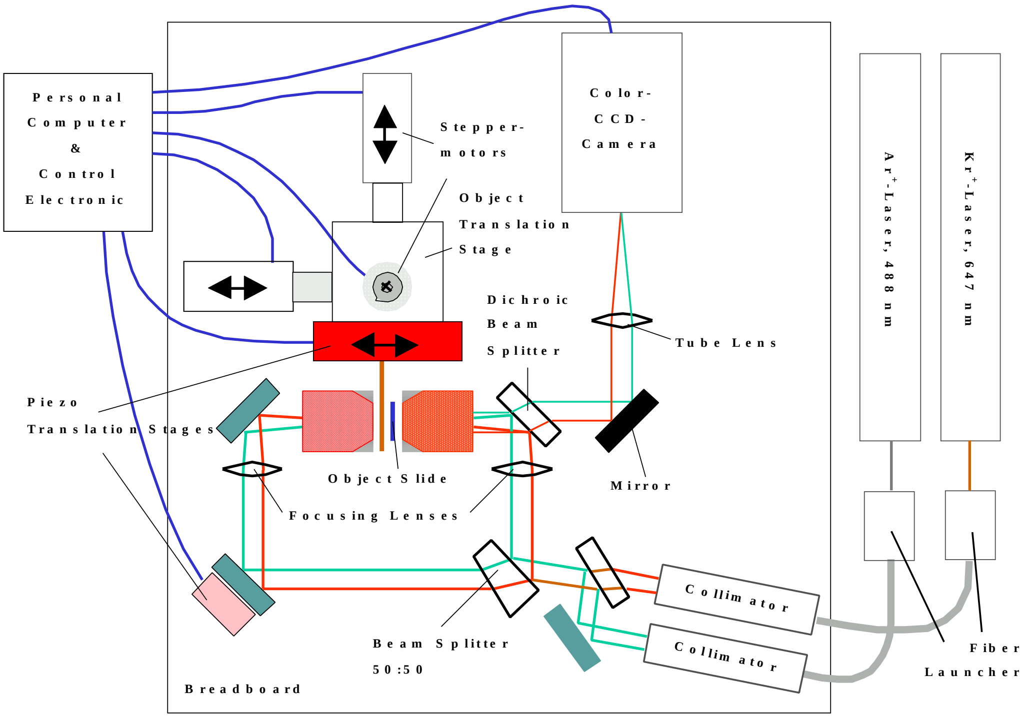

Figure 4.1: SMI microscope set-up: Briefly, it consists of a rectangular interferometer with a 50 : 50 beam splitter. Two vertically polarised beams are focused into the back focal plane of a corresponding objective lens. Between the two objective lenses, a "standing wave field" is produced. The objects mounted on a conventional cover slide, and covered by a conventional cover slip can be moved along the axial direction as the object translation stage is moved by stepper motors. For the detection, a cooled colour CCD camera is used.

4.1.3 Principles of the size evaluation method

For the evaluation of the axial diameter of fluorescent particles , it is necessary to recall some fundamental concepts of SMI microscopy: The Point Spread Function (PSF) is the intensity distribution of a "point-like" object, and its axial projection ($PSF(z)$) can be represented as the product between a sinc-squared function (the epifluorescent PSF) and a cosine-squared function (excitation PSF) (see equation 1.2).

The Axial Intensity Distribution (AID) of an extended, i.e. not point like, fluorescent object differs from the PSF. In this case, the AID of an extended fluorescent object presents an internal unmodulated part (object "disturbance"); the larger the object the larger the object "disturbance". The AID may be approximated by the adaptation function here called ($AID(z)$) described in equation 2.3. In the present section a more complex expression of $AID(z)$ (in which the background noise is considered) is used:

$$AID(z) = \left[M_1 \mathrm{sinc}\left(\frac{z-z_1}{B}\right)\right]^2 \left[\cos\frac{z-z_0}{C}\right]^2 + \left[M_g \mathrm{sinc}\left(\frac{z-z_2}{E}\right)\right]^2 + L; \tag{4.1}$$

where all the parameters of the first element of the sum are the same as defined in equation 2.3; M_g, E are positive parameters, and z_2 is the position of the maximum of the object "disturbance" (for more details see Figure 2.1. The positive parameter L corresponds to the mean background noise. Two different approaches were made to evaluate the AID of a fluorescent object: Using an automatic routine the mean background noise was subtracted from the 3D image before extracting the AID; consequently, the parameter L was fixed to be equal to zero in equation 4.1. In the second case, no background subtraction was made before extracting the AID, and the adaptation function $AID(z)$ described in equation 4.1 was considered to be the approximation of the AID.

4.1.4 Size evaluation algorithms

The concept of the nanosize measurements is based on the well known fact that the object "disturbance" increases increasing the object size. In the terms of equation 4.1, this object "disturbance" was quantified by the parameter M_g. By using SMI-VIM (for more details see Chapter 2) it is possible to determine the axial extension ("size") of small fluorescent objects (corresponding to the diameter in case of spherical object). The algorithms for this have been described in detail in Chapter 2. Briefly, the object size in the direction of the optical axis (axial direction (z)) is determined when the evaluation of the ratio R ("modulation contrast" R) between the object "disturbance" and the total AID maximum is made (see Figure 4.2). Taking into account equation 4.1, the relation between the modulation contrast R and the parameter introduced in equation 4.1 may be written as in equations 2.3 and 2.3:

$$R := \frac{M_g}{M} = \frac{M_g}{M_1 + M_g} = \frac{1}{1 + \frac{M_1}{M_g}}; \tag{4.2}$$

with $M := M_1 + M_g$.

The VIM calibration functions (see Section 2.3) and the analytical expression of R (see Section 2.3.2) were used in order to determine the object size. It is important to remind that to obtain these calibration functions, only microscope parameters (excitation/emission wavelengths, numerical aperture, refraction index of the embedding medium) were used while all experimental object information was excluded.

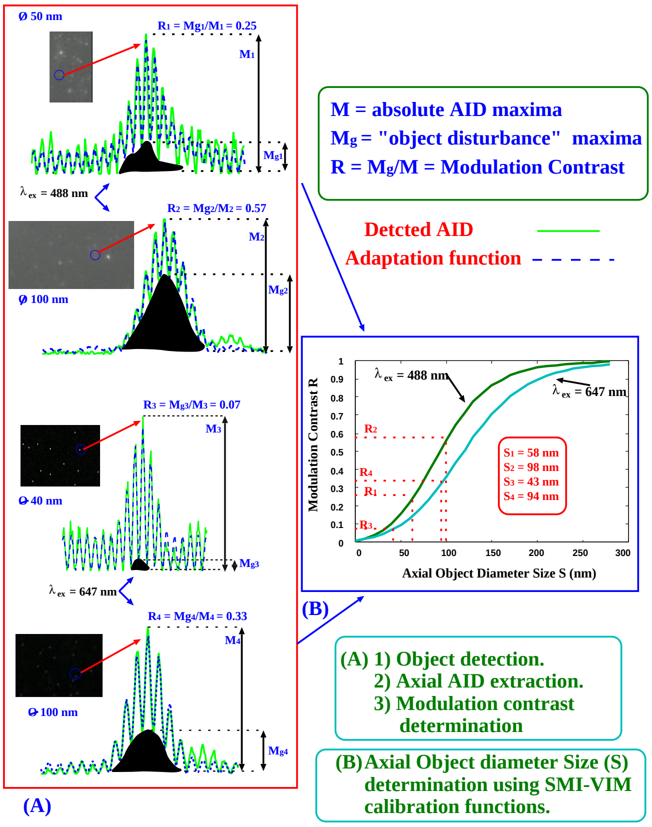

Figure 4.2: Principle of SMI-nanosizing: A) Experimental examples for SMI x,y viewing fields with beads visible as very small white "dots" are presented at the left; the AIDs shown at the right indicate the intensity distribution for the objects encircled. Note that the intensity minima in the zone beneath the AID-maximum are modulated due to the object "disturbance". For better clarity, this zone is indicated manually (in black). Virtual Microscopy (VIM) calibration allowed to extract the parameters of the axial AID and to measure the modulation contrast R (see equation 4.2). In the Figure, the adaptation function, used for the determination of R is represented by a dotted line. The experimental AIDs and the results of the modulation contrast R determination using the VIM tools, (from top to bottom) of a 50 nm ∅ "green bead"; of a 100 ∅ "green bead"; of a 40 nm ∅ "red bead"; and of a 100 nm ∅ "red bead", respectively, are shown. B) Using SMI-VIM calibration functions $R = f(S)$, it was possible to determine the size S of the fluorescent objects with the AIDs indicated on the left side.

4.2 A first series of size measurements.

A first series of experiments were realised using different kinds of "beads". Measurements were performed with 40 nm ∅ (diameter) and 100 nm ∅ beads ("nominal diameter" according to the manufacturer), excited by 647 nm wavelength ("red beads"); in addition, 50 nm ∅ and 100 nm ∅ beads excited by 488 nm wavelength "green beads" were measured. Part of these of experiments was made using the 40 nm ∅, 100 nm ∅ "red beads" and the 100 nm ∅ ("green beads") characterised by a nominal diameter size of 40 nm and 100 nm, respectively. The beads were deposited on a conventional object slide and embedded using Vectashield (Vector Laboratories, Burlingame, California) and their density was adjusted by epifluorescence microscopy in such a way that individual, very small diffraction limited "spots" were observed. Such "spots" were assumed to be candidates for individual isolated "beads"; for the SMI measurements, the conventional object slide was covered by a conventional cover slip. The object slides prepared as described above were placed between the two SMI microscope objective lenses; immersion oil (index of refraction n =1.515) was used to provide optical contact between the external surface of the cover slip and of the object slide and the front surface of the SMI-objective lenses (NA = 1.4; magnification 100x). Scanning the object slide with the SMI microscope, a total number of $N_{totb} = N_{40r} = 13$ (40 nm ∅ "red beads"); $N_{totb} = N_{100r} = 15$ (100 nm ∅ "red beads"); and $N_{totb} = N_{100g} = 7$ (100 nm ∅ "green beads") beads were localised. For each of these specimens, 10 independent consecutive measurements were made. For a given object slide with beads, a full set of optical sectioning (200 optical sections) was performed providing a first 3D-data stack; after completion, this procedure was carried out another 9 times; each of these measurements consisted of the acquisition of 200 bidimensional (lateral x-y-plane) images which were orthogonal to the axial (z) direction defined by the optical axis of the two SMI objective lenses, and placed along different z positions. By the object scanning stage the axial distance (Δz) between two neighboring image planes was fixed to be 20 nm; the 3D images acquired were characterized by a voxel size of $(107\times107\times20)$ nm^3. For size determination, two different approaches were used as described in section 4.1: In the first, the mean background noise from the 3D data stack was deduced before extraction of the AID; in the second case, the AID parameters were determined without prior background noise subtraction. From the adaptation function (equation 4.1), the parameters M_1 and $M_g$were used to calculate the modulation contrast R (see equation 2.3). This experimentally determined modulation contrast R was then inserted into the calibration function $R = f(S)$ obtained by SMI-VIM computer simulations, using the excitation/emission wavelengths, the refractive index of the immersion oil, and the numerical aperture applied as the only additional parameters. For all

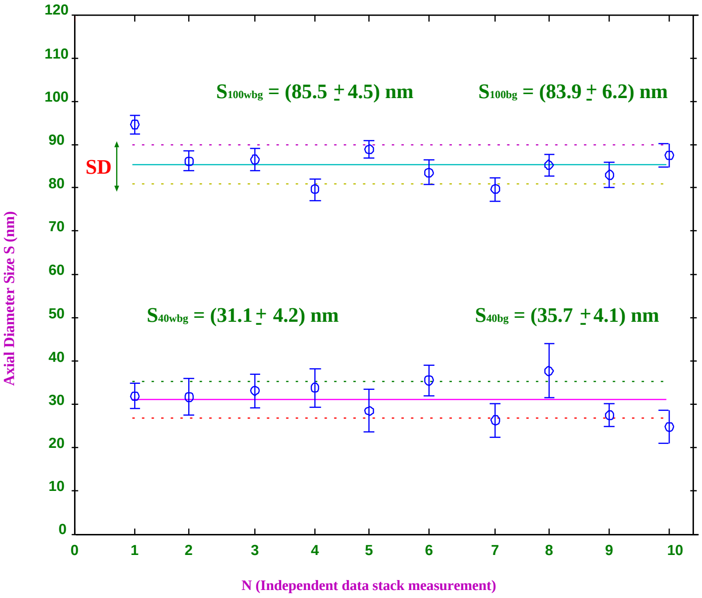

Figure 4.3: Experimental SMI nanosizing of 40 nm ∅ and 100 nm ∅ "red beads": The results of ten independent size (i.e. 10 independent 3D-data stacks) measurements are shown for the case of specimens consisting of 40 nm ∅, and of 100 nm ∅ "red beads", respectively. In the graph, the continuous lines are the mean values of all the 10 independent data stacks (S_{wbg} values); the dotted lines indicate the mean values plus and minus their standard deviations (SD). The circles are the mean values evaluated for each singular acquisition, and the bars are their standard deviations of the mean (SDM). In the graph, the final results of the size estimates obtained subtracting the background noise before the AID computation (S_{40wgb}, S_{100wgb}), and without any prior background noise substraction before the AID evaluation (S_{40gb}, S_{100gb}) are given also numerically.

the single 3D data stacks, the means of S for all the N_{40r} (or N_{100r}, N_{100g}) beads were evaluated and considered as the estimate of the size (diameter) of the beads; the standard deviation of the mean was considered as the estimate of the accuracy (for more details see Figure 4.3, Figure 4.4 and Tables 4.2, 4.3). The mean values calculated for all the size evaluations in the ten independent 3D-data stacks were considered as the estimate of the mean diameter/size S of the bead ensemble (for more details see Figures 4.3, 4.4, 4.5 and Table 4.1). In Table 4.1, the results of size measurements are shown, as obtained after the two different methods for

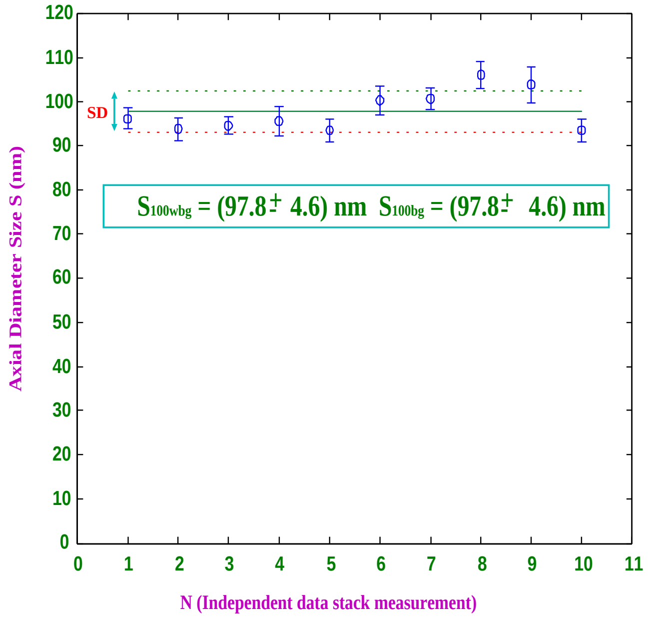

Figure 4.4: Experimental SMI nanosizing of 100 nm ∅ ”green beads”: The results of ten independent measurements (ten 3D-data stacks) for the case of a specimen consisting of 100 nm ∅ ”green beads”. In the graph, the continuous line represents the mean values for all the 10 independent data stacks (S_{wbg} values); the dotted lines indicate the mean values plus and minus their standard deviations (SD). The circles indicate the mean values evaluated for each singular acquisition, and the bars are their standard deviations of the mean (SDM). The final results of the size estimates obtained subtracting the background noise before the AID computation (S_{100wgb}), and without any prior background noise substraction before the AID evaluation (S_{100gb}), are given also numerically.

extraction of the AID were used. In the column at the left margin the nominal diameter values (”true size” $\mathcal{S}$) of the spherical beads are placed as given by the manufacturer; in the other two columns, the results of the evaluation are shown performed a) after a background noise substraction was automatically made on the 3D data stacks ($\mathcal{S}_{wbg}$ ”S with background noise subtraction”); b) for the case that no background noise substraction was made ($\mathcal{S}_{bg}$ ”S with remaining background noise”). The results of the two different methods of data treatment were in good agreement: The measurements regarding the same beads ensemble did not differ by more than the estimate of the standard deviation. Furthermore, the results shown were found to be close to the nominal values given by the manufacturer. Differences between the measured values and the nominal values of the beads were found especially when 100 nm ∅ ”red beads” measurements were analyzed. These different values may be explained by the consideration that the SMI size evaluation regards the effective fluorescent size of the beads but not the total physical size. The two sizes coincide only in the ideal case of complete spatial homogeneity; for example, in the case that the fluorescence molecules are concentrated in the interior core of the beads, the diameter obtained by SMI-nanosizing would be smaller than the diameter determined by EM or atom force microscopy. Unfortunately, no detailed information about the spatial homogeneity of the fluorochrome distribution was avaliable from the manufacturer. Even more, the manufacturer did not deliver any information regarding the accuracy of his size evaluation, neither any information regarding the methods used for such evaluations. Consequently, it is presently not possible to decide to what extent the small deviations between the measured object size and the nominal object size are due to measurements and calibration artefacts. In any case, the accuracy of the measurements was high in the case that 100 nm ∅ ”green beads”, 100 nm ∅ ”red beads”, 40 nm ∅ ”red beads” and 50 nm ∅ ”green beads” were considered. An accuracy of $\simeq$ 10-20% for 40 nm ∅ ”red beads”, and $\simeq$ 5-10% for 50 nm ∅ ”green beads”, 100 nm ∅ ”green beads”, and 100 nm ∅ ”red beads” was found. These determinations are consistent with the theoretical predictions (for more details see Chapter 2 and Chapter 3). The experiments made with 50 nm ∅ ”green beads” deserve a special remark: These beads exhibited a high fluorescence bleaching rate; thus, it was not possible to repeat 10 times the SMI measurements on the same ensemble of beads as in the other cases. Instead, the mean values of the sizes of four different ensembles having 20, 22, 27, and 24 beads, respectively, were evaluated (for more details see Tables 4.1, 4.4, and Figure 4.5). The size estimates presented in Table 4.1 are the mean values of all the size measurements in all the four independent ensembles. For the cases of 40 nm ∅ ”red beads” and 100 nm ∅ ”green beads”, it was possible to study the accuracy of size measurements regarding not the ensemble but each single identified bead. The mean of ten independent measurements was considered as the estimate of the size of each single identified bead, and the accuracy was estimated using the evaluated values of the standard deviation on the acquisitions. In Table 4.5 , evaluations of the size of each bead for the case of 40 nm ∅ ”red beads” ($\mathcal{S}_{40r}$), 100 nm ∅ ”red beads”($\mathcal{S}_{100g}$), and 100 nm ∅ ”green beads” ($\mathcal{S}_{100g}$) are presented. In this case, a comparison between the two different data analysis methods is presented. The results shown in columns A were obtained after the mean background noise was automatically subtracted in each 3D data stack; instead, the results shown in columns B were calculated without any previous background noise substraction. The two different data analysis methods

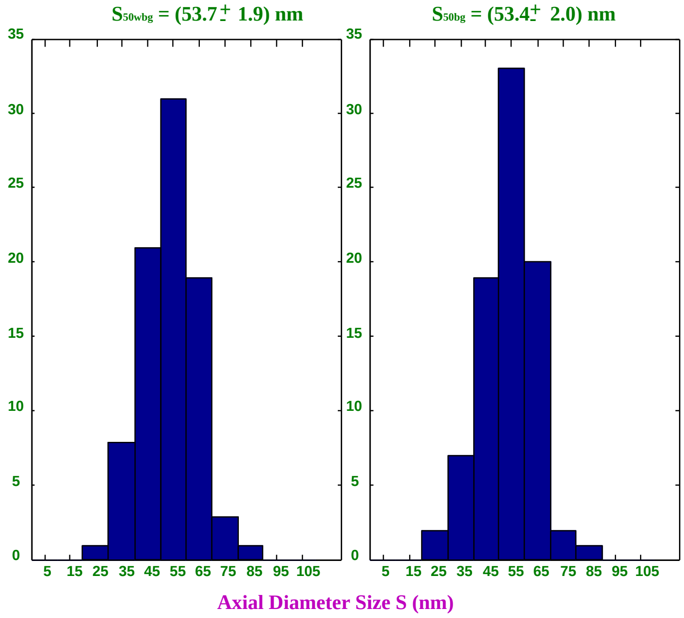

Figure 4.5: Experimental SMI nanosizing of 50 nm ∅ ”green beads”: The results of four independent measurements for the case of specimen consisting of 50 nm ∅ ”green beads”. The histograms presented were obtained merging all the size measurements made on four independent specimens ($N_{totb} = 93$). The histogram on the left side is related to the case in which the background noise was subtracted from the 3D data set before the AID computation; the histogram on the right side presents the results of measurements performed without any prior background substraction noise. $S_{50_{wbg}}$, $S_{50_{bg}}$ are the mean values measured merging the size measurements of all the four specimens. Due to the histogram step size of 10 nm, the apparent histogram width is broadened compared to the standard deviation calculated from the individual data.

yielded compatible results. As predicted by SMI-VIM (for more details see Chapter 2 and Chapter 3), in general the accuracy in size determination was higher for the case of 100 nm ∅ ”green beads” and ”red beads” than for the case of 40 nm ∅ ”red beads”. It is important to note that in the case of 100 nm ∅ ”green beads” and 100 nm ∅ ”red beads”, an accuracy in the order of 5% was often obtained corresponding to about 1/100 of the excitation wavelength.

Table 4.1: Summary of nanosizing results: Here the results of size measurements performed on 40 nm ∅ ”red beads”, 50 nm ∅ ”green beads”, 100 nm ∅ ”red beads” and ”green beads” are shown (mean ± standard deviation (SD)). In the column on the left side the nominal values of the beads size given by the manufacturer are listed. In the second column from the left the results of size measurements, in the case the background noise is automatically subtracted from the 3D data before the AID computation, are presented ($\mathcal{S}_{wbg}$). In the third column starting from the left side the results of size measurements, without any prior background noise substraction before the AID computation, are presented ($\mathcal{S}_{wbg}$).

”true size” $\mathcal{S}$ (nm)	$\mathcal{S}_{wbg}$ (nm)	$\mathcal{S}_{bg}$ (nm)	N_{totb}
40 (λ_{ex} = 647 nm)	31.1 ± 4.2	35.7 ± 4.1	130
50 (λ_{ex} = 488 nm)	53.7 ± 1.9	53.4 ± 2.0	93
100 (λ_{ex} = 488 nm)	97.8 ± 4.6	95.7 ± 4.2	70
100 (λ_{ex} = 647 nm)	85.5 ± 4.4	83.9 ± 6.2	150

Table 4.2: Numerical presentation of nanosizing results obtained from 40 nm ∅ and 100 nm ∅ ”red beads”: Here, in detail, all the results shown graphically in Figure 4.3 are presented. N indicates a single independent data stack acquisition of an entire field of view; Columns A denote mean values plus/minus the standard deviation of the mean (SDM) of the size evaluations performed on each data stack (N = 1, 2, ⋯ 10) in the case the background noise was subtracted from the 3D data before the AID was evaluated ($\mathcal{S}_{wbg}$); columns B denote mean values plus/minus SDM of the size evaluations performed on each data stack in the case that the background noise was not subtracted from the 3D data before the AID was evaluated ($\mathcal{S}_{bg}$). For example, in the data stack N = 1 for the case of 40 nm ∅ ”red beads”, 13 single objects in the field of view were registered by SMI-microscopy. The mean size of these object was determined to be 31.9 ± 2.9 (SDM) nm. In data stack N = 2, the same 13 objects were measured again; in this case the mean size measured was 31.8 ± 4.3 (SDM) nm.

N	”true size” 40 nm $\mathcal{S}$ (nm)	”true size” 40 nm $\mathcal{S}$ (nm)	”true size” 100 nm $\mathcal{S}$ (nm)	”true size” 100 nm $\mathcal{S}$ (nm)
1	31.9 ± 2.9	33.8 ± 3.5	94.7 ± 2.1	95.4 ± 2.0
2	31.8 ± 4.3	35.9 ± 4.7	86.2 ± 2.4	90.2 ± 2.4
3	33.2 ± 4.0	33.4 ± 3.7	86.5 ± 2.5	86.5 ± 2.6
4	33.8 ± 4.4	36.1 ± 4.4	79.7 ± 2.5	72.7 ± 3.7
5	28.6 ± 4.8	33.6 ± 2.9	88.9 ± 2.0	83.6 ± 3.3
6	35.5 ± 3.4	33.6 ± 3.2	83.6 ± 2.8	83.4 ± 3.2
7	26.3 ± 3.9	33.3 ± 3.7	79.8 ± 2.7	78.6 ± 3.0
8	37.8 ± 6.2	40.2 ± 2.9	85.3 ± 2.5	83.7 ± 3.4
9	27.5 ± 2.6	32.9 ± 3.2	83.0 ± 3.0	80.9 ± 3.8
10	24.8 ± 3.9	30.5 ± 3.7	87.5 ± 2.6	84.0 ± 3.3
	A	B	A	B

Table 4.3: Numerical presentation of nanosizing results obtained from 100 nm ∅ ”green beads”: Here, in detail, all the results shown graphically in Figure 4.4 are presented. N indicates a single independent data stack acquisition of an entire field of view; Column A denotes mean values plus/minus the standard deviation of the mean (SDM) of the size evaluations performed on each data stack (N = 1, 2, ⋯ 10) in the case the background noise was subtracted from the 3D data before the AID was evaluated ($\mathcal{S}_{wbg}$); column denotes B mean values plus/minus SDM of the size evaluations performed on each data stack in the case that the background noise was not subtracted from the 3D data before the AID was evaluated ($\mathcal{S}_{bg}$). For example, in the data stack N = 1 for the case of 100 nm ∅ ”green beads”, 7 single objects in the field of view were registered by SMI-microscopy. The mean size of these object was determined to be 96.2 ± 2.4 (SDM) nm. In data stack N = 2, the same 7 objects were measured again; in this case the mean size measured was 93.8 ± 2.4 (SDM) nm.

N	”true size” 100 nm $\mathcal{S}$ (nm)	”true size” 100 nm $\mathcal{S}$ (nm)
1	96.2 ± 2.4	94.8 ± 2.1
2	93.8 ± 2.4	91.6 ± 2.6
3	94.6 ± 2.6	93.7 ± 1.8
4	95.6 ± 2.0	94.3 ± 2.7
5	93.5 ± 3.2	92.6 ± 1.9
6	100.3 ± 3.1	97.2 ± 2.6
7	100.7 ± 2.5	98.3 ± 2.2
8	106.1 ± 3.0	102.6 ± 2.5
9	103.8 ± 4.1	101.8 ± 2.7
10	93.5 ± 2.6	90.1 ± 2.6
	A	B

Table 4.4: Numerical presentation of nanosizing results obtained from 50 nm "green beads": Here, in detail, all the results shown graphically in Figure 4.5 are presented. N indicates a single independent data stack acquisition of an entire field of view; Column A denotes mean values plus/minus the standard deviation of the mean (SDM) of the size evaluations performed on each data stack (N = 1, 2, 3, 4) in the case the background noise was subtracted from the 3D data before the AID was evaluated ($\mathcal{S}_{wbg}$); column B denotes mean values plus/minus SDM of the size evaluations performed on each data stack in the case that the background noise was not subtracted from the 3D data before the AID was evaluated ($\mathcal{S}_{bg}$). For example, in the data stack N = 1 for the case of 50 nm $\varnothing$ "green beads", 20 single objects in the field of view were registered by SMI-microscopy. The mean size of these object was determined to be 54.5 ± 2.3 (SDM) nm. In data stack N = 2, 22 objects in the field of view were measured; in this case, the mean size measured was 50.4 ± 1.7 (SDM) nm.

N	"true size" 100 nm $\mathcal{S}$ (nm)	"true size" 100 nm $\mathcal{S}$ (nm)	N_{totb}
1	54.5 ± 2.3	53.9 ± 2.3	20
2	50.4 ± 1.7	52.6 ± 2.3	22
3	53.7 ± 2.8	53.7 ± 2.2	27
4	54.8 ± 2.0	55.3 ± 2.0	24
	A	B	

Table 4.5: Numerical presentation of nanosizing measurements performed on 40 nm $\varnothing$, 100 nm $\varnothing$ "red singular beads", and 100 nm $\varnothing$ "green singular beads": In this Table the results of "single" bead size evaluation, in the case of 40 nm $\varnothing$, 100 nm $\varnothing$ "red beads", and 100 nm $\varnothing$ "green beads" are presented. In each data stack the beads are arbitrary labeled with the number $\mathcal{N}_b$ see first column from the left side. Columns A show the results of size evaluation in the case the background noise was automatically subtracted before the AID was measured ($\mathcal{S}_{wbg}$); columns B show the same evaluations performed without any background noise subtraction was performed before the AID was measured ($\mathcal{S}_{bg}$).

	$\mathcal{S}_{40}$ (nm)	$\mathcal{S}_{40}$ (nm)	$\mathcal{S}_{100}$ (nm)	$\mathcal{S}_{100}$ (nm)	$\mathcal{S}_{100}$ (nm)	$\mathcal{S}_{100}$ (nm)
$\mathcal{N}_b$	$\lambda_{ex} = 647$ nm	$\lambda_{ex} = 647$ nm	$\lambda_{ex} = 647$ nm	$\lambda_{ex} = 647$ nm	$\lambda_{ex} = 488$ nm	$\lambda_{ex} = 488$ nm
1	27.6 ± 8.8	31 ± 11	91.4 ± 3.6	91.6 ± 3.8	93.1 ± 5.0	91.7 ± 4.8
2	20.6 ± 7.2	29.8 ± 7.8	96.3 ± 3.0	96.5 ± 3.2	96.9 ± 8.0	93.9 ± 6.5
3	26.2 ± 6.8	35.6 ± 8.0	92.0 ± 5.1	92.6 ± 5.8	90.9 ± 4.2	89.8 ± 5.1
4	42 ± 14	44 ± 13	89.4 ± 7.2	91 ± 10	105.9 ± 5.7	102.8 ± 4.7
5	28.9 ± 9.2	31.3 ± 9.3	79.8 ± 9.5	75. ± 11	96.9 ± 7.6	95.3 ± 5.6
6	20.7 ± 7.8	29.4 ± 7.6	78.2 ± 6.1	73.3 ± 9.9	97.9 ± 4.4	96.0 ± 3.9
7	36.8 ± 8.4	39.8 ± 4.8	83.1 ± 5.0	82.7 ± 5.3	102.6 ± 8.8	100.3 ± 7.1
8	27 ± 13	34.5 ± 6.8	72.6 ± 6.9	70.9 ± 7.8		
9	20.0 ± 8.3	26.4 ± 7.2	93.8 ± 5.9	93.5 ± 6.6		
10	32 ± 11	35.1 ± 9.9	91.7 ± 5.1	88.9 ± 8.4		
11	35 ± 11	34.7 ± 8.9	66.7 ± 7.4	60 ± 10		
12	56.9 ± 5.3	63.2 ± 4.3	84.6 ± 3.7	83.6 ± 9.2		
13	31 ± 11	28.6 ± 9.2	85 ± 11	81 ± 13		
14			91.9 ± 4.9	92.0 ± 4.9		
15			86.5 ± 6.9	86.5 ± 6.9		
	A	B	A	B	A	B

4.3 A second series of Measurements

In Section 4.2 the focus of the research was to start to discover the accuracy limits of size evaluations. Expecially was shown that high accuracy evaluations can be performed using both the excitation wavelengths of the Heidelberg SMI microscope. Furthermore the stability of the system respect of repetitive size measurements of the same object was studied (see Table 4.5). Here the main goal is to show the present experimental limits in size evaluations using the Heidelberg SMI microscope. According with the SMI-VIM models and simulations shown in Chapter 2 and in Chapter 3 the excitation wavelength of the Heidelberg SMI microscope that allows the smaller subwavelength size measurements is $\lambda_{ex} = 488$ nm. Therefore a big series of size measurements were performed only using fluorescent particles (beads) excitable with $\lambda_{ex} = 488$ nm, having 26 nm, 40 nm, 44 nm, 50 nm, 57 nm, 71 nm, 85 nm, 100 nm and 140 nm diameter according with the values given by the the manufacturer (Duke scientific corporation Palo Alto California). Using the definition of size resolution given in Chapter 3 the limits of statistical and singles size measurements were studied. In the margin of this research a comparison between size evaluation performed on different specimen (produced by different manufacturer) but characterized by the same size (100 nm $\varnothing$) is presented.

4.3.1 A marginal but interesting experiment

After several different sized beads were ordered by Duke scientific corporation, the Heidelberg SMI group had in dotation three set of 100 nm $\varnothing$ beads excitable with $\lambda_{ex} = 488$ nm produced by three different manufacturer (Molecular Probes, Duke lab, Bio lab SN). It comes spontaneously to perform measurements with that beads as a test of their quality. Furthermore according to the theory high precision size measuremets can be performed with that specimens. The acquisitions were performed following the same procedure as in the previous section. Furthermore the results shown in Chapter 4.2 indicates that a previous substraction of the background does not lead to systematic errors when 100 nm $\varnothing$ beads were measured, then only evaluation after a previous substraction of the background were performed; the reason that justify this choice is that the adaptation function described in equation 4.1 is more simple to handle when one parameter is deleted (i.e. $L = 0$). For each set of beads one probe was prepared; for each probe the estimate of the size is given by the mean of the size measurements performed on a N_{totb} number of independent beads; the estimate of the error is the standard deviation SD on that measurements. Note that only one measurement of each data set was performed and not multiple repetitions as mostly in Section 4.2. The results shown in Table 4.6 are in good agreement and prove one time more the stability of the SMI-VIM size evaluations algorithms.

Table 4.6: Left side column: nominal value of the beads given by the manufacturer: (A) Molecular Probes; (B) Duke Lab; (C) Bio lab SN.
Central column: SMI measured values (nm).
Right side column: total number of beads measured N_{totb}.

Nominal value (nm)	Measured value (nm)	N_{totb}
100 (A)	102.5 ± 5.7	83
100 (B)	101.4 ± 4.9	64
100 (C)	102.6 ± 5.3	86

4.3.2 Limit of Size measurements with an SMI-Microscope

In Chapter 3 (see expecially Section 3.3.2 and Section 3.3.4) was pointed out that the present SMI microscope experimental configuration in combination with the SMI-VIM evaluations tools has its size determination limit near 40 nm for $\lambda_{ex} = 647$ nm and near 30 nm for $\lambda_{ex} = 488$ nm. In other words it become very critical distinguish differences in the object size when this is in the range of $\lambda_{ex}/16$ or better in the range of 1/3 the fringe FWHM ($\simeq$ 81 nm for λ_{ex} = 488 nm and $\simeq$ 108 nm for $\lambda_{ex} = 647$ nm). Considering that the FWHM of the standing wave field determines the oscillating properties of the AID became intuitively understandable that for the system objects which axial extension is 2 or 3 time less big than FWHM of the fringes presents the same physical properties (barycentre position in to the fringe and size). In the previous section measurements regarding 40 nm diameter red beads were pereformed and the results were shown. Unfortunately not other specimens were avaliable (e.g. with a nominal diameter of 50 nm) to study the sensitivity of the system in that range and to prove that this is a real limit of the size evaluations using $\lambda_{ex} = 647$ nm. For the case of green channel ($\lambda_{ex} = 488$ nm) was possible to study the limits of size evaluations; two different kind of fluorescent particles were tested. First a preparation (for details see Section 4.2) made by 26 nm ∅ beads was measured. These beads were provided by Duke lab even with the estimation of the maximal variation of their size. In a second time measurements with 40 nm ∅ beads (Molecular Probes) were performed. The results are shown in table 4.7; measurements using the green channel down to at least 30 nm are feasible. Even if the criteria of size resolution is not fulfilled between 26 nm ∅ beads and 40 nm ∅ beads, however, computing the mean value of the size of the elements of each preparation it is possible to distinguish an ensemble of 26 nm ∅ beads from one made by 40 nm ∅ beads. Anyway, what it is possible really to show, is the present limit of the instrument. This limit can be overcame if some technical problems will be resolved. First a non homogeneous background along the z planes disturbs the evaluations expecially in the case in which the total number of detected photons and the signal to noise ratio is not so high. This problem probably is due to the specimen preparation: cover slip and object slide reflect the light in different ways creating a not homogeneous illumination along the z axis. The solution could be just build up a new object holder that support preparation made on coverslip covered by coverslip. Another problem is to create preparations were the beads are not clustering together. This is very difficult expecially when the specimen has a diameter down to 40 nm or less. In this case is not enough make huge solution of the beads and treat them with ultrasonic impulse and use several other precautions that normally works with bigger beads. Although the more important problem regards the visualization software.[2,5,54,55,56] After an acquisition is terminated it is not possible to establish online[2,5] if these problematic specimen are useful or not. There is a big bug in the visualization software expecially regarding the option of subtracting the background noise. This operation is performed in such a way that the mean background is evaluated on all the acquisition plane. As it is clear the background is constant on small planes and not on a big acquisition window (several effect even a not perfectly homogeneous density of the specimen lead to it) then when it is necessary to perform acquisition in a large experimental window this process produce strange and not useful intensity profiles. The reader should note that a big acquisition window is necessary when low beads density specimen are prepared in order to avoid clustering. This problem can be resolved easily just restricting the area in which the background noise has to be computed around the time to time select visualization point.

Table 4.7: Left side column: nominal beads size values (provided by the manufacturer; note that the accuracy limits of the specimen given by the manufacturer only inthe case of 26 nm ∅ beads was assumed as an estimation of the error.
Cental column: the evaluated value of the size of the particles is the mean values on all the size evaluation and the accuracy is considered proportional to the inverse of the standard deviation.
Right side column: total number of beads constituting the specimens N_{totb}

Nominal value (nm)	Measured value (nm)	N_{totb}
26.0 ± 6.0	31.6 ± 7.6	82
40	43.2 ± 6.5	149

4.3.3 Size resolution and SMI size measurements

All the experimental problems discussed in the previous section help to understand that the measurements here shown indicate only a starting point for a future developing of the SMI instrument. Anyway the results shown in the previous Section and in the present Section are really very innovative in microscopy. So far in light microscopy no measurements were presented that shown size measurements down 100 nm. Here several size measurements far down 100 nm were effectively made. Even more a size resolution (for the definition see Chapter 3) of 30 nm is shown and it is proved that measurement with a statistical accuracy down to 10 nm are feasible. Following the procedure indicate in Section 4.2 several specimen were prepared and for each of them one acquisition was performed. These specimen were constituted by green beads with nominal (according to manufacturer) size between 26 nm and 140 nm: 26 nm; 40 nm; 44 nm; 50 nm; 57 nm; 71 nm; 85 nm, 100 nm; 140 nm. After the acquisition process was terminated for each specimens a total number of N_{totb} was individuated and the size of them evaluated using SMI-VIM algorithms. The mean calculated on the N_{totb} measurements, for each beads preparation, was considered as the estimate of the size and the standard deviation on that measurements was considered as the estimation of the accuracy. Figure 4.7 and Figure 4.8 in combination with Table 4.8 are useful to visualize the results of this experiments. The accuracy of size evaluation is stable around the 10% of the mean value estimate; this means that is possibles to distinguish two different ensemble of beads when their mean values differ more than 10 nm. As it is shown expecially in Figure 4.8 the size resolution limit is around 30 nm; for example the distribution of measurements regarding 50 nm ∅ beads and 85 nm ∅ beads are completely separated as the distribution of 71 nm ∅ beads and 100 nm ∅ beads. Several reasons justify a size resolution three time bigger than the theoretical previsions (see chapter 3). It is necessary to add to all the experimental problems discussed in Section 4.3.2 even the fact that a high rate bleaching still strongly perturb measurements regarding fluorescent objects. The bleaching effect leads to not optimal photon count conditions and sometime some of the conditions that allow size measurements are not effective. In presents of high rate bleaching it is not always possible to consider the object to be measured homogeneously covered of fluorochromes and then all the size evaluation calibration algorithms are not valid. The fact that all these measurements were performed so far to ideal conditions enhance once more the quality of the scientific results shown.

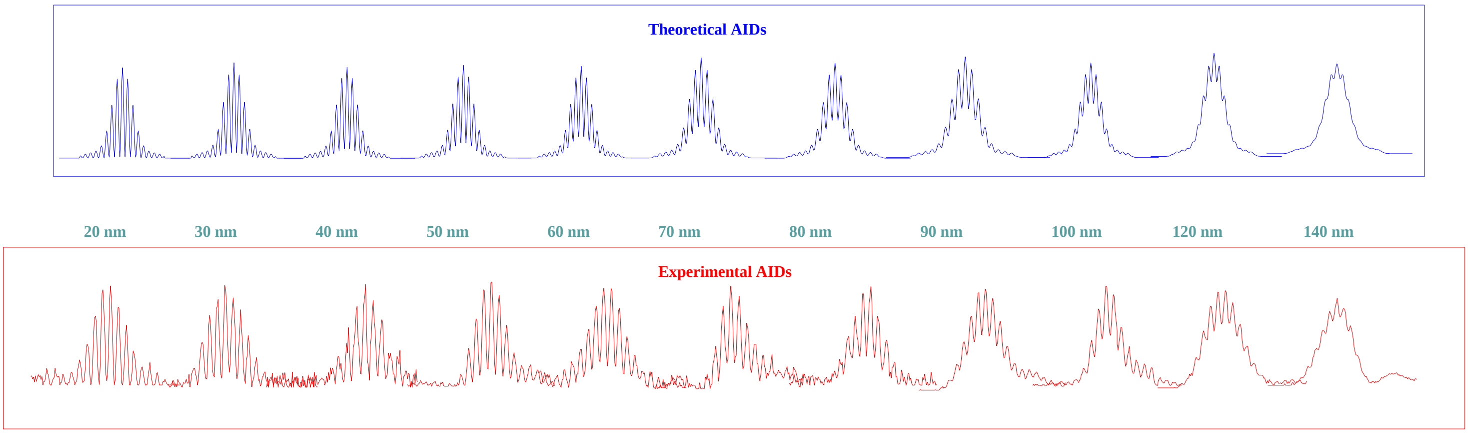

Figure 4.6: A gallery of different AID; Top: Ideal AIDS produced by VIM.
Bottom: experimental measured AIDs. Note that the AIDs in both case, for a matter of visualization, are not printed in scale.

Table 4.8: Comparison between the nominal value of the beads given by the manufacturer (left side column) and the evaluated values of the same beads (mean ± SD) (see central column). Note that in the on the right side column the total number of bead detected (N_{totb}) for each specimen is reported.

Nominal value (nm)	Measured value (nm)	N_{totb}
26.0 ± 6.0	31.6 ± 7.6	82
40	43.2 ± 6.5	149
44.0 ± 6.6	47.0 ± 4.1	76
50	50.4 ± 5.4	171
57.0 ± 8.1	61.8 ± 5.5	60
71.0 ± 7.1	69.4 ± 5.0	114
85.0 ± 8.5	81.3 ± 4.8	36
100 ± 10	101.4 ± 4.9	64
140 ± 14	133 ± 14	88

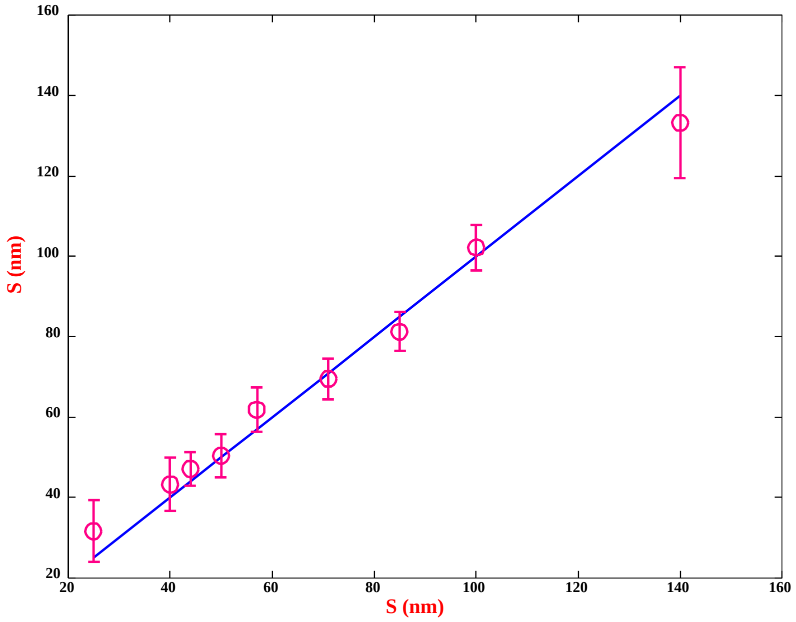

Figure 4.7: Abscissa: ”True size” $\mathcal{S}$
. Ordinate: ”True size” $\mathcal{S}$
Continuous line: ”True size” versus ”True size”; circle experimental mean estimated values of the size of different ensemble of beads; bars standard deviation (SD) of these estimates

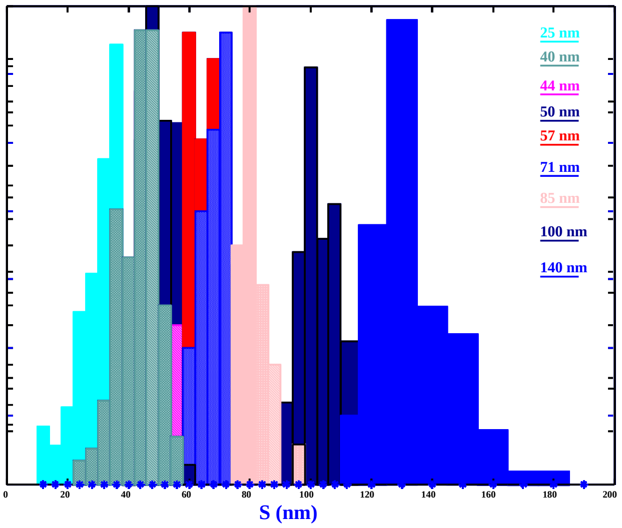

Figure 4.8: Superposition of all the size distributions measured. This Figure helps to understand which is the size resolution limit in which different sized objects it is possible to distinguish. For example the distribution relative to beads with nominal diameter of 44 nm is complitely covered by the distribution of 50 nm nominal diameter beads and 40 nm nominal diameter beads. This means that it is not presently possible neither statistically to distinguish different sized objects in a range of 5 nm.

Chapter 5

Experimental Topology Measurements

5.1 Introduction

In several application of modern physics expecially in quantitative structural cell biology research it is important to measure with high accuracy small distances between a multitude of specifically labelled and accurately localized fluorescent intracellular objects. Using SPDM the objects to be measured are labeled with fluorescent markers that use different spectral signatures, thus allowing identification of the objects owing to their excitation emission spectra or fluorescence lifetime. The positions of the objects are then determined from their coordinate in the image data file by use of e.g., the fluorescence intensity barycentre. Knowledge of the geometrical optics of the system alllows calculation of the object position in the object space. To measure distances in the order of less then 20 nm often required for the analysis of functional supramolecular biostructures fluorescence resonance energy transfer techniques (FRET) are applied. Such approaches allow measurements of individual distances down to about 10 nm. However FRET techniques seem to not have capabilities to investigate the topology of an ensamble of multiple object. The theoretical simulations shown in Chapter 2 indicate that axial distances with an accuracy of one nanometer can be reached even under low photon count condition using SMI microscopy. Here series of experimental measurements will demonstrate that distance evaluation with an accuracy of one nanometer are feasible using SMI microscopy.

5.2 Distance measurements procedure in SMI microscopy.

5.2.1 Measurements

The experimental setup was briefly described in the previous Chapter. In order to calibrate the accuracy in topological measurements with the SMI microscope fluorescent microspheres were used (Tetraspeck beads Molecular Probes Eugene Oregon) with the diameter of 100 nm (according to the manufacturer and to SMI size evaluations), and with different excitation and emission peaks (the absorption emission peak at 660/680 nm was used). These beads had the advantage of having a low bleaching rate in the red spectrum, thus allowing multiple 3D SMI measurements. Furthermore that beads present a high signal to noise raton then the abberations due to the non costant background noise are irrelevant. A suspension of beads was dropped onto an object slide. After the beads had dried, Vectashield embedding medium (Vector Laboratories Burlingame, California) was applied to mount them on the object slide; then they were covered with a conventional coverslip. Theoretically the beads deposited on the object slide should have the same axial position and different lateral coordinate. In reality, there are some deviation from the ideal configuration such as roughness of the glass, the exciting wavefield, variance of diameter and shape of the beads, and sometime non homogeneity of the fluorochrome lier that cover the beads. These deviations leeds to small deviations, e.g. in the order of few nano meter, in the axial positions of the beads. The measurements were performed by the recording of 3D data stacks; each stack contains 200-400 two dimensional (2D) images (lateral optical section) with 64x64 pixels including several fluorescent objects. The acquisition process was the same as described in Section 4.2. To measure the reproducibility of the axial distance measurements between the fluorescent targets, for each area a 3D data stack of the same objects was measured independently in ten consecutive 3D registrations. Thus one 3D serie consisted of ten independent 3D data stacks. For evaluation in each 3D data stacks the same objects was identified and localized. Figure 5.1 shows a typical axial intensity distribution of one object where in the top the row data is displayed and in the bottom the same data is displayed after substraction of the background noise. For distance determination, adaptation curves calculated with appropriate algorithms (see equation, 2.3 equation 4.1 and below). To clearly separate the objects from each other, objects with lateral (x, y) distances from each other larger than the optical resolution (500 -800 nm) were selected. Here the results relative to three series of measurements will be presented.

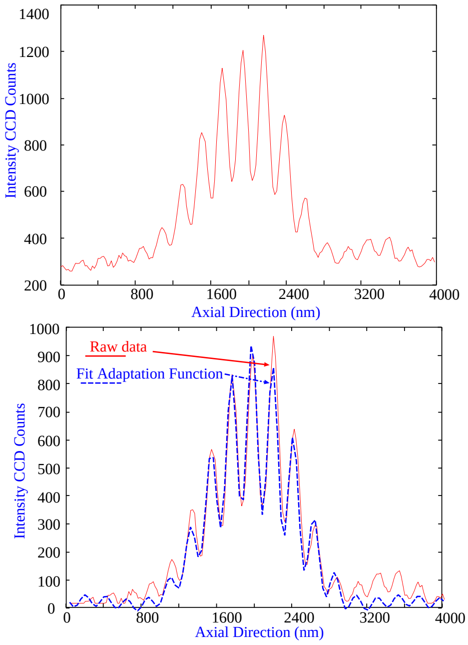

Figure 5.1: Typical axial intensity of one fluorescent object for the axial distance measurements (Tetraspeck bead, diameter 100 nm, λ_{ex} = 647 nm.)
Top: Measured intensities (raw data); Bottom: Raw data after subtraction of the background noise. Dashed curve, calculated adaptation function.

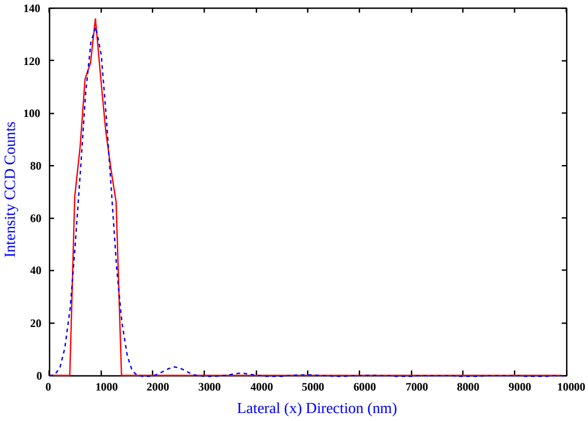

Figure 5.2: Typical lateral intensity of one fluorescent object for the lateral distance measurements (Tetraspeck bead, diameter 100 nm, λ_{ex} = 647 nm.)
Raw data is shown after subtraction of the background noise. Dashed curve, calculated adaptation function.

5.2.2 Algorithms

The determination of the distances were made with different algorithms; two different non linear least square algorithms were used one for extract information from the lateral intensity distribution (LID) of the objects, the other, detailed described in the previous Chapter for extract information from the AID.

5.2.3 Lateral evaluations

The procedure of lateral distances measurements is divided in two parts. First using the brighest 2D image plane of each 3D data stack the objects were manually identified and a volume 9X9X(200-400) were selected around them. The LID (relative to the x, y axis) only for the previous mentioned region was extracted. After a non linear least square fit was used in order to find the maximum of the intensity that theoretically coincide with the intensity barycentre of the measured object. This adaptation function is closer to the theoretical expression of LID:

$$LID\Big[x(y)\Big] = AJ_0^4\left[\frac{x(y) - x_{max}(y_{max})}{B_{xy}}\right]; \qquad (5.1)$$

where J_0 is the Bessel function of the first kind and zero order, A is positive parameter proportional to maximum of the intensity, $x_{max}(y_{max})$ corresponds to the position of the maximum of the LID and B_{xy} is a positive parameter proportional to FWHM of the LID.

5.2.4 Axial evaluations

How to determine the axial distances between two objects was described in details in Section 1.2.3; expecially the equation 1.4 will be used after $z_{01(2)}$ is computed using AID(z) (see equation 4.1) as adaptation function after the background noise is subtracted.

5.3 Results

The results of three series of measurements will be here presented: axial and lateral distance measurements were performed in all the cases.

5.3.1 Lateral distance measurements

Serie 1:

In this Serie seven objects (obj1, obj2,...,obj7) were localized, then 21 distances were calculated. The results are shown in Table 5.1. In the lateral direction the mean error was 8.6 nm for x direction, and 9.7 nm for y direction.

Table 5.1: Results of lateral distance determinations in SMI microscopy: All the distances between 7 object were measured. Note that it was possible to determine lateral distances with an error down to 5 nm. The estimate of the error is the standard deviation of a whole set of measurements (10).

x (nm)	x (nm)	x (nm)	x (nm)	x (nm)	x (nm)	x (nm)
	obj2	obj3	obj4	obj5	obj6	obj7
obj1	715.2 ± 8.2	2991 ± 10	3692.1 ± 7.2	2493.4 ± 8.6	4105 ± 12	1116.8 ± 8.4
obj2		2275.9 ± 5.3	2976.8 ± 5.0	1778.1 ± 8.0	3390.6 ± 8.3	401.5 ± 6.8
obj3			700.8 ± 8.9	497.8 ± 9.9	1114.7 ± 8.7	1874.4 ± 9.1
obj4				1198.7 ± 7.2	413 ± 11	2575.3 ± 5.5
obj5					1612 ± 13	1376.6 ± 7.7
obj6						2989 ± 11
y (nm)	y (nm)	y (nm)	y (nm)	y (nm)	y (nm)	y (nm)
	obj2	obj3	obj4	obj5	obj6	obj7
obj1	836 ± 10	825 ± 11	101 ± 11	1616.1 ± 9.2	2415 ± 12	2506 ± 13
obj2		10.7 ± 5.9	734.5 ± 7.5	2452.6 ± 6.8	3252.2 ± 9.3	3342.8 ± 8.8
obj3			723.9 ± 9.3	2442.0 ± 7.4	3241 ± 10	3332.3 ± 9.0
obj4				1718 ± 10	2517 ± 12	2608 ± 10
obj5					1361 ± 13	90.6 ± 7.1
obj6						1271 ± 12

Serie 2:

In this Serie four objects (obj1, obj2, obj3, obj4) were localized, then 6 distances were calculated. The results are shown in Table 5.2. In the lateral direction the mean error (SD) was 17.6 nm for x direction, and 15.1 nm for y direction. Here the error in distance determination is quite twice the previous Serie. However even in this not optimal experimental conditions an error of only 5.4 nm was measured in at least one case. This means that a high accuracy in topology measurements is a real property of the SMI microscope.

Serie 3:

In this Serie four objects (obj1, obj2, obj3, obj4) were localized, then 6 distances were cal-

Table 5.2: Results of lateral distance determinations in SMI microscopy: All the distances between 4 object were measured. Note that it was possible to determine lateral distances with an error down to 5 nm. The estimate of the error is the standard deviation of a whole set of measurements (10).

x (nm)	x (nm)	x (nm)	x (nm)
	obj2	obj3	obj4
obj1	1234 ± 12	2746 ± 19	3405 ± 26
obj2		1511 ± 11	2170 ± 18
obj3			659.1 ± 9.1
y (nm)	y (nm)	y (nm)	y (nm)
	obj2	obj3	obj4
obj1	2326 ± 18	2293 ± 23	1243 ± 23
obj2		32 ± 10	1082 ± 11
obj3			1050.2 ± 5.4

culated. The results are shown in Table 5.3. In the lateral direction the mean error (SD) was 9.5 nm for x direction, and 13.2 nm for y direction. Even in this serie errors down 10 nm were measured.

Table 5.3: Results of lateral distance determinations in SMI microscopy: All the distances between 4 object were measured. Note that it was possible to determine lateral distances with an error down to 6 nm. The estimate of the error is the standard deviation of a whole set of measurements (10).

x (nm)	x (nm)	x (nm)	x (nm)
	obj2	obj3	obj4
obj1	826 ± 11	630 ± 10	336.4 ± 7.9
obj2		1457 ± 13	489.5 ± 6.3
obj3			967.4 ± 9.0
y (nm)	y (nm)	y (nm)	y (nm)
	obj2	obj3	obj4
obj1	1319 ± 19	1588 ± 13	4799 ± 17
obj2		269 ± 10	3479 ± 11
obj3			3210.8 ± 9.4

5.3.2 Axial distance measurements

Serie 1:

In this Serie seven objects (obj1, obj2,...,obj7) were localized, then 21 distances were calculated. The results are shown in Table 5.4. In the axial direction the mean error was 2.0 nm. Once an error less of one nanometer was registered (relative to the distance between obj3 and obj4). Anyway high resolution and accuracy axial distance evaluation are feasible normally with the present SMI setup. It seems not to be a matter of luck to reach in axial direction an accuracy between one and 2 nanometer.

Table 5.4: Results of axial distance determinations in SMI microscopy: All the distances between 21 object were measured. Note that it was possible to determine axial distances with an error down to 0.7 nm. The estimate of the error is the standard deviation of a whole set of measurements (10).

z (nm)	z (nm)	z (nm)	z (nm)	z (nm)	z (nm)	z (nm)
	obj2	obj3	obj4	obj5	obj6	obj7
obj1	6.6 ± 2.6	2.0 ± 1.6	2.3 ± 1.8	6.5 ± 2.3	1.7 ± 2.2	6.4 ± 3.1
obj2		8.7 ± 1.3	4.3 ± 1.2	0.12± 1.5	4.9 ± 2.2	12.9 ± 2.7
obj3			4.33 ± 0.70	8.5 ± 1.2	3.7 ± 1.6	4.3 ± 2.6
obj4				4.2 ± 1.2	0.6 ± 1.4	8.6 ± 2.2
obj5					4.8 ± 2.3	12.8 ± 3.0
obj6						8.1 ± 2.6

Serie 2:

In this Serie four objects (obj1, obj2,obj3, obj4) were localized, then 6 distances were calculated. The results are shown in Table 5.5. In the axial direction the mean error was 2.1 nm. Once an error of one nanometer was registered (relative to the distance between obj1 and obj4). The results shown in Table 5.5 are almost all in details shown in Figure 5.4. In this Figure the lines follow the results of single distance measurements along all the series. The comparison between Figure 5.4 and Figure 5.3 indicates that almost quite all the systematic perturbation that disturb topology absolute measurements were neutralized in this kind of measurements. In Figure 5.3 are shown the measured axial absolute positions of the four objects detected in serie 2. A strong drift of the absolute position appears clear; the reasons of this effect can be several e.g. vibration of the object stage defects of the step motors etc. etc.

Table 5.5: Results of axial distance determinations in SMI microscopy: All the distances between 4 object were measured. Note that it was possible to determine axial distances with an error down to 1 nm. The estimate of the error is the standard deviation of a whole set of measurements (10).

z (nm)	z (nm)	z (nm)	z (nm)
	obj2	obj3	obj4
obj1	6.7 ± 2.6	17.9 ± 2.9	5.4 ± 1.0
obj2		11.3 ± 2.0	1.3 ± 2.0
obj3			12.5 ± 2.4

Serie 3:

In this Serie four objects (obj1, obj2,obj3, obj4) were localized, then 6 distances were calculated. The results are shown in Table 5.6. In the axial direction the mean error was 1.2 nm. All the measurements present an error close to one nanometer.

Few considerations: Serie 1 presents an average error in 3D distance determination 13 nm. One of the more precise measurements made on this series regards the 3D distance between obj2 and obj4:

$$D3D(obj2, obj4) = (3066.1 \pm 9.1)nm$$

; a distance in the order of μm can be measured with an error less than 10 nm with the SMI microscope in a quite normal experimental configuration.

Serie 2 presents an average error in 3D distance determination 23 nm. Even in this case super 3D distance resolutions can be reached:

$$D3D(obj3, obj4) = (1239 \pm 11)nm$$

;

Serie 3 presents an average error in 3D distance determination 16 nm. In this case one of the more precise 3D evaluation is:

$$D3D(obj2, obj4) = (3513 \pm 12)nm$$

;

Axial distance evaluations in the order of 1 and 2 nanometer are a standard for an SMI microscope under normal experimental conditions that allow the possibilities to program high research biological measurements. SMI-VIM (see Chapter 2) simulations have told that the limit in accuracy for topological evaluation are still far to be reached. The system can be improved in several parts:

1. The software is week[2,5,54,55,56] and not allow online biological visualization (see the end of Chapter 4).
2. the optical componends are assambled in a not professional way. Several light abberation are due to this fact: For example the laser beam waist is bigger than the diameter of the lenses and mirrors present in the microscope.

3. The combination of conventional object slide and cover slip gives rise to a not uniform illumination along the z axis.
4. the extreme difficulties to change few lenses to focalize the emitted radiation on the CCD camera in order to reduce from 107 nm to 50-60 nm the lateral voxel size. This simple operation can increase of a factor two the system precision in the lateral plane.
5. Last but not least: the difficulty of some colleagues to understand that methods of barycentre determination (intensity gravity centers) based on thresholding are far to be the optimal solution for reach high precision measurements in optics. This problem is the only that seems to possible to be resolved; the prove is that such wonderful 3D evaluation still wait for be published in another contest than the present work. For information that data is more than one year old and only the axial part is published.

This "war bulletin" sound like an accuse but is only the prove that the system even far away from the best experimental conditions can give wonderful results; such measurements are just a starting point for future developments.

Table 5.6: Results of axial distance determinations in SMI microscopy: All the distances between 4 object were measured. Note that it was always possible to determine axial distances with an error down to 1 nm. The estimate of the error is the standard deviation of a whole set of measurements (10).

z (nm)	z (nm)	z (nm)	z (nm)
	obj2	obj3	obj4
obj1	0.0 ± 1.4	8.3 ± 1.3	1.3 ± 1.4
obj2		8.37 ± 1.0	1.29 ± 1.1
obj3			9.67 ± 1.2

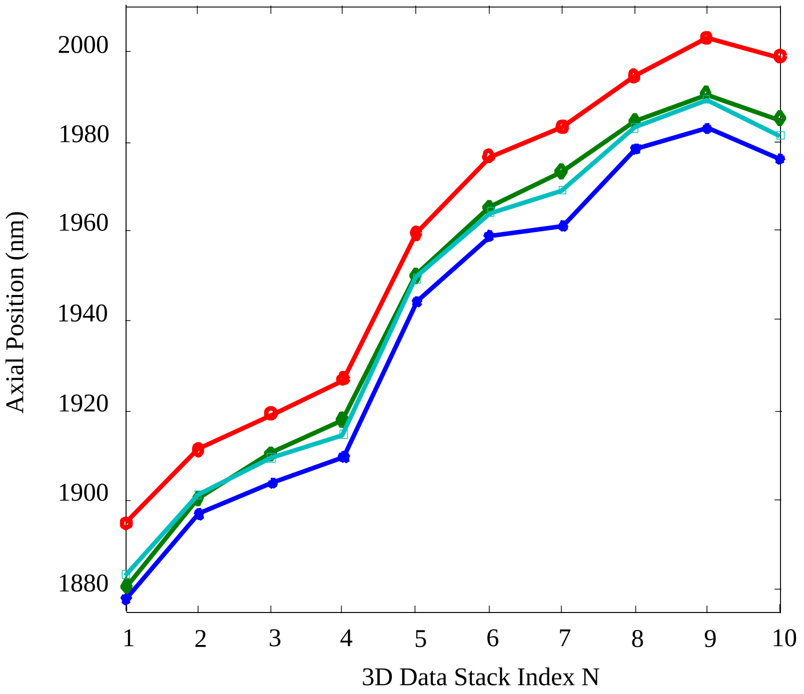

Figure 5.3: Measured consecutive axial positions of the four objects relative to series 2.
Abscissa: 3D data stack index, respectively, of consecutive, independent 3D measurements. The axial object positions were changed in almost identical manner.

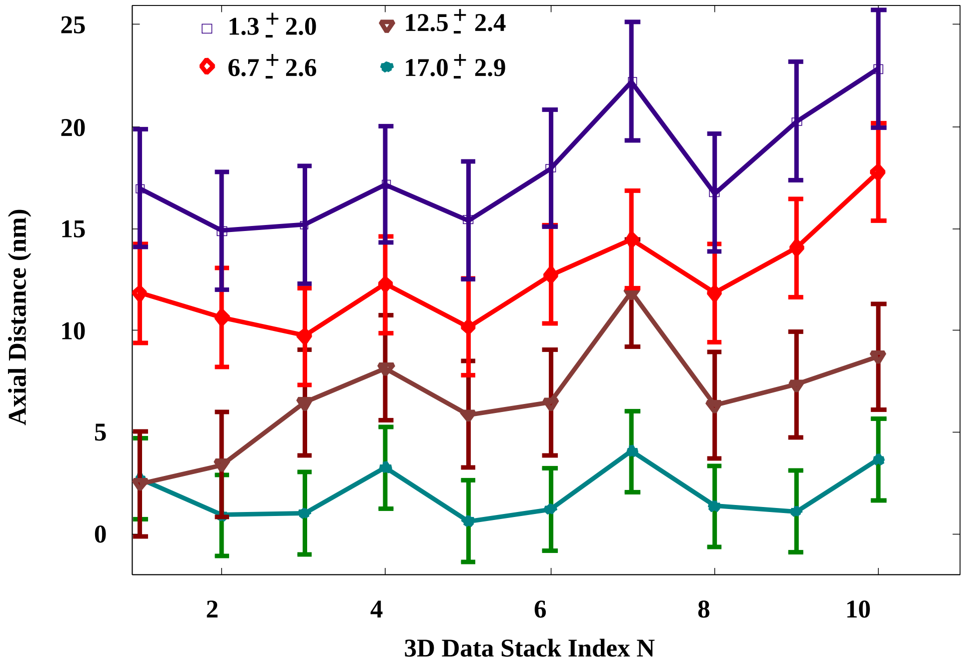

Figure 5.4: Axial distances between two objects (results shown in Table 5.5).

Chapter 6

Biological Applications

The determination of the size of individual objects is one of the main applications of microscopy. This has become of special importance in the biosciences. For example, topological analysis of three dimensional nano-structures of complexes of biological macromolecules, "biomolecular machines" (BMM), is one of the major goals in modern cell biology. In most cases, such biomolecular machines have a size (diameter for spherical objects/extension in a given direction) below some 100 nm. In particular, it is highly important for a deeper understanding of functional topology of the genome[13,14,15,16,38,64] to analyze individual specific chromatin regions (composed of DNA and proteins). Another example is the investigation of the organisation of "transcription factories"[58,59,60,61,62,63] where DNA sequences are transcribed into RNA sequences, or to study the organization and the evolution of "replication factories"[60] where DNA sequences are replicated, i.e copies with identical sequence are produced. Mutual distances between the barycentre (BC) of the BMM "elements" (BC: "fluorescent intensity gravity center" following specific labeling with suitable fluorochromes) and their sizes measured by SMI microscopy, provide important structural information. Although in recent years substantial progress was realised by X-ray and Electron Microscopy (EM) analysis of such "biomolecular machines", these techniques did not allow the elucidation of the "in vivo" conformation. While atomic force microscopy and Scanning Near field Optical Microscopy (SNOM) permit to study biological nanostructures with high optical resolution if positioned at a surface, an analysis of such structures in the interior of cells would be possible by far field light microscopy only. The small size of many of these biological nanostructures, until recently excluded Far Field Light

Microscopy (FFLM) from such studies. In this Chapter an advanced biological experiment will be performed by SMI-microscopy. The final goal of this experiment is to estimate the mean size of the transcription factories. The writer may note that whatever is the result of this estimation, at the moment it is possible, in light microscopy, to perform such experiment only using SMI microscopy.

6.1 Transcription factories

Transcription is the first step in the expression of the genetic information contained in DNA, and is performed by molecular machines called RNA polymerase.[58,59,60,61,62,63] Eukaryotic organisms contain three types of polymerase (I, II and III) that transcribe specific groups of genes. Polymerase II transcribes the most varied group of genes, including those encoding for proteins. It has been shown that polymerase II complexes are present in discrete nanostructures called "transcription factories" each containing, on average, 8 active polymerases. For example, the nucleus of the human cell line (HeLa), with volume 500-1000 μm^3, contains $\sim$ 80,000 active polymerase II in only $\sim$ 10,000 factories.[63] With confocal microscopy, these sites can not be resolved from each other in optical sections, necessitating the use of ultrathin ($\sim$ 100 nm) cryosections. Thin cryosections also provide excellent sensitivity, and can be used for both light and electron microscopy (LM and EM, respectively).[61] The size of transcription factories has been estimated to be $\sim$ 40-50 nm in diameter by EM. However, EM requires the use of three layers of antibodies (each with length 9-20 nm) to achieve maximum sensitivity; this may lead to an overestimation of size. EM is also an expensive, highly skilled and time-consuming technique, for which SMI microscopy could be an important alternative.

6.2 Important experimental details

6.2.1 Sample preparation

In collaboration with S. Martin and Dr. A. Pombo (Nuclear Organisation Group, Medical Research Council Clinical Sciences Centre, London, UK), we set out to test the applicability of SMI for measuring the size of transcription factories in ultrathin cryosections. Sample preparation (by S. Martin at the MRC-CSC, London HeLa cells (human carcinoma cell line) were fixed in paraformaldehyde, infused with sucrose (a cryoprotectant) and frozen in liquid nitrogen. Cryosections (90-150 nm thick) were cut using a cryoultramicrotome, and transferred to glass coverslips. Pol II transcription factories were indirectly immunolabelled with a mouse IgM antibody (H5) and an anti-mouse IgG/IgM antibody conjugated with Alexafluor488 fluorochromes. The sections were counter-stained with TOTO-3, a nucleic acid stain, to identify the nucleus of cells and the coverslips mounted in Vectashield on glass microscope slides and sealed with nail varnish.

6.2.2 Image collection on the SMI microscope.

A brief description of the Heidelberg SMI microscope is in Chapter 4. Cryosections counterstained with TOTO-3 were located using the 647 nm laser, and image sequences collected (160-180 images/stack) using the 488 nm laser and the 647 nm laser simultaneously or separately with integration times of between 0.5 and 5 seconds (S. Martin, at Kirchoff Institute of Physics). Stored images were analysed with the SMI software and the co-ordinates of individual foci (transcription factories) manually recorded (S. Martin and A. Kroll, Kirchoff Institute). These co-ordinates were then used (the procedure will be described in the following section) by the author of this work to obtain SMI profiles and size measurements of the foci.

6.3 Data analysis and results

Ten different specimen were used to be analysed. Two different individual foci random selection were made, the first in Heidelberg after the acquisition was made on all the ten specimen by S. Martin and A. Kroll, the second several months later in London by Sonya Martin in London using only five specimens; the second selection was made on the five specimens characterized by the higher signal to noise ratio. A first analysis was made on the individual foci selected in Heidelberg in order to establish a data analysis procedure that avoid, the more is possible, ambiguous results and systematic drift of the results produced by the experimental user. Actually one of the problem in modern sciences is the reproducibility of experimental results and how them are influenced by the scientist. Expecially in biology the risk of data drift caused by the subconscious desire of the scientist to reach his goal is high because the experimental approach is different than in physics (all the collateral effect present in the phenomena are often more important than the average physical quantities that there are leading it) and because the results of the experiments are really open to be interpret in several ways. Knowing all these problems I decided to analyse all the first data selection using eight different methods. Each method theoretically have to lead to the same result. Expecially the eight methods differs only for what regards the extraction of the SMI AID and least square procedure to obtain the values of the modulation contrast R. Then these procedures were applied to the data consecutively and after from the measured values of R the object size $\mathcal{S}$ was evaluated. In this way i did not know the final results using one algorithm before a new algorithm analysis was started. It was also interesting made this kind of evaluation as the test of accuracy of size evaluation under different SNR conditions (or different photon count conditions N_{tot}). Repeat in a little different way the data analysis of one spot could be a nice way to estimate the accuracy of this single measurement when, as often happens in a biological experiment, it is not possible to have several independent acquisitions regarding the same individual spot.

6.3.1 Eight different data analysis approaches

The 8 methods differed in three ways; the co-ordinates used to extract the AID, cutting the AID and background noise subtraction. In all the cases the fit procedure requires the user to choose suitable starting values for each of the parameters (this choice is lead by experience) and then to run the fit routine. The user can then decide if the adaptation function is a good representation of the extracted data or not.

Foci co-ordinates:

.A) Methods 1-4:

The foci (selected by eye) are cut from the main file in small 9x9x(160-180) files and the axial projection is performed using a 3x3 mask centred on the foci co-ordinate. In order to compensate for possible drift of the foci barycentre along the data set, intensity profiles were extracted using the mean intensity from this 3x3 mask. A fit was then performed in order to extract the size parameters. The relation between the size $\mathcal{S}$ and the fit parameters is given by equation 4.2

.B) Methods 5-8:

The foci are extracted in a 5x5x(160-180) file centred on the foci co-ordinates (selected by eye). The actual barycentre of the foci is then defined as the position of maximum intensity in this 5x5 file for each image (160-180). This new position is then used to produce the AID.

Cutting AID:

.A) Methods 2, 4, 6 and 8:

To gain an informative AID 100 axial planes are usually enough therefore uninformative, noisy axial planes at the extremes of the AID can be removed. To achieve this the maximum of the AID is taken to be the centre of the image and the data from only the 50 images either side of it are passed through the fit routine.

.B) Methods 1, 3, 5 and 7:

The AID is not cut, all axial planes are used.

Background noise subtraction:

.A) Methods 3, 4, 7 and 8:

Starting from the basic assumption that the background noise is constant along the z axis, before the AID is subjected to the fit function protocol the background intensity is cut by an automatic routine (for the fit it will be used equation 4.1 with the assumption $L = 0$). This routine automatically fit and substract the background noise assuming as initial value of the fit that the signal to noise ratio (SNR) is equal to SNR $= 80$ %; in other words it is assumed, as an initial condition, that the average noise intensity value is the 20 % of the maximum of the intensity.

.B) Methods 1, 2, 5and 6:

No background noise subtraction.

The distributions of the size measurements for 68 foci in one cell obtained using the 8 methods (see Table 6.1) described above were compared using the Kolmogorov-Smirnof statistical test (thanks to Sonya Martin). It was found, that there was no significant difference between the size measurements produced by the different methods (at the 5% significance level). Furthermore for each single foci (here called foci n. 0, foci n.1 etc. etc.) the mean value on this 8 different methods (meth.1, meth.2....meth.8) was considered as an estimate of the size and the standard deviation (SD) was used to estimate the accuracy and reproducibility of the SMI single size measurements. These foci were randomly selected from a specimen characterized by a good SNR then, in the 68% of the cases the values of SD are less than 10 % of the respective mean. This means that under reasonable good experimental conditions the results of the size measurements are reproducible with and indetermination around 10 %.

Table 6.1: Multiple SMI size evaluation of the same specimen. In the left side column are numbered the randomly selected foci used for this multiple evaluations; meth.1, meth.2$\cdots$ meth.8 are the 8 different evaluations methods to measure the foci axial size; under the column named mean the mean value of a single foci size is evaluated using the 8 different methods; under the column SD the values of the standard deviation evaluated using the 8 different methods are shown.

foci n.	meth.1	meth.2	meth.3	meth.4	meth.5	meth.6	meth.7	meth.8	mean	SD	x	y
0	68.7	75.7	68.3	69.2	67.7	70.7	67.9	67.7	69.5	2.7	111	72
1	68.4	75.4	67.0	81.6	69.5	71.3	69.6	69.5	71.5	4.8	129	96
2	65.1	78.1	75.0	71.0	72.0	68.9	77.1	72.0	72.4	4.3	112	108
3	62.8	73.9	59.7	73.0	69.5	71.3	69.6	69.5	68.7	4.9	126	97
4	83.1	72.3	62.3	67.1	63.0	64.1	60.9	63.0	67.0	7.4	89	95
5	67.6	77.4	65.7	89.9	74.5	68.8	74.6	74.5	74.1	7.6	91	99
6	67.2	66.6	64.1	65.4	53.8	66.7	58.8	53.8	62.0	5.7	88	115
7	62.0	58.0	65.1	72.0	61.9	53.9	70.0	61.9	63.1	5.9	65	120
8	73.8	81.6	71.1	70.4	62.4	71.3	59.4	62.4	69.0	7.3	68	129
9	66.7	71.2	67.7	72.6	77.6	75.7	66.0	77.6	71.9	4.8	56	125
10	67.0	65.9	67.9	54.9	51.0	54.7	50.9	51.0	57.9	7.6	64	139
11	86.4	83.4	59.8	57.2	58.4	66.0	58.8	58.4	66.1	11.9	62	131
12	65.9	66.6	61.8	65.6	58.4	66.0	58.8	58.4	62.7	3.7	65	133

13	74.6	68.4	81.1	69.8	93.4	73.5	60.6	93.4	76.9	11.7	78	139
14	65.7	51.0	59.2	52.4	79.8	72.1	63.2	79.8	65.4	11.2	76	149
15	62.9	74.4	60.9	61.6	62.8	64.7	61.6	62.8	64.0	4.4	80	152
16	74.2	74.1	78.0	77.4	75.5	68.4	74.9	75.5	74.8	2.9	76	161
17	86.7	66.5	57.2	69.5	57.7	61.2	59.2	57.7	64.5	10.0	71	177
18	86.1	96.8	87.3	90.3	85.8	83.5	85.2	85.8	87.6	4.2	65	185
19	73.7	66.9	63.8	66.3	62.9	69.0	62.8	62.9	66.0	3.8	44	170
20	81.7	73.5	71.7	73.8	79.3	76.5	81.9	79.3	77.2	3.9	32	159
21	78.0	65.1	58.8	59.7	60.8	60.4	55.5	60.8	62.4	6.8	77	196
22	76.8	67.1	56.6	56.8	61.5	66.0	61.9	61.5	63.5	6.5	91	193
23	59.7	58.0	68.5	59.4	77.4	60.9	98.4	77.4	70.0	13.9	92	200
24	79.7	75.9	55.8	86.5	66.4	75.9	67.9	66.4	71.8	9.6	109	184
25	75.0	66.6	61.5	61.9	67.3	66.3	67.0	67.3	66.6	4.1	115	180
26	55.3	64.3	63.4	65.2	66.6	68.5	67.3	66.6	64.6	4.1	103	171
27	63.2	61.5	70.7	69.1	61.3	65.7	47.6	61.3	62.5	7.0	114	157
28	57.1	55.1	49.6	44.8	53.5	58.0	69.4	53.5	55.1	7.2	125	159
29	75.5	44.6	54.3	53.2	57.8	66.1	58.4	57.8	58.5	9.2	131	157
30	76.4	65.4	82.6	70.8	76.0	59.9	57.1	76.0	70.5	8.9	127	169
31	76.6	72.8	68.5	76.8	58.4	68.5	58.4	58.4	67.3	7.9	142	144
32	90.0	87.2	87.4	87.6	105.	77.9	75.1	105.0	89.6	11.1	145	127
33	56.5	76.5	53.4	65.9	85.1	68.1	54.9	85.1	68.2	12.9	160	127
34	72.1	73.1	68.9	79.2	87.0	71.4	62.9	87.0	75.2	8.6	145	137
35	79.1	51.7	70.1	71.4	78.5	77.9	78.8	78.5	73.2	9.4	151	136
36	54.9	63.4	54.1	62.0	59.5	66.4	55.9	59.5	59.5	4.4	175	155
37	77.0	71.3	55.1	76.3	64.6	65.7	61.0	64.6	67.0	7.5	190	156
38	79.4	70.3	60.5	62.7	66.1	65.3	63.4	66.1	66.7	5.9	202	149
39	70.1	69.8	71.0	69.4	72.6	69.9	72.7	72.6	71.0	1.4	194	142
40	66.1	64.6	47.3	72.6	76.4	72.3	49.2	76.4	65.6	11.5	198	135
41	66.7	59.8	54.4	56.1	62.9	63.2	62.4	62.9	61.1	4.0	189	130
42	68.4	64.4	65.1	64.6	64.6	65.9	65.1	64.6	65.3	1.3	194	110
43	76.3	70.6	63.2	66.5	65.9	67.1	77.9	65.9	69.2	5.3	224	139
44	62.6	79.3	62.4	70.9	65.6	69.3	62.4	65.6	67.3	5.8	223	130
45	64.4	82.1	85.0	63.2	64.2	80.5	66.5	64.2	71.2	9.4	223	122
46	70.1	88.8	69.7	73.7	70.1	79.1	67.0	70.1	73.6	7.1	222	116
47	67.9	67.2	67.8	67.1	63.9	65.1	63.2	63.9	65.8	1.9	252	114
48	58.2	66.1	57.0	61.7	61.3	63.7	59.6	61.3	61.1	2.9	242	90
49	60.1	74.0	59.3	71.7	69.1	69.2	65.2	69.1	67.2	5.3	248	82
50	72.9	75.3	72.8	74.8	70.2	73.5	69.0	70.2	72.4	2.3	265	68
51	78.6	89.2	79.2	78.9	79.0	79.9	79.2	79.0	80.4	3.6	240	73
52	72.2	76.1	71.1	71.8	62.1	62.6	63.4	62.1	67.7	5.7	234	72
53	66.7	72.2	68.4	69.5	67.9	67.3	60.5	67.9	67.6	3.3	228	92
54	61.5	71.3	59.5	67.5	67.9	67.3	60.5	67.9	65.4	4.2	225	92
55	73.6	78.5	73.3	79.6	82.0	80.2	76.7	82.0	78.2	3.4	229	68
56	64.5	65.8	65.0	66.5	66.5	76.0	64.8	66.5	66.9	3.7	189	78
57	74.1	75.3	75.4	75.5	90.6	84.9	89.8	90.6	82.0	7.7	190	62
58	89.3	91.2	89.1	90.6	94.2	99.8	90.8	94.2	92.4	3.5	195	64
59	66.1	75.0	65.9	77.7	68.5	66.7	65.9	68.5	69.3	4.5	177	80
60	58.2	65.6	59.0	60.1	60.9	62.6	59.1	60.9	60.8	2.3	148	63
61	82.5	78.8	69.8	74.8	73.5	72.8	73.5	73.5	74.9	3.9	148	53
62	81.5	74.8	69.9	74.9	67.6	66.7	65.4	67.6	71.1	5.5	148	42
63	72.1	91.4	65.9	76.5	68.2	68.3	65.1	68.2	72.0	8.6	149	38
64	58.4	59.5	61.2	60.2	61.9	58.5	62.7	61.9	60.5	1.6	153	214
65	65.2	63.7	52.5	67.0	61.2	66.3	56.4	61.2	61.7	5.0	121	213
66	61.1	65.6	62.2	68.2	67.6	71.1	67.0	67.6	66.3	3.2	134	223
67	60.8	76.5	79.9	63.3	59.1	72.0	79.6	59.1	68.8	9.2	104	219
68	64.8	62.6	64.1	64.0	67.4	60.9	68.5	67.4	65.0	2.6	9	20

The optimal approach for size measurement was decided to be meth.3 in which the experimentally collected foci co-ordinates were used as the true centre of the foci, the AID was subjected to background subtraction but remained uncut. Methods 5-8 were rejected because by using the maximum intensity in a 5x5 mask as the true centre we were unable to discriminate between two foci very close together (i.e. less than 5 pixels apart). It was decided not to cut the AID as this method fails when intensity peaks occurring at the edges of the AID are higher than the true AID intensity maximum (this often occurs with smaller foci). It was decided to use the background subtraction method as it removes one parameter thus making the AID easier to handle. It is apparent that all of the 8 methods can fail depending on the starting parameter inserted or on the users ability to adjust the parameters in an order of magnitude of 5%.

The mean value ($\mathcal{S}_m$) computed on all the evaluations shown in Table 6.1 performed using meth.3 is $\mathcal{S}_m = 66.1$ nm with a SD equal to 9.1 nm.

In Figure 6.1 the histogram of the size evaluation performed using meth.3 and relative to the data shown in Table 6.1 is shown. Nine more random selection were done using nine different cell acquisitions. Merging all the results (451 independent foci were evaluated) of these evaluations and the results shown in Table 6.1 the mean estimate value of the size of the foci ($\pm SD$) was found to be:

$$\mathcal{S}_m = (75 \pm 19) nm.$$

To explain a so big difference between the two mean size estimates, it must be considered that not all the cell used in this experiment give AID with a good SNR. In Figure 6.2 a comparasion of the two size measurements distribution is made; the reader may note that the first histogram was made using part of the measurements used even in the second histogram. Then the difference between the mean value of the first distribution (data shown in Table 6.1) and the mean values of all the data except the data of relative of Table 6.1 should be bigger than 9 nm. In Figure 6.3 is shown the difference between an AID with a good SNR (this is an AID relative to a foci shown in Table 6.1) an an AID with a low SNR. One experimental evidence that can be proved only with the visualization of massive quantities of data (not possible here) is that the size evaluation performed on AID with low SNR give rise almost always to bigger sizes values. A low SNR means often that the bleaching effect is predominant and then one of the most important assumption of the size evaluation VIM algorithm is not complitely true: the objects to be measured should be homogeneously covered by fluorochrome.

In Figure 6.4 a diffraction bidimensional image of the cell with the higher SNR is shown; even more is described how a random selection of foci in the cell was made.

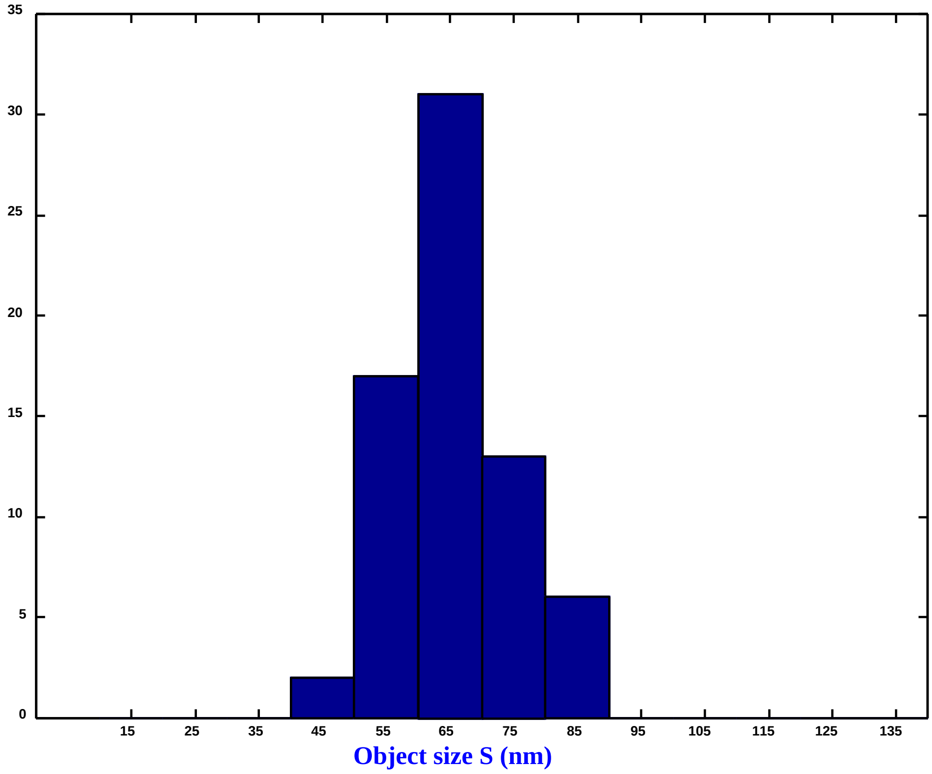

Figure 6.1: Size measurements distributions of 68 foci randomly selected from one Cryosections.

For quantified how big is the drift to higher size estimate due to low SNR another random foci choice was made considering the 5 cells with the best SNR; the estimation of the size (148 foci) was:

$$\mathcal{S}_m = (69 \pm 19)nm$$

. If only the two best SNR cells are used the following estimate of transcription factories size (relative to 50 foci) was found:

$$\mathcal{S}_m = (60 \pm 13)nm$$

. In Figure 6.5 the distribution of the size evaluation relative to all the 148 foci selected is shown. That foci are order in such a way that the first 50 (numbered: 1-50) are the foci relative the

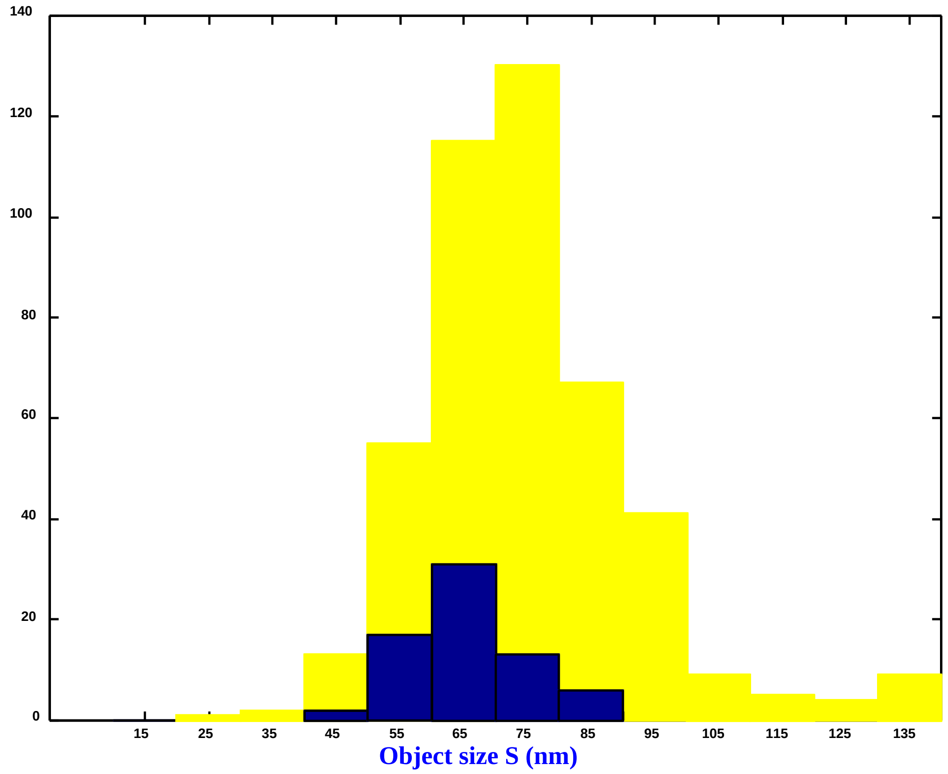

Figure 6.2: Comparasion between the size distribution obtained using all the foci randomly selected (451 foci) and the distribution (in blue)relative to 68 foci selected only in one Cryosections.

best 2 SNR cells; it is clearly possible to see a drift to bigger size values of the measurements for the restant 98 foci (51-148). In my opinion the results shown in Table 6.1 (meth.3) should be considered as the size estimation of the transcription factories. This an intuitive opinion based on objective facts (size versus SNR). Then such estimate can not substitute the one relative of all first foci selection or the one relative to the second foci selection because is not supported by enough scientific data. So the estimate of the first complete selection or the second complete foci selection should be used as the actual estimate of the transcription factories size with the high suspicion that such results are overestimation due to multiple efficiency defect of the system.

As in the previous Chapters a really critical discussion of the Heidelberg SMI system is the best way to consider positively the results of this experiments. If these measurements were performed under optimal conditions the conclusion should be that an SMI microscope can be used only for preliminary size evaluation but can not give rise to high level biological investigation. The high pioneer way in which a scientist is forced to work hoping to perform decent acquisition (for this experiment were selected only 10 and only 2 were (for my opinion)

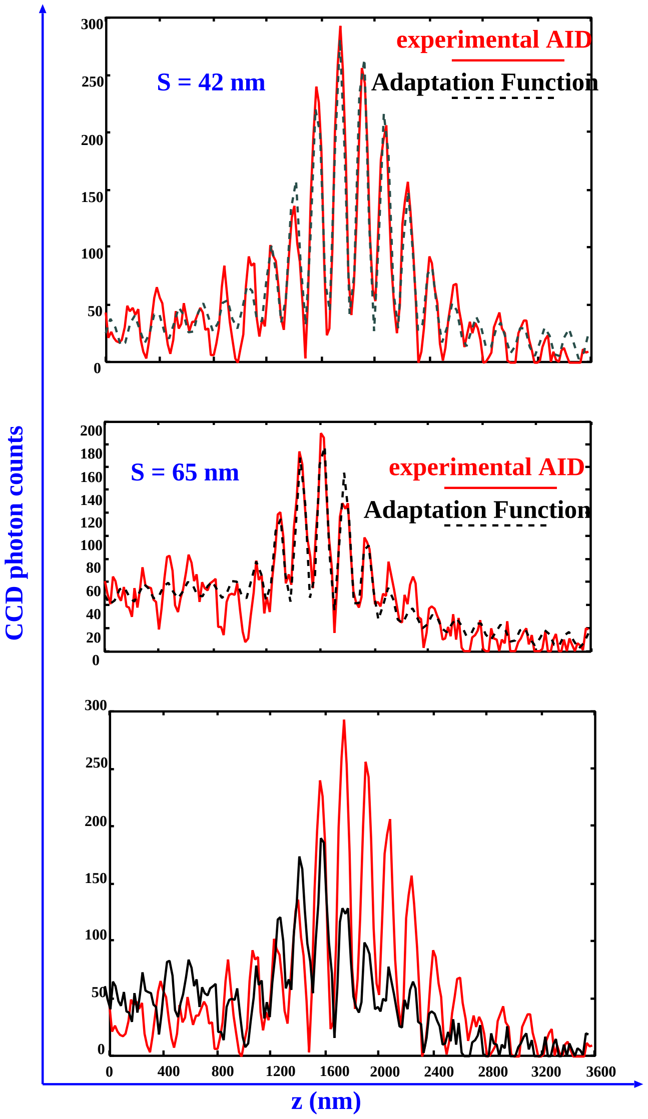

Figure 6.3: Example of dependence between size evaluation and SNR (or bleaching). In the top is shown an AID with good SNR relative the Cryosections which data is exposed in Table 6.1. Middle: The AID of one foci selected randomly by a Cryosections in which the SNR was not so good. Bottom: The superposition of the two previous AID are shown in scale.

really useful respect of more than one week of hard experimental work indicates that with simple structural improvement this instrument can be really used in advanced research.

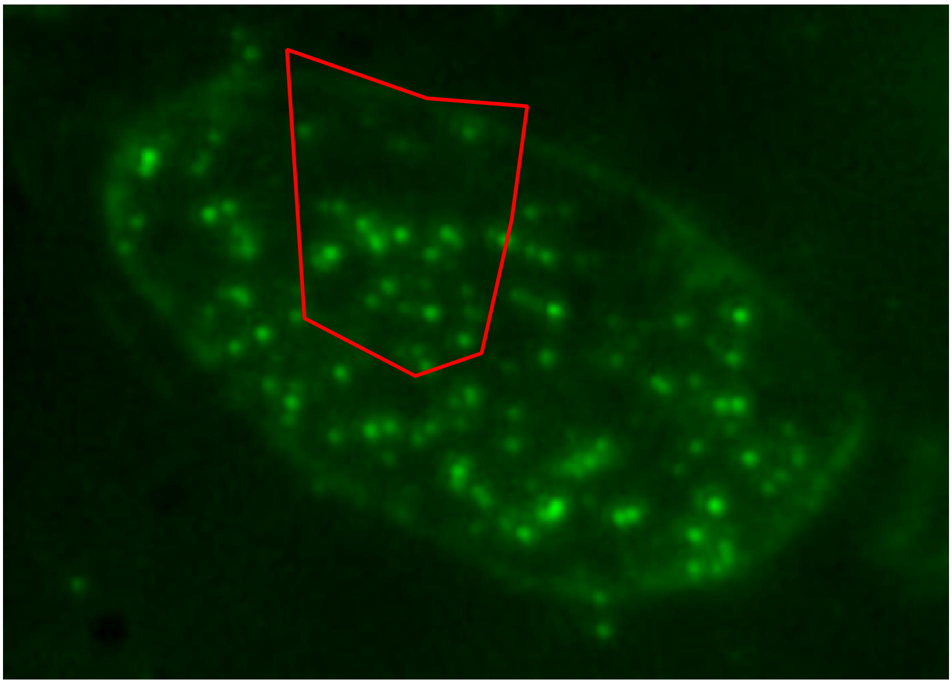

Figure 6.4: A diffraction image of a Cryosections is shown: This Figure should not be used in a biological presentation because the shape of the cell is not circular. This image is used only to show how a random selection is made. An area statistically representative (from the border to the center) is selected (red line). All the foci inside this area will be used for size evaluations.

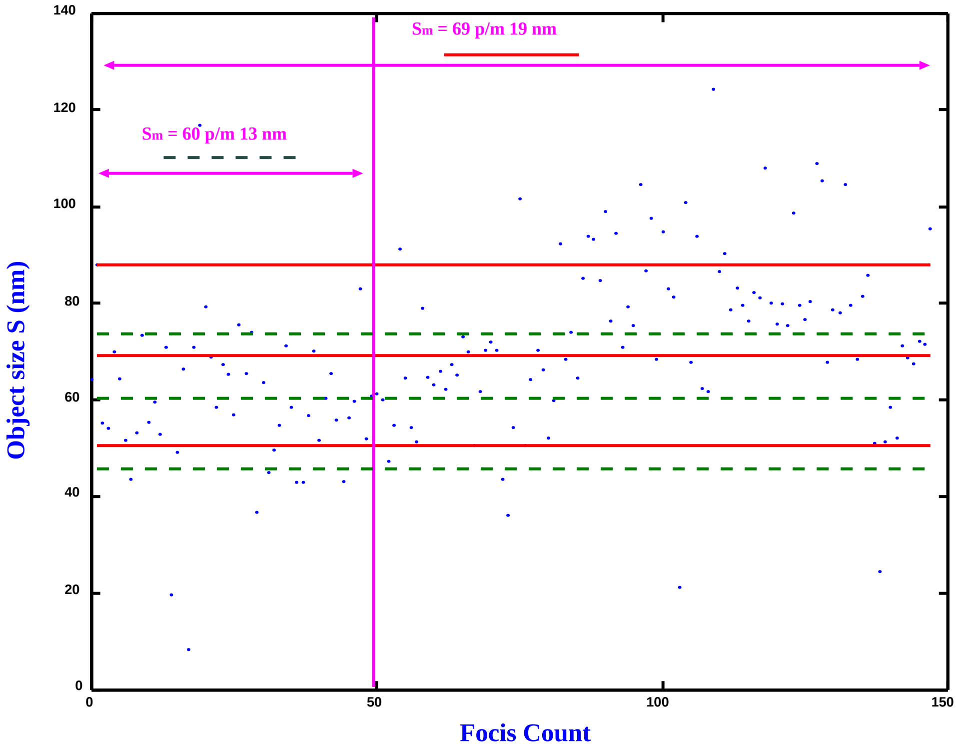

Figure 6.5: Distribution of size measurements: All the selected foci are numbered; the first 50 foci are relative to the two Cryosections with the best SNR. There is a relevant difference between the mean value of the size $\mathcal{S}_m$ relative to the first 50 foci and the mean value of the size $\mathcal{S}_m$ relative to all the distribution.

Chapter 7

Conclusion and Prospectives

7.1 Conclusions

The initial conditions of this dissertation were that it was a common need to understand what can of potential has SMI microscopy. Not so much before was made in order to show the theoretical limits of the instruments regarding topology measurements. In other words this dissertation starts with the introduction of SMI-VIM in order to discover the potentiality of the instruments in topology evaluations. The results shown Chapter 1 indicates that SMI microscopy allows really high resolution topological measurements far down the optical resolutions limits (e.g. 800 nm). The SMI VIM experiments discover that it is possible to resolve distances between objects with an accuracy far down the one nanometer range even in photon count conditions due to biological samples. Furthermore SMI VIM first discover a new application (see Chapter 2): The algorithms to measure subwavelengths sized object with SMI microscopy were introduced: In a second time (see Chapter 3) the limits of size determination in SMI microscopy was the main subject to be discussed. For example was pointed out that it is possible presently to measure sizes down to 30 nm using $\lambda_{ex} = 488$ nm and using $\lambda_{ex} = 360$ nm this limits can be push down to 10 nm.

The second part of the dissertation (see Chapter 4, Chapter 5 and Chapter 6) was dedicated to real experimental measurements.

In Chapter 4 several size measurements using different sized fluorescent beads were performed. Size measurements indicates that it is possible to determine objects sizes down to 40 nm using $\lambda_{ex} = 647$ nm and down to 30 nm using $\lambda_{ex} = 488$ nm. With both the previous mentioned excitation wavelength size measurements in the 50-100 nm range are feasible with high accuracy. Up to now the author is trying to discover what other light microscopy set up allows these kind of measurements.

In Chapter 5 topology measurements were shown that confirms the theoretical previsions of Chapter 1.

Finally Chapter 6 presents as a biological application the experiments performed in order to estimate the size of transcription factories. It was possible to make an estimation of the size of the transcription factories in a range exclusive to SMI microscopy (around 70 nm). The scientific importance in biology of this experiments can not be indicated by the author of the present dissertation.

Did SMI microscopy show all its potential during this dissertation? If the answer is yes I can say that anyway this potential is big and allows a long series of practical application for the microscope, and it is even realistic to imagine that a commercial prototype of the microscope can be built. Honestly I think that this work can be considered as the starting point of a new series of theoretical studies and experimental measurements and in this dissertation it was not possible to point out a reach number of phenomena that can be originally studied with the microscope.

A little gallery of Figures in the following will indicate new ideas (not only simple ideas) for develop research in SMI microscopy. Each of the following Figures can be considered as the programmatic starting point of new work.

7.2 Prospectives

7.2.1 SMI ”Linear” tomography or ”dynamic resolution”

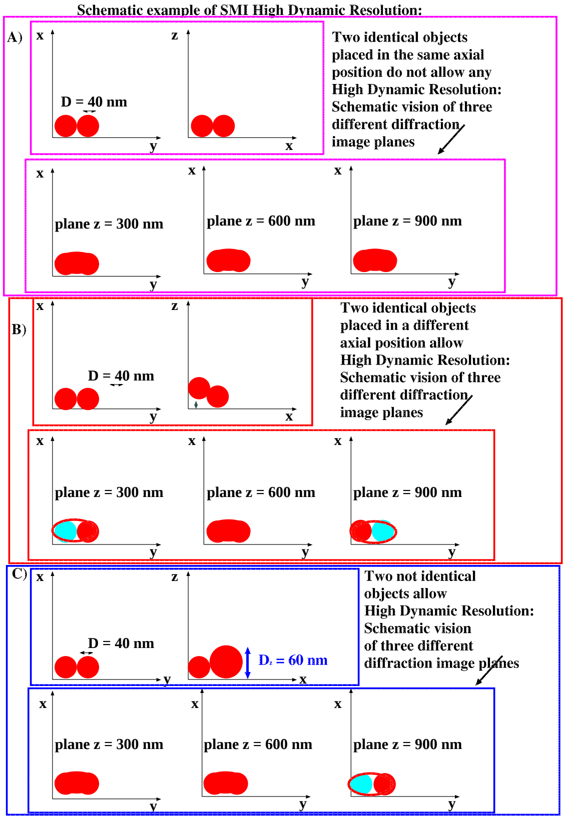

Figure 7.1: Sometime a two dimensional SMI image can be worser than the one it is possible to acquire with the confocal. In the future this problem can be technically resolved and hopefully the SMI will present bidimensional images as in the modern confocal system. If other aspects are considered this improvements will not make the SMI system so special. Forgetting all the huge amount of precious information offered by SMI Microscopy (size evaluation, high resolution topology) it is possible to use his image detection procedure for discrimate objects really close in the limit of one voxel. Imagine to have two identical fluorescent balls one closer to the other (they can touch one each other) and this balls have a diameter of 50 nm; the projection of these balls on the axial direction is the same; in every bidimensional image plane that will be analyzed only one big spot will be shown and it is not possible to reach any conclusion: if this spot is made by one two three 100 elements. Imagine now that the same balls are placed in such a way that the projection in axial direction is almost the same but not the same; what will shown playing the movie of the all the bidimensional acquisition is that in same planes, as before, a huge big spots homogeneously illuminated will be shown, but in few other planes at the beginning and in the end of the movie it will be possible to note that the big spots is more illuminated on the left in some frames and in some other is more illuminated on the right. Increasing the difference between the projection of the fluorescent two balls on the axial direction these effect will be enhanced. The same effect can be noted if the two ”balls” have a different diameter. Even in the first case mentioned would be possible to resolve the two balls by contolling the direction of the wavefront i.e. when the wavefront is not perpendicular to optical axis. This effect can be called SMI High Dynamic Resolution (SMI-HDR) or SMI-Linear Tomography (SMI-LT). The SMI microscopy can be considered as a dynamic microscopy.

7.2.2 New SMI-VIM calibration processes

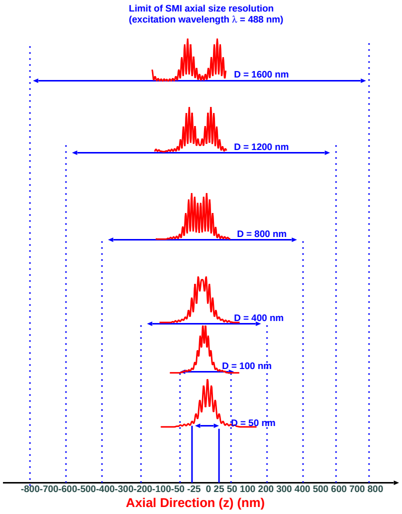

Figure 7.2: In this Figure are represented the AIDs of two extended objects (with a diameter $\mathcal{S}$ = 50 nm). The excitation wavelength was fixed to be λ_{ex} = 488 nm. The computations were performed in ideal noiseless conditions using ensembles of point like objects. The Figure shows that, using SMI-VIM, it is possible to realize calibrations functions in order to determine the relative distance of the two points using a minimum of one spectral signature. The intensity profiles are changing with the distance between the two ”point-like” objects.

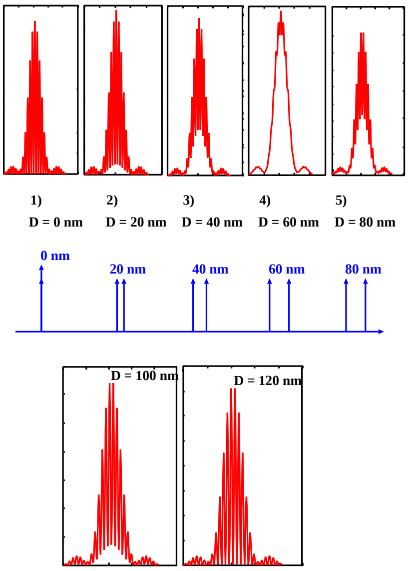

Figure 7.3: In this Figure are represented the AIDs of two point like objects (with a diameter $\mathcal{S}$ = 10 nm). The excitation wavelength was fixed to be λ_{ex} = 488 nm. The computations were performed in ideal noiseless conditions using ensembles of point like objects. The Figure shows that, using SMI-VIM, it is possible to realize calibrations functions in order to determine the relative distance of the two points using a minimum of one spectral signature. The intensity profiles are changing with the distance between the two ”point-like” objects.

7.2.3 Advanced SMI-VIM topology

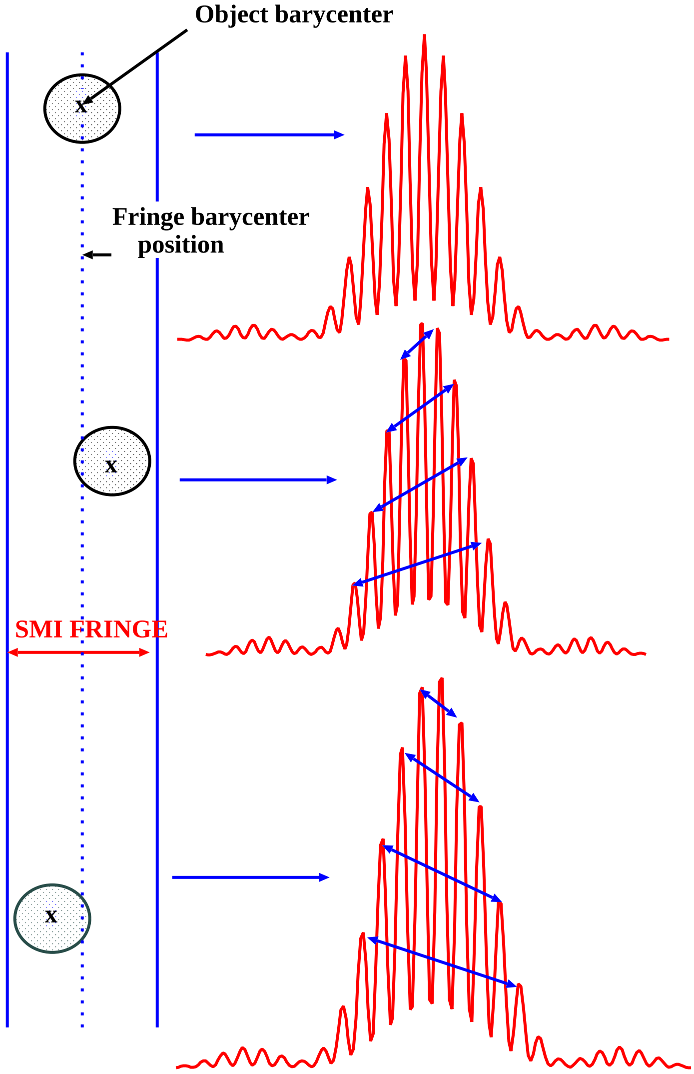

Figure 7.4: VIM evaluation of the object barycentre position respect to the fringes barycentre.
Case: $\lambda_{ex} = 488$ nm.
All the AIDs are produced by VIM in ideal noiseless conditions using an ensembles of 5 point like objects ($\mathcal{S} = 50$ nm).

7.2.4 Determination of size and topology of a Macro Molecular Complexes MMC.

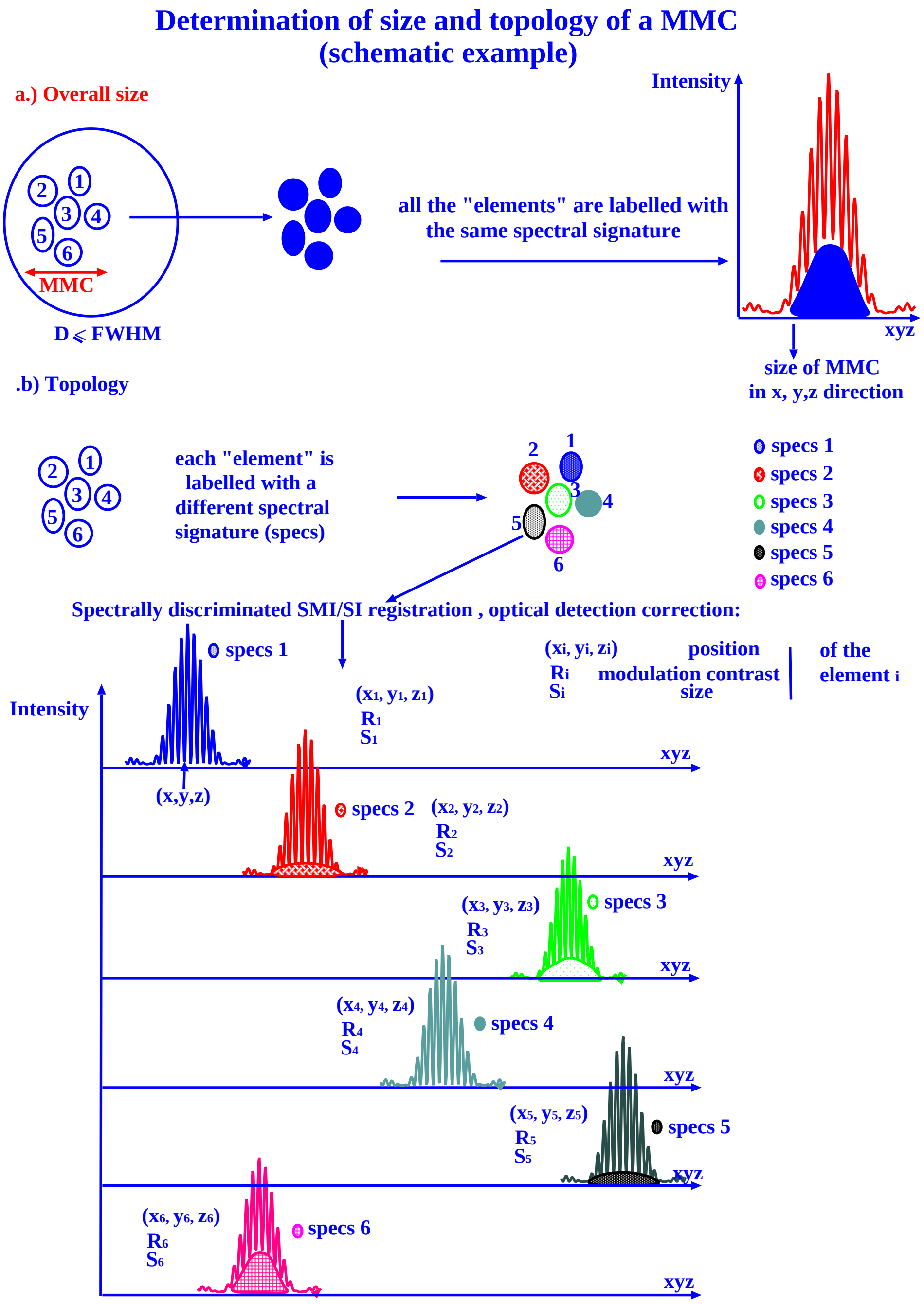

Figure 7.5: Determination of size and topology of a MMC.Original idea of Prof. Dr. Dr. C. Cremer.

7.2.5 Gene expression in SMI microscopy

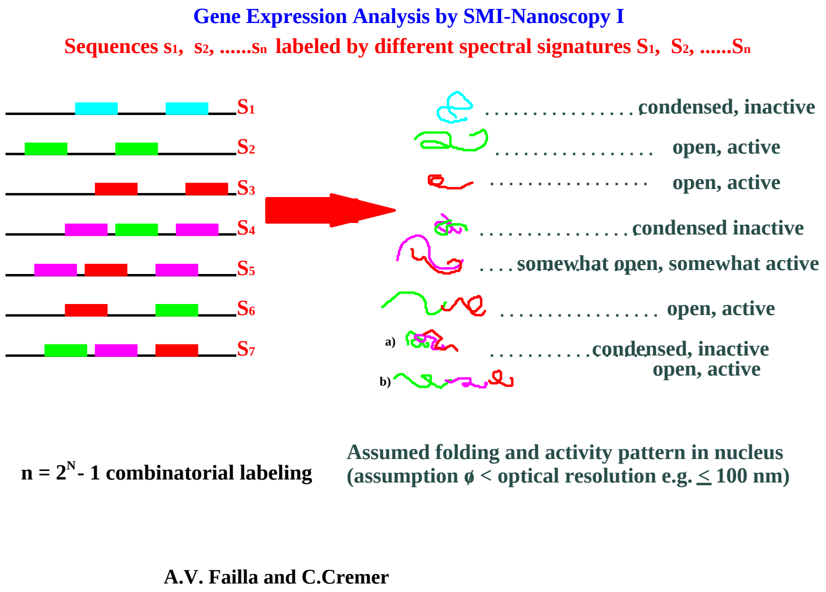

Figure 7.6: Gene expression in SMI microscopy schematic example 1. Original idea of Prof. Dr. Dr. C. Cremer.

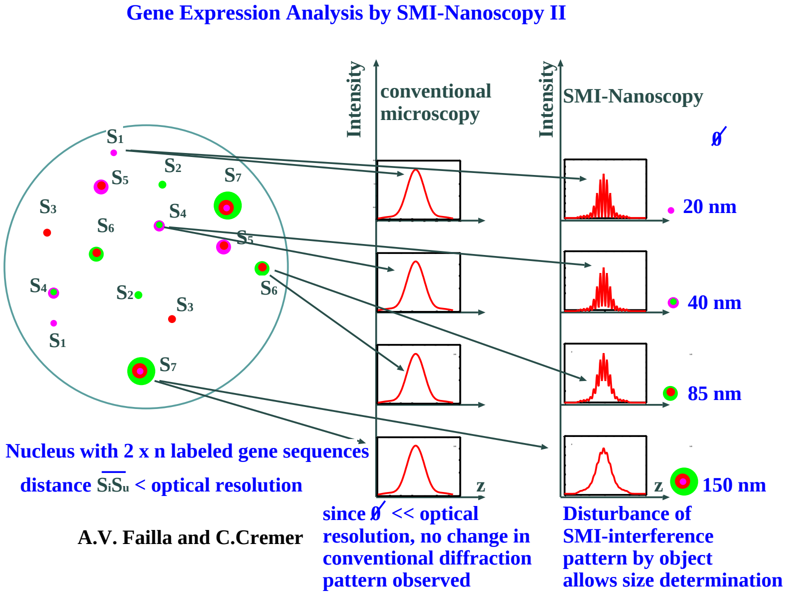

Figure 7.7: Gene expression in SMI microscopy schematic example 2. Original idea of Prof. Dr. Dr. C. Cremer.

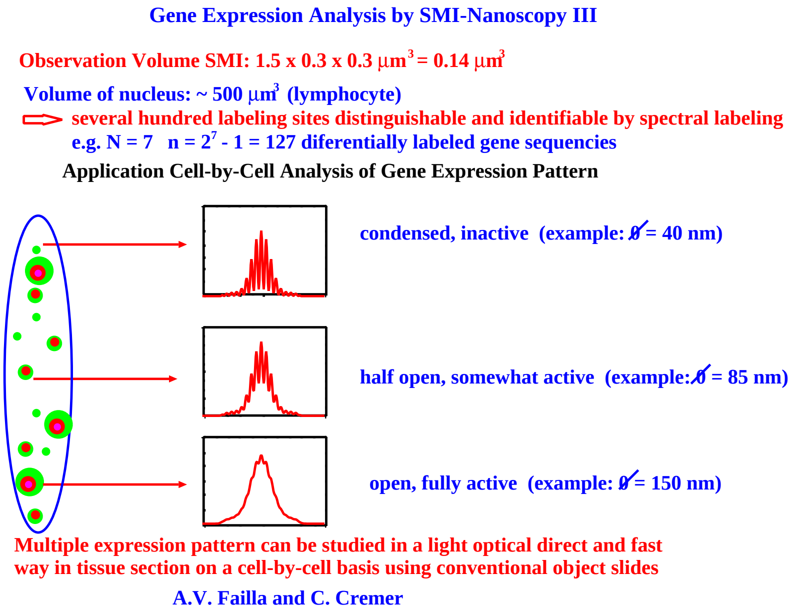

Gene Expression Analysis by SMI-Nanoscopy III

Observation Volume SMI: 1.5 x 0.3 x 0.3 μm^3 = 0.14 μm^3

Volume of nucleus: ~ 500 μm^3 (lymphocyte)

⇨ several hundred labeling sites distinguishable and identifiable by spectral labeling
e.g. N = 7 n = 2^7 - 1 = 127 diferentially labeled gene sequencies

Application Cell-by-Cell Analysis of Gene Expression Pattern

condensed, inactive (example: Ø = 40 nm)

half open, somewhat active (example: Ø = 85 nm)

open, fully active (example: Ø = 150 nm)

Multiple expression pattern can be studied in a light optical direct and fast way in tissue section on a cell-by-cell basis using conventional object slides

A.V. Failla and C. Cremer

Figure 7.8: Gene expression in SMI microscopy schematic example 3.
Original idea of Prof. Dr. Dr. C. Cremer.

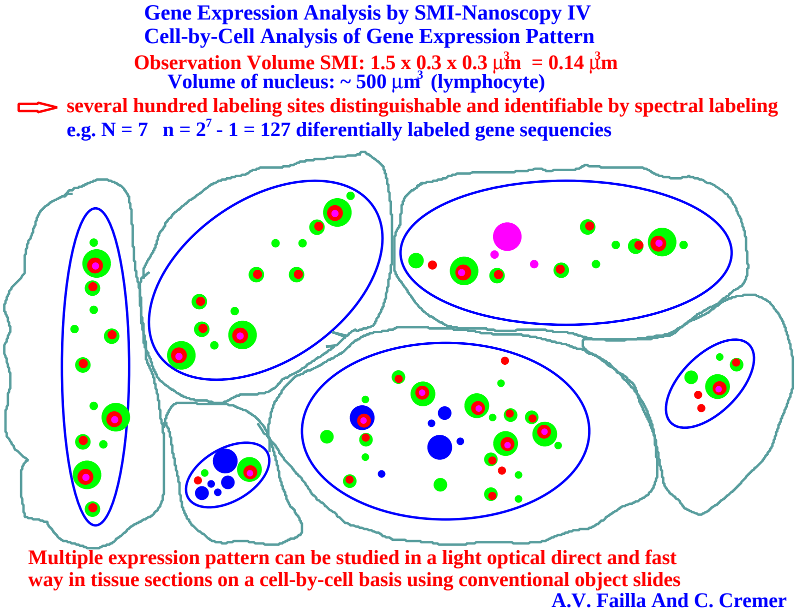

Gene Expression Analysis by SMI-Nanoscopy IV
Cell-by-Cell Analysis of Gene Expression Pattern

Observation Volume SMI: 1.5 x 0.3 x 0.3 μm^3 = 0.14 μm^3
Volume of nucleus: ~ 500 μm^3 (lymphocyte)

⇨ several hundred labeling sites distinguishable and identifiable by spectral labeling
e.g. N = 7 n = 2^7 - 1 = 127 diferentially labeled gene sequencies

Multiple expression pattern can be studied in a light optical direct and fast way in tissue sections on a cell-by-cell basis using conventional object slides

A.V. Failla And C. Cremer

Figure 7.9: Gene expression in SMI microscopy schematic example 4.
Original idea of Prof. Dr. Dr. C. Cremer.

List of Figures

List of Tables

Bibliography

[1] A. V. Failla and C. Cremer. Virtual spatially modulated illumination microscopy predicts nanometer precision of axial distance measurements. *Proc. SPIE in press*, 2001.

[2] A. V. Failla, B. Albrecht, A. Schweitzer, and C. Cremer. Spatially modulated illumination microscopy a new approach to biological nanostructure analysis. *G.I.T.*, (2):40–42, 2001.

[3] A. V. Failla, P.Edelmann, A. Schweitzer, and C. Cremer. Nanotopology analysis in three-dimensional light microscopy. *to be submitted Optics*, 2002.

[4] A. V. Failla, P.Edelmann, and C. Cremer. Virtual spectral precision distance microscopy indicate nanometer distance resolution in biological specimen. In *QMC II*, pages 199–202, 2001.

[5] A. V. Failla, B. Albrecht, R. Heintzmann, and C. Cremer. Spatially modulated illumination microscopy: online visualization of intensity distribution and prediction of nanometer precision of axial distance measurements by computer simulations. *Journal of Biomedical Optics*, (6(3)):292–299, 2001.

[6] A. V. Failla, A. Cavallo, and C.Cremer. Subwavelength size determination using smi virtual microscopy. *Appl. Opt. submitted*, 2002.

[7] B. Albrecht, A. V. Failla, A. Schweitzer, and C. Cremer. Spatially modulated illumination microscopy allows axial distance resolution near one nanometer. *Appl. Opt.*, 1(41):80–87, 2002.

[8] A. V. Failla, B. Albrecht, U. Spoeri, A. Kroll, and C.Cremer. Nanosizing of fluorescent objects by spatially modulated illumination microscopy. *Appl. Opt. submitted*, 2002.

[9] B. Albrecht, B.Schneider, A. Schweitzer, A. V. Failla, T. Jaeger, A. Kroll, G. Hildenbrend, A. Weisel, M. Hausmann, P. Edelmann, and C.Cremer. Distance measurements with axial precision in the nanometer range using spatially modulated illumination microscopy. In *QMC II*, 2002.

[10] B.Schneider, J. Bradl, I. Kirsten, M. Hausmann, and C. Cremer. High precision localization of fluorescent targets in the nanometer range by spatially modulated excitation fluorescence microscopy. *In: Fluorescence microscopy & fluorescence probes*, (2):63–68, 1998.

[11] B.Schneider, I. Upmann, I. Kirsten, J. Bradl, M. hausmann, and C. Cremer. A dual-laser, spatially modulated illumination fluorescence microscope. *Microscopy and Analysis*, (1):5–7, 1999.

[12] B.Schneider, B. Albrecht, P. Jaeckle, D. Neofotistos, S. Soeding, T. Jaeger, and C. Cremer. Nanolocalization measurements in spatially modulated illumination microscopy using two coherent illumination beams. *Optical Diagnostics of Living Cells III SPIE*, (3921):321–330, 2000.

[13] T. Cremer, G. Kreth, H. Koester, R.H.A. Fink, R. Heintzman, I. Solovei, D. Zink, and C. Cremer. Chromosome territories, interchromatin domain compartment and nuclear matrix: an integrated view of the nuclear architecture. *Critical Reviews in Eukaryotic Gene Expression*, (12):179–212, 2000.

[14] T. Cremer, A. Kurz, R. Zirbel, S. Dietzel, B. Rinke, E. Schröck, M. R. Speicher, U. Mathieu, A. Jauch, P. Emmerich, H. Scherthan, T. Ried, C. Cremer, and P. Lichter. Role of chromosome territories in the functional compartmentalization of the cell nucleus. *Cold Spring Harb.Symp.Quant.Biol.*, (58):777–792, 1993.

[15] C. Cremer, C. Münkel, M. Granzow, A. Jauch, S. Dietzel, R. Eils, X. Y. Guan, P. S. Meltzer, J. M. Trent, J. Langowski, and T. Cremer. Nuclear architecture and the induction of chromosomal aberration. *Mut. Res.*, (19):139–146, 1996.

[16] T.Cremer and C. Cremer. Nuclear architecture and gene regulation in mammalian cells. *Nature Reviews Genetics*, 4(2):292–301, 2001.

[17] P. Edelmann and C. Cremer. Improvement of confocal spectral precision distance microscopy (spdm). *SPIE Vol.*, (3921):313–320, 2000.

[18] S. W. Hell, E. H. K. Stelzer, S. Lindek, and C. Cremer. Confocal microscopy with an increased detection aperture: type-b 4pi confocal microscopy. *Optics Lett.*, (19):222–224, 1994.

[19] S .W. Hell, S. Lindek, C. Cremer, and E. H. K. Stelzer. Measurement of the 4pi-confocal point spread function proves 75 nm axial resolution. *Appl. Phys. Lett.*, (64):1335–1337, 1994.

[20] S. Lindek, E. H. K. Stelzer, and C. Cremer. Confocal theta fluorescence microscopy with anular aperture. *Appl. Optics*, (35):126–130, 1996.

[21] Bailey, D .L. Farkas, D. L. Taylor, and F. Lanni. Enhancement of axial resolution in fluorescence microscopy by standing wave excitation. *Nature*, (366):44–48, 1993.

[22] M. G. Gustafsson, D. A. Agard, and J. W. Sedat. Sevenfold improvement of axial resolution in 3d wide field microscopy using two objective lenses. *Proc. SPIE*, (2412):147–156, 1995.

[23] A. Esa, P. Edelmann, L. Trakthenbrot, N. Amariglio, G. Rechavi, M. Hausmann, and C. Cremer. 3d-spectral precision distance microscopy (spdm) of chromatin nano structures after triple-color labeling: a study of the bcr region on chromosome 22 and the philadelphia chromosome. *J. Microscopy*, (189):118–136, 2000.

[24] T. D. Lacoste, X. Michalet, F. Pinaud, D. S. Chemia, A. P. Alivistatos, and S. Weiss. Ultrahigh-resolution multicolor colocalization of single fluorescent probes. *Proc. Natl. Acad. Sci. USA*, (97):9461–9466, 2000.

[25] H. Bornfleth, K. Sätzler, R. Eils, and C. Cremer. High precision distance measurements and volume-conserving segmentation of objects near and below the resolution in three-dimensional confocal fluorescence microscopy. *J. Microscopy*, (189):118–136, 1998.

[26] A. M. van Oijen, J. Köhler, J. Schmidt, M. Müller, and G. J. Brakenhoff. 3-dimensional super-resolution by spectrally selective imaging. *Chemical Physics Letters*, (292):183–187, 1998.

[27] M. Schmidt, M. Nagorny, and S.W. Hell. Subresolution axial measurements in far-field fluorescence microscopy with precision of 1 nanometer. *Rev. Sci. Instrum.*, (71):2742–2745, 2000.

[28] G. Mariott, R.M. Clegg, D.J. Arndt-Jovin, and T.M. Jovin. Time-resolved imaging microscopy phosphorescence and delayed fluorescence imaging. *Biophys. J.*, (60):1374–1387, 1991.

[29] J.R. Lakowicz, H. Szmaczinnski, , and K. Nowaczyk. Fluorescence lifetime imaging. *Proc. Natl. Acad. Sci. Usa*, (89):1271–1275, 1992.

[30] A. Schoenle, M. Glatz, and S.W. Hell. Four-dimensional multiphoton microscopy with time correlated single-photon counting. *Appl. Opt.*, (39):6306–6311, 2000.

[31] E. Betzig and J:K: Trautmann. Near-field optics: Microscopy, spectroscopy and surface modification beyond the diffraction limit. *Science*, (257):189–195, 1992.

[32] M. Born and E.wolf. *Principle of Optics*. Pergamon press, 1980.

[33] H. Bornfleth, K. Sätzler, , D. Zink, R. Eils, and C. Cremer. Model based segmentation of of biological structures in three-dimensional confocal microscopic images using a four-dimensional approach. *Cell Vision*, (4):203–204, 1997.

[34] H. bornfleth. *Precision distance microscopy and model based segmentation for the analysis of the functional topology of the cell nucleus.* PhD thesis, Ruperto Carola University of Heidelberg, 1998.

[35] J. Bradl, M. Hausmann, V. Ehemann, D. Komitowski, and C. Cremer. A tilting device for 3d microscopy: application to in situ imaging of interphase cell nuclei. *J.Microscopy*, 1(168):47–57, 1992.

[36] J. Bradl, B. Rinke, A. Esa, P. Edelmann, H. Krieger, B. Schneider, M.Hausmann, and C. Cremer. Comparative study of three-dimensional localization accuracy in conventional confocal laser scanning and axial tomographic fluorescence light microscopy. *Proc. SPIE*, (2926):201–206, 1996.

[37] J. Bradl, M. Hausmann, B. Schneider, B. Rinke, and C. Cremer. A versatile 2π tilting device for fluorescence microscope. *J. Microscopy*, 3(176):211–221, 1994.

[38] Jr. M. Bruchez, M. Moronne, P. Gin, S. Weiss, and A:P: Alivisatos. Semiconductor nanocrystals as fluorescent biological labels. *Science*, 5385(281):2013–2016, 1998.

[39] K. Carllson and N.Aslund. Confocal imaging for 3-d digital microscopy. *Applied Optics*, (26):3232–3238, 1987.

[40] R.Chmelik and H. Zdenek. Parralel-mode confocal microscopy. *Proc. SPIE*, (3568):101–109, 1999.

[41] C. Cremer and T. Cremer. Consideration on a laser scanning microscope with high resolution and depth of field. *Microscop. Acta*, (81):31–44, 1978.

[42] P. Edelmann, A. Esa, H. Bornfleth, R. Heintzmann, and C. Cremer. Correlation of chromatic shifts and focal depth in spectral precision distance microscopy measured by micro axial tomography. *Proc. SPIE*, (3568):89–95, 1999.

[43] G. Ende, H. Treuer, and R. Boesecke. Improvement in axial resolution by interference confocal microscopy. *Phys Med Biol*, 1(37):261–271, 1992.

[44] M. G. Gustafsson, D. A. Agard, and J. W. Sedat. 3d widefield microscopy with two objective lenses: Experimental verification of improved axial resolution. *Proc SPIE*, (2655):62–66, 1996.

[45] R. Heintzmann, H. Meunch, and C.Cremer. High-precision distance measurements in epifluorescent microscopy simulation and experiment. *Cell Vision*, 2(4):252–253, 1997.

[46] R. Heintzmann and C.Cremer. Reconstruction of axial tomographic high resolution data from confocal fluorescence microscopy: A method for improving 3d fish images. *Analytical Cellular Pathology accepted*, 1999.

[47] G.M.P. van Kempen, L.J. van Vliet, and P.J. Verveer. A quantitative comparasion of image restoration methods for confocal microscopy. *Journal of Microscopy*, 3(185):354–365, 1997.

[48] E.M.M. Manders, F.J. Verbeek, and J.A. Aten. Measurement of co-localization of objects in dual-colour confocal images. *Journal of Microscopy*, 3(169):375–382, 1993.

[49] E.M.M. Manders, R. Hoebe, J. Strackee, A.M. Vossepoel, and J.A. Aten. Larger contour segmentation: A tool for the localization of the spots in confocal images. *Cytometry*, (23):15–21, 1996.

[50] A. Patwardhan. Subpixel position measurements using 1d, 2d and 3d centroid algorithm with emphasis on application in confocal microscopy. *Journal of Microscopy*, 3(186):246–257, 1997.

[51] E.H.K. Stelzer. Contrast, resolution, pixelation, dynamic range and signal-to-noise ratio: fundamental limit to resolution in fluorescence microscopy. *Journal of Microscopy*, (189):15–24, 1998.

[52] T. Wilson, R. Juskaitis, and M.A.A. Neil. A new approach to three dimensional imaging in microscopy. *Cell Vision*, 2(4):231, 1997.

[53] T. Wilson, R. Juskaitis, M.A.A. Neil, and M. Kozubeck. An aperture correlation approach to confocal microscopy. *proc. SPIE*, (2981):21–23, 1997.

[54] D. Chapman. *Teach yourself Visual C++ in 21 days.* SMAS publishing, 1998.

[55] D. Kruglinski, S.Wingo, and G.Shepherd. *Inside Visual C++ 6.0.* Microsoft Press Redmond, 1998.

[56] D. Pallmann. *Programming Bots, Spiders and Intelligent Agents in Microsoft Visual C++.* Microsoft Press Redmond, 1999.

[57] R. Heintzmann. *Resolution Enhancement of Biological Light Microscopic Data.* PhD thesis, Ruperto Carola University of Heidelberg, 1999.

[58] D.A. Jackson, F.J. Iborra, E.M.M. Manders, and P.R. Cook. Numbers and organization of rna polymerases, nascent transcripts and transcription units in hela nuclei. *Mol Biol Cell*, (9):1523–1536, 1998.

[59] F.J. Iborra, A. Pombo, D.A. Jackson, and P.R. Cook. Active rna polymerases are localized within discrete transcription factories in human nuclei. *J. Cell Sci*, (109):1427–1436, 1996.

[60] P.R. Cook. The organization of replication and transcription. *Science*, (284):1790–1795, 1999.

[61] A. Pombo, D.A. Jackson, F.J. Iborra, M. Hollinshead, H. Kimura, K. Sugaya, and P. R. Cook. Transcription factories. In *Eurem 12 Brno*, volume B, pages 461–464, 2000.

[62] A. Pombo, P. Cuello, W. Schul, Jong-Bok Yoon, R.G. Roeder, P.R. Cook, and S. Murphy. Regional and temporal specialization in the nucleus: a transcriptionally-active nuclear domain rich in ptf, oct1 and pika antigens associates with specific chromosomes early in the cell cycle. *The EMBO Journal*, (17):1768–1778, 1998.

[63] A. Pombo, M. Hollinshead, and P.R. Cook. Bridging the resolution gap: Imaging the same transcription factories in cryosections by light and electron microscopy. *.Histochem. Cytochem.*, 4(47):471–480, 1999.

[64] G. Blobel. Gene gating: a hypothesis. *Proc. Natl. Acad. Sci. Usa.*, (82):8527–8530, 1985.

[65] J.T. Frohn, H.F. Knapp, and A. Stemmer. True optical resolution beyond the rayleight limit achieved by standing wave illumination. *Proc. Natl. Acad. Sci. USA.*, (97):7232–7236, 2000.

[66] J.T. Frohn, H.F. Knapp, and A. Stemmer. Three-dimensional resolution enhancement in fluorescence microscopy by harmonic excitation. *Opt. Lett.*, (26):828–830, 2001.

[67] T. A. Klar, S. Jacobs, M. Dyba, A. Egner, and S. W. Hell. Fluorescence microscopy with diffraction resolution barrier broken by stimulated emission. *Proc. Natl. Acad. Sci. USA*, (87):8206–8210, 2000.

[68] S. W. Hell, S. Lindek, and E. H. K. Stelzer. Enhancing the axial resolution in far-field light microscopy: two photon 4pi confocal fluorescence microscopy. *Journal of Modern Optics*, (41):675–681, 1994.

Contents